EXTINCTION DROPLET SIZING MEASUREMENTS IN DIESEL RELEVANT SPRAYS

A Thesis Presented to
The Academic Faculty

By

Gabrielle Louise Martinez

In Partial Fulfillment
Of the Requirements for the Degree
Master of Science in the
School of George W. Woodruff School of Mechanical Engineering

Georgia Institute of Technology

December 2018

Extinction droplet sizing measurements in diesel relevant sprays

Approved by:

Dr. Caroline Genzale, Advisor
George W. Woodruff School of Mechanical Engineering
Georgia Institute of Technology

Dr. Devesh Ranjan
George W. Woodruff School of Mechanical Engineering
Georgia Institute of Technology

Dr. Oleksandr (Sasha) Bibik
Daniel Guggenheim School of Aerospace Engineering
Georgia Institute of Technology

Date Approved: November 12, 2018

To my husband, Robert, my parents, Rachel and Abelardo, and my sister, Caroline
for your unwavering love, support, and prayers

ACKNOWLEDGMENTS

diagnostic and being an awesome co-author. I am so thankful to my dear friend, Boni Yraguen. I know that God had a special plan having us join the lab at the same time. I'm so happy that we became friends. I will cherish all the memories: late nights at CNES doing homework and eating popcorn, long days at the lab taking apart the vessel, even longer days taking data and watching heaters fail, endless coffee runs, Friday nights full of work and fun, and celebrating at each other's weddings. I will miss you a ton.

To all my family and friends, especially my parents and sister. I cannot thank you enough for all that you have done for me throughout my life. You have molded me into the person I have become, and I know that I would not have made it here without you. Thank you, Mom and Papi, for loving me, caring for me, and supporting me throughout my life. Thank you for providing me with an excellent Catholic education and for always encouraging me to pursue my dreams. My sister, Caroline, you have blessed my life immensely since you were born. Thank you for being the best sister ever. I miss you every day.

To my wonderful husband Robert, you have been there for me throughout graduate school, always providing love, encouragement, and support. You have been there for me in my most challenging moments and celebrated with me through my successes. You have listened to me talk about my research, asking questions, and providing suggestions. I know that I would have starved in grad school without your excellent cooking. I am so blessed to get to share my life with you. I love you so much.

TABLE OF CONTENTS

LIST OF TABLES

LIST OF FIGURES

LIST OF SYMBOLS AND ABBREVIATIONS

Abbreviations

SAMR	Scattering Absorption Measurement Ratio
SMD	Sauter Mean Diameter
Oh	Ohnesorge number
Re	Reynolds number
LVF	Liquid Volume Fraction
PDPA	Phase Doppler Particle Analysis
USAXS	Ultra-Small Angle X-Ray Scattering
APS	Advanced Photon Source
DBI	Diffuse Back-Illumination
ECN	Engine Combustion Network
FWHM	full width half maximum
SNR	signal-to-noise ratio
CFD	computational fluid dynamics

Symbols

d	droplet size
V	volume
S	surface area
τ	optical thickness
I_o	incident light intensity/radiation
I	attenuated light intensity
l	effective path length
μ	linear attenuation coefficient
ρ	fuel density
$\overline{M}$	projected fuel density
q	scattering vector
λ	wavelength of light/radiation
θ	angle between the incident and scattered x-rays
$\overline{C_{ext}}$	extinction cross section
z	illumination path length
$\overline{\dfrac{\pi d^3}{6}}$	number-weighted mean droplet volume
τ_{meas}	measured optical thickness
τ_{corr}	corrected optical thickness
α	collection angle of the detection system
β	size of droplets in the probe volume

x	size parameter
d_{Lit}	droplet size in literature
d_{633}	droplets exhibiting similar scattering behavior at 633 nm

SUMMARY

A new diagnostic for the quantification of Sauter Mean Diameter (SMD) in high-pressure fuel sprays has been recently developed using combined optical and x-ray measurements at the Georgia Institute of Technology and Argonne National Laboratory, respectively. This diagnostic utilizes liquid scattering extinction measurements from diffuse back-illumination (DBI) imaging, conducted at Georgia Tech, and liquid absorption measurements from x-ray radiography, conducted at Argonne's Advanced Photon Source. The new diagnostic, entitled the Scattering Absorption Measurement Ratio (SAMR), quantifies two-dimensional distributions of path-integrated SMD, enabling construction of the spatial history of drop size development within practical fuel sprays. This technique offers unique benefits over conventional drop-sizing methods in that it can be more robust in optically dense regions of the spray, while also providing high spatial resolution of the corresponding droplet field. The spatially-resolved SMD measurements that result from the SAMR diagnostic will be especially valuable to the engine modeling community for the quantitative validation of spray submodels in engine CFD codes.

The methodology for quantification of SMD distributions using the SAMR technique has been previously introduced. This thesis aims to extend the initial development of the SAMR technique by presenting in detail: the experimental methodologies used in the SAMR technique, including the development of an ideal DBI setup for this technique; the data processing methodologies developed by the author; two-dimensional Sauter Mean Diameter measurements within diesel sprays for various experimental conditions; a summary of the various sources of measurement uncertainty; an assessment for how the sources of uncertainty affect the quantified SMD; and paths to improve the technique moving forward. The SMD results show that for low

ambient density conditions droplets decrease in size as radial and axial position increases. For

high ambient density conditions, however, the droplets show a stable size near the spray

centerline and steadily increase in size as distance from the centerline increases. Additionally,

this work provides 2-D droplet sizing maps which are particularly useful for model validation.

CHAPTER 1

INTRODUCTION AND MOTIVATION

Environmental concerns, health hazards, fuel security, and increasingly strict government emissions regulations have triggered the development of high-efficiency, clean internal combustion engines. Additionally, the US Department of Energy forecasts that overall petroleum consumption will continue to increase despite the decline in petroleum production in the US [1]. The transportation sector is using most of the petroleum. In fact, it is projected that by 2030 the transportation sector will consume 75% of the total petroleum consumed in the US [1]. This signifies that the energy crisis will continue to be an issue in the future. The most cost-efficient, near-term solution is to improve the fuel efficiency of internal combustion engines.

Engine efficiency improvements will require high compression-ratio engines with advanced direct-injection strategies to optimize combustion and thermal energy conversion. Modern engines, both compression ignition and spark ignition, are utilizing direct injection strategies to achieve high fuel efficiency. Improving the fuel injection process in direct injection engines is crucial because it directly controls air-fuel mixing, combustion, and subsequent engine-out emissions [2]. The spray atomization process and the air-fuel mixing process in direct injection engines are linked [2, 3, 4]. Effective atomization promotes high rates of mixing and evaporation [4]. Furthermore, enhanced rates of vaporization and mixing improves fuel efficiency and reduces engine-out emissions [5, 6]. By augmenting the air-fuel mixing process, the ideal charge is prepared for combustion. The air-fuel mixing process is largely governed by the spray atomization process. Thus, developing cleaner and more fuel-efficient engines requires a fundamental understanding of the physical mechanisms governing spray breakup.

1

Because direct injection strategies continue to be a prominent way to improve fuel efficiency, sprays continue to play a critical role in developing high-efficiency clean combustion engines of the future. Despite the importance of sprays in advanced engine technologies, much remains unknown about the physics governing atomization in high-pressure fuel sprays. Within the literature, several mechanisms have been proposed to explain the primary breakup and atomization process of sprays but have never been fully validated [7]. This work aims to address this fundamental knowledge gap in the spray formation process by extending the development of a new diagnostic entitled, Scattering Absorption Measurement Ratio (SAMR) technique to directly measure the formed droplets from the atomization process [7, 8, 9, 10]. This droplet sizing technique combines x-ray absorption and visible-light scattering extinction measurements from Argonne National Laboratory and Georgia Institute of Technology, respectively. The ratio of these measurements, combined with Mie-scattering theory yields 2D volume-projected droplet size distributions in diesel-like sprays within regions of moderate optical thickness [10, 9]. This thesis includes a detailed demonstration of the new technique, by describing the experimental methods, outlining the theoretical development, providing a comprehensive look at the data processing methodology, analyzing the Sauter Mean Diameter (SMD) results, examining and quantifying measurement uncertainties in the SAMR diagnostic, and proposing suggestions for future work.

CHAPTER 2

LITERATURE REVIEW

2.1 Background

In direct injection engines, the spray breakup processes are known to affect engine-out emissions and efficiency [4, 11, 3, 12]. As such, studying and understanding the spray atomization process is crucial. The spray atomization process is a complicated phenomenon which consists of several steps. First, the high-pressure liquid fuel spray is injected through a nozzle into a gaseous environment. When a liquid is injected through a nozzle, the liquid atomizes (forms liquid droplets). These liquid droplets further disintegrate, vaporize, and ultimately undergo combustion in an engine [4]. The spray breakup process is governed by the nozzle geometry, the environment of the gas into which the spray is being injected, and properties of the liquid jet [4]. The spray formation process affects several global spray parameters, such as, cone angle, rate of penetration, spray shape/geometry, etc.

Theoretical work has been done to understand the mechanisms of droplet breakup. The foundation for current spray breakup theories stem from the work on liquid round jets done by Reitz and Bracco [13, 14, 15]. Reitz proposed that four main breakup regimes exist each with different forces acting on the jets, namely liquid inertia, surface tension, and aerodynamic forces [13]. The four breakup regimes are: Rayleigh breakup, first wind-induced, second wind-induced, and atomization [13]. These breakup regimes are determined by the size of the nozzle relative to the size of the droplets formed. In Rayleigh breakup, the droplets are larger than the nozzle. First wind-induced regimes consist of nozzles and droplets on the order of the same size; whereas

second wind-induced regimes have droplets slightly smaller than the jet diameter. Finally, the

atomization regime consists of droplets whose diameters are much smaller than the nozzle

diameter. In the atomization regime, spray breakup commences at the nozzle exit. Figure 1

shows an adapted figure from Reitz's dissertation [15] as published in Magnotti's dissertation

[7], which plots the four regimes as a function of their Ohnesorge and Reynolds numbers. The

Ohnesorge number is a non-dimensional number which relates the relative importance of viscous

forces to surface tension and inertial forces [16]. The Reynolds number is a non-dimensional

number which relates the relative importance of inertial to viscous forces [16]. Figure 1

illustrates that diesel and gasoline sprays typically lie in the atomization regime due to their large

Reynolds numbers. Additionally, diesel and gasoline sprays have nozzle diameters that are much

larger than the droplet diameters.
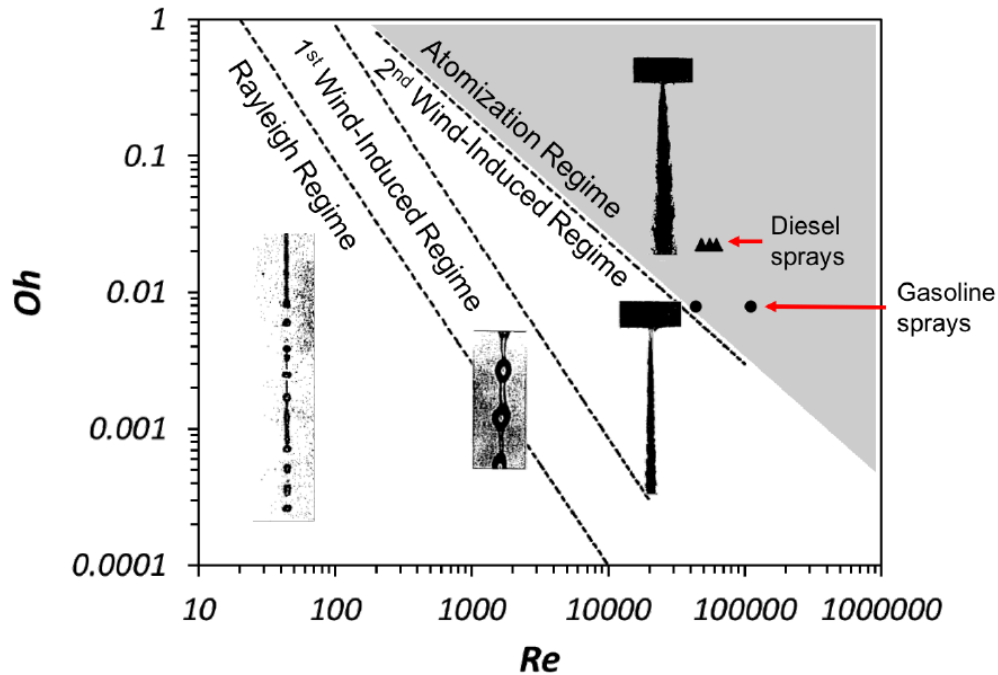
Figure 1: The four breakup regimes in relation to their Ohnesorge (Oh) and Reynolds (Re) numbers

The physical mechanisms driving the spray breakup process vary due to the relative

velocity between the gas and liquid. The aerodynamically induced instabilities theory was

4

proposed as driving the spray atomization process [15, 14] and is currently the most widely accepted theory. The liquid surface is initially disturbed by the fastest growing surface wave, Λ. These disturbances precipitate the formation of droplets that scale in size with Λ [17]. These instabilities grow according to the dispersion relation and ultimately cause the spray to form droplets [13]. Figure 2 shows a schematic representing the aerodynamically induced instability breakup theory [13, 15]. This breakup theory generally holds for sprays in the first and second wind induced regimes where the Reynolds numbers are moderate [7]. It has been suggested that the aerodynamic wave growth theory should also be valid for sprays in the atomization regime. However, other researchers argue that spray breakup in the atomization regime should also consider: the role of turbulence generated in the nozzle, the role of nozzle geometry effects, liquid cavitation inside the nozzle, velocity profile rearrangement, and liquid supply pressure oscillations [7, 14]. Much debate exists over the correct theory to explain the spray breakup process for sprays in the atomization regime, and thus, more experimental research is needed to validate or disprove these theories.
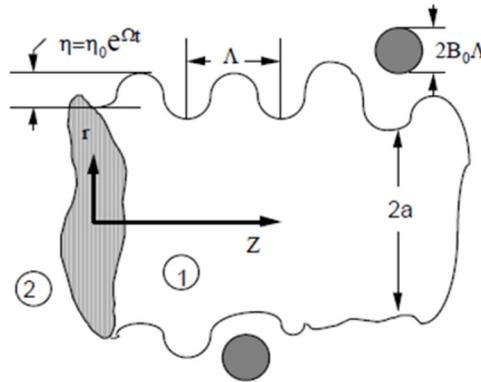
Figure 2: Diagram representing the surface instabilities which drive the spray atomization in aerodynamically induced instabilities breakup theory

2.1.1 Typical Diesel Sprays

Besides the lack of understanding in the physics driving spray breakup in diesel sprays, they are also a challenging measurement environment. Diesel sprays have high droplet number

densities, fast time scales, small length scales, fast velocities and high Reynolds numbers, which make it difficult to directly image a spray and observe the ligaments and droplets formed from spray atomization. In diesel engines, the fuel is injected at incredibly high pressures, from 200-1700 bar [18]. At the time of injection, for typical diesel operation, the combustion chamber environment is at 50-100 bar, around 1000 K and 15 to 25 kg/m^3 [18]. The exit velocity of the fuel is about 500-600 m/s. The expected droplet sizes range from 1-200 μm depending on the nozzle size [4]. Thus, extremely fast time scales and small length scales make many diagnostics ineffective at measuring diesel spray droplet sizes. In addition, the overall scale of a diesel spray plume is rather small. Typically, diesel plumes extend axially up to 50 mm and radially about 2-3 mm. Additionally, diesel injection durations are generally less than 8 ms, thus requiring high speed imaging to be able to capture the injection event. Thus, the severe environment of diesel sprays limits the available spray droplet sizing diagnostics to understand the spray atomization process.

2.2 Spray Droplet Sizing Diagnostics

To better understand the spray atomization process and determine the most appropriate spray breakup theory, quantitative experimental measurements are necessary. Directly observing the spray breakup process is difficult due to high droplet number densities, small length scales, and fast time scales [10]. Several droplet sizing measurement techniques exist, each with their respective advantages and disadvantages, which will be presented in this chapter.

2.2.1 Long Distance Optical Microscopy

Crua and co-workers at the University of Brighton have developed a high-speed microscopic imaging technique that images diesel sprays with high spatial and temporal resolution [19, 20, 21]. They used a rapid compression machine and common rail diesel injector

to achieve ambient pressures up to 80 bar and injection pressures up to 1600 bar [19]. They used a long-distance microscope and collection imaging optics which produced a projected pixel size of .6 μm/pixel with a viewing region of 768 by 614 pixels [19]. They used a diffuse frequency-doubled Nd:YAG laser to produce blur free and speckle free shadowgraphic images of the diesel spray. Additionally, a high-speed video camera was used to capture movies of the spray formation process. Figure 3 shows an example of the still images produced from the setup. The high spatial resolution of the image allows droplets and ligaments from the spray to be measured.
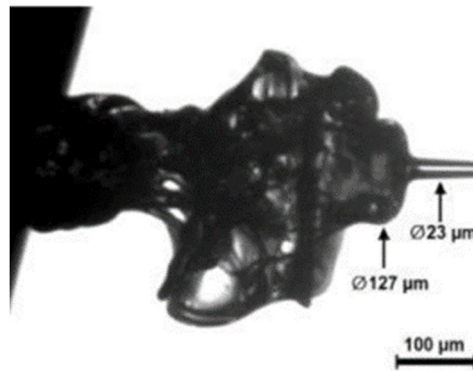
Figure 3: A ligament at the interior of the jet [19]. The base of the ligament measures 127 μm.

In a more recent work by Crua and co-workers, the near-nozzle region of diesel and biodiesel sprays were imaged using blur-free shadowgraphic images to measure droplet sizes [20]. The experimental setup consisted of a Delphi common rail system, high pressure fuel system and a seven-hole DFI-1.3 injector from Delphi [20]. The cylindrical nozzle had a diameter of 135 μm. The experiments were taken at atmospheric ambient density with the fuel being injected at 1000 bar. A diffused double-pulsed Nd:YAG laser was used to illuminate the spray. A long-range microscope and dual-frame CCD camera captured the images of the spray. The image size was 593x784 μm which captured up to 15mm downstream of the nozzle and 300 μm radial distance from the spray axis. Thus, the projected pixel size was .57 μm/pixel. Figure 4 shows an example of the images captured from this imaging system. Additionally, Figure 4

shows the high droplet number density of the spray, which makes direct observation using this technique limited to regions along the periphery of the spray. A variety of droplet detection algorithms were used to ensure that very small droplets or droplets out of focus could still be detected and their diameters measured. The droplet's equivalent diameter is calculated using, $d = 2\sqrt{A/\pi}$. The surface area, A, is captured from the images.

Dual frame at nozzle exit (dt = 400 ns)   10 mm (0.3 mm off-axis)   15 mm (0.3 mm off-axis)
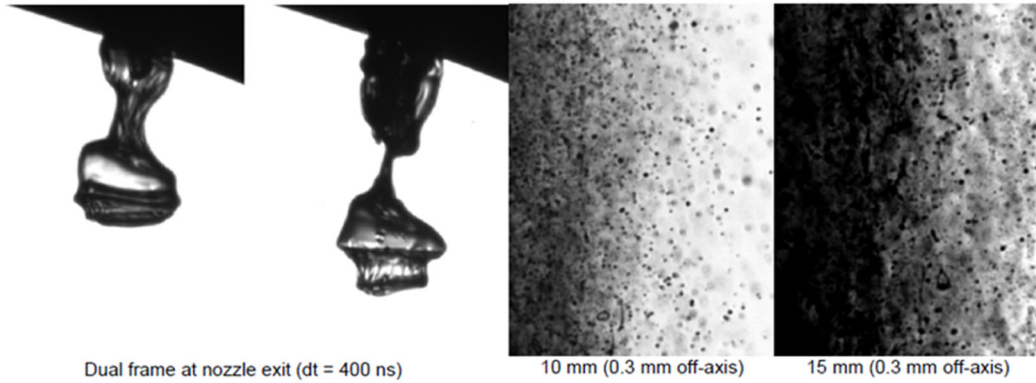
Figure 4: The shadowgraphic images for rape methyl ester fuel at the nozzle exit, 10mm downstream, and 15 mm downstream (left to right) [19]

Some statistical analysis was done to calculate the droplet size distribution for the two fuels. 200 images were recorded per test with an average of 600 droplets per image [20]. Based on the viewing region and the depth of field the average droplet density was calculated to be 1300 drops/mm^2 and volumetric droplet density of 65,000 drops/mm^3 [20]. The results indicate that 10 mm away from the nozzle the droplet size distributions peak at 2 μm for both fuels, which the authors attribute to secondary atomization [20]. From these high-resolution images, they can calculate the fuel droplet sizes.

Crua's work shows great progress in direct imaging of diesel relevant sprays. He is able to achieve either high frame rate low resolution movies or high resolution still images of diesel sprays [19, 20, 21, 22]. The images also provide a large field of view. However, there are some disadvantages to this spray diagnostic. For example, this experimental technique is generally limited to low jet velocities, less than 100 m/s [21]. Thus, they are only capable of producing

blur-free high-resolution images of diesel sprays at the start of injection when the jet velocity is slower than during the rest of the injection [22]. Additionally, it is limited to the periphery of the spray where individual droplets can be imaged [20]. When applying the droplet detection algorithm, the maximum number of droplets must be detected accurately. This is difficult in the dense polydisperse regions of the spray, which is why the technique is mostly applied at the spray periphery [20]. Thus, direct imaging of diesel sprays may not provide the most efficient path to understanding spray droplet size evolution in space and time.

2.2.2 Multiple-Wavelength Extinction Measurements

Parker, Labs, and co-workers at the Colorado School of Mines developed multiple-wavelength extinction experiments which allow them to measure the fuel droplet sizes and liquid volume fraction (LVF) [5, 6, 23]. They used scattering measurements using lasers with infrared wavelengths. Employing infrared wavelengths allows for optically thick sprays to be studied because extinction cross sections are lower for longer wavelengths [5]. They take a ratio of the Beer-Lambert law for the two different infrared wavelengths to calculate the liquid volume fraction and Sauter Mean Diameter [5]. They analyzed dodecane, diesel, and methyl oleate fuel sprays injected through a 310 μm diameter nozzle at 620 bar into an ambient temperature and pressure environment [5]. During the steady portion of the spray, they measured SMDs 2-3.25 μm at the centerline and 6-8 μm at the spray periphery for all three fuels as seen in Figure 5 [5].
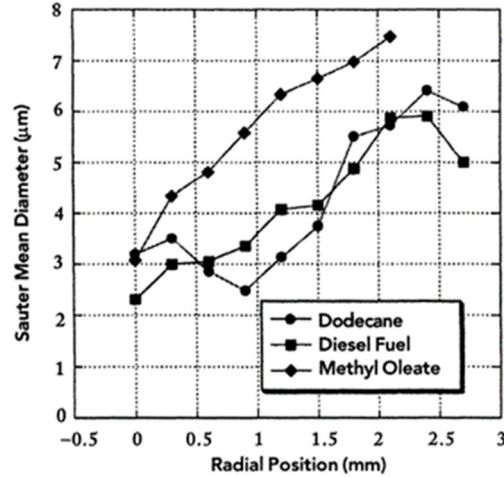
Figure 5: At an axial location of 25 mm, SMDs as a function of radial position for all three fuels

In a later work by Labs and Parker, they used a scattering absorption measurement using lasers with infrared wavelengths [23]. As before, they take a ratio of Beer Lambert law for the two different infrared wavelengths to find the LVF and SMD. They conducted their experiments at atmospheric temperature and pressure (300 K, 1 bar) and at 873 K ambient temperature and 12.5 bar ambient pressure. For both cases, they injected fuel through a 160 μm nozzle at a peak injection pressure of 800 bar. The other aspects of the experimental setup are the same as their previous work [5]. They collected data at the spray centerline every 5 mm starting at 15 mm ending at 45 mm. Figure 6 shows an example of their droplet sizes and LVF results for the steady period of the injection event. The droplets tend to increase in size as axial distance increases and as radial distance increases (not shown here). This data set is useful because it provides detailed droplet sizing information throughout the entirety of the spray.
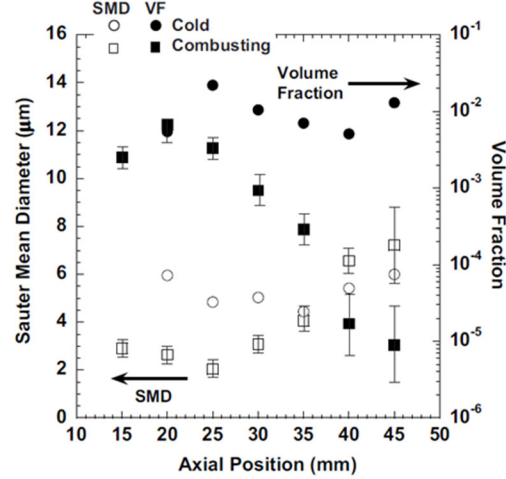
Figure 6: The SMDs and volume fraction for combusting and cold cases at the spray centerline as a function of axial position

Overall, the work of Parker and Labs advanced spray droplet sizing diagnostics by providing much-needed spatial and temporal droplet sizing information. Providing droplet information in the dense, optically thick regions of the spray is advantageous because typical light scattering measurements and direct imaging of the spray cannot be used in these regions due to the high droplet number density. However, they did not thoroughly measure or quantify the effect that multiple scattering has on the optical thickness measurement [6]. Instead, they did a simple approximation to establish upper and lower bounds for the attenuation correction [6]. This was done by evaluating the extinction of the beams with the scattering signals for 9.27 µm scattering at 11° and 1.06 µm scattering at 90° [6]. The upper and lower limit on attenuation is used to estimate the upper and lower limit on droplet size. Thus, this also limits the droplet sizes that can be measured. Additionally, the two-laser scattering experimental setup can be difficult to employ. The laser beams must be properly focused to produce overlapping co-axial beam waists [5]. If this technique is employed in a pressure vessel, special windows are required which can transmit both infrared and visible radiation [5, 23]. Because the experiments use a laser-based technique, it can be time consuming to travel axially and radially throughout the spray. Without doing so, a complete picture of the spatial evolution of the droplet size could not be achieved.

Thus, while this technique is useful in providing detailed droplet information in diesel relevant sprays, it has some limitations in experimental setup and some large sources of uncertainty in the regions of high optical thickness.

2.2.3 Phase Doppler Particle Analysis (PDPA)

Phase Doppler Particle Analysis (PDPA) is one of the most useful and commonly employed drop sizing measurements in spray applications because it can measure time averaged droplet size, velocity, number density, and volume flux simultaneously [24, 25, 26, 27]. PDPA utilizes two intersecting coherent laser beams to create a small measurement volume for probing individual droplets [24, 26]. When the two incident laser beams interact with the particle, the light is scattered. The measured Doppler signal is recorded at different scattering angles, which results in a change in phase modulation. This change in phase modulation is proportional to the diameter of the particle [26, 28].

Payri and co-workers at CMT Motores Térmicos at Universidad Politécnica de Valencia established an optimal PDPA measurement to characterize injection events from a diesel nozzle, which allowed them to measure time resolved droplet sizes [27]. The experimental conditions for the study were injection pressures 300 to 1300 bar and ambient density from 1.2 to 40 kg/m^3 [27]. A TSI PDPA system was used with a measurable frequency from 300 Hz to 175 MHz, a minimum transit time of 50 ns, and a maximum sampling rate of 800 MHz [27]. The other specifications of the setup can be found in the paper. The receiver slit width was varied from 25 to 100 μm because significant improvements occurred as slit width decreased [27]. The slit width had a large effect on the detection of droplets. The droplet sizes and velocities are shown in Figure 7 as a function of time for the 300 bar injection pressure 50 mm downstream and 1 mm off-axis of the nozzle [27]. The droplets are larger near the initial transient phase of injection.

This plot, however, does not show any spatial information about droplet size. Additionally, 50 mm downstream is quite far from the regions where spray breakup exists.
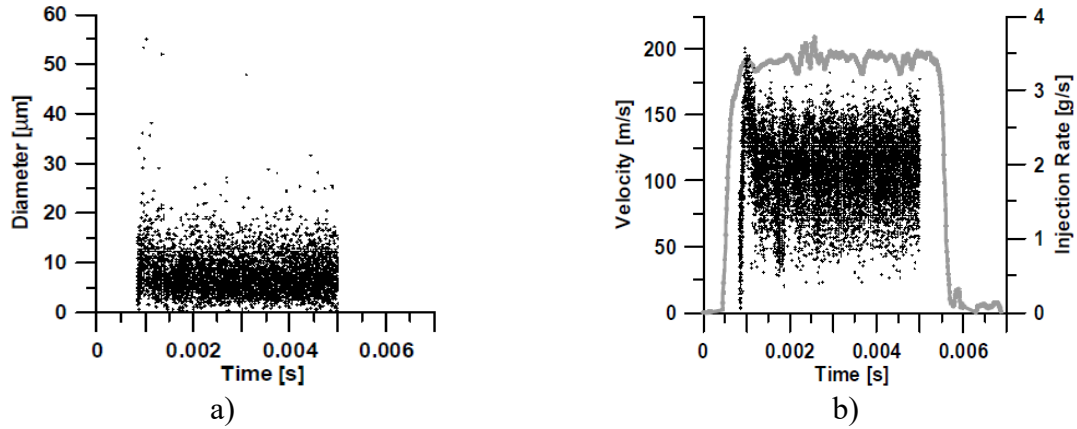
Figure 7: The a) droplet diameters and b) velocities as a function of time for $P_{inj}=300$ bar, $P_{amb}=1$ bar at an axial location of 50 mm and a radial position of 1 mm

Araneo and Tropea from the Technical University of Darmstadt also sought to improve PDPA measurements made in diesel relevant sprays [29]. Their experimental setup consisted of a Bosch common rail Diesel system, a 190 μm single hole nozzle injector and a commercial Dantec PDPA system. A long injection duration was used so that the steady portion of the spray could be investigated. This is often difficult to do with PDPA because the optical density of the spray is much higher during these steady times. The fuel was injected at 300 bar into an atmospheric temperature and pressure environment. They investigated the effect that the laser power, the photomultiplier voltage, the SNR validation threshold and the density of drops had on the measured droplet sizes and the droplet size distribution [29]. The measured droplets are all less than 30 μm. Figure 8 shows an example of the droplet sizing results for this setup. They optimized the PDPA setup such that 1500 single droplets were measured per injection and high temporal resolution was achieved. While this work is valuable in optimizing PDPA, it is still limited to ambient conditions due to the difficulties that windows in a pressure vessel would cause.
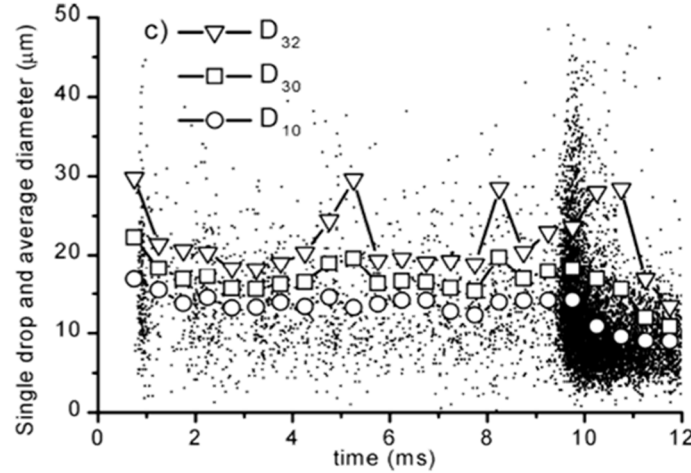
Figure 8: Raw droplet size information as a function of time

Some advantages to PDPA are that it is non-intrusive, usually has high accuracy and spatial resolution, and is an absolute measurement, meaning it does not need to be calibrated with another measurement [26]. Phase Doppler anemometry only applies under certain conditions, however. The particle must be spherically homogeneous and dominated by only one scattering mode [26]. When non-spherical particles are measured, errors are introduced, which can overestimate the droplet diameters up to 45% [28]. Additionally, difficulties arise when dense turbid media are measured [27]. The likelihood of multiple droplets existing within the probe volume are high within high optical thickness sprays [28, 29]. This produces overlapping signals which can often be unprocessable, thus yielding invalid measurements [28, 30, 29]. Also, in dense regions of the spray the signals can be very noisy which results in a low data acquisition rate [29]. Because PDPA can only measure single droplets at a time, number density and 3D measurements are not available. Therefore, previous PDPA measurements conducted in diesel-like sprays have been limited to locations far downstream of the nozzle [27], far away from the primary breakup region. Also, because PDPA is a pointwise measurement, it can be very time consuming to generate a multi-dimensional scan of the spatial droplet size distribution and understand the spray breakup process [24]. In addition, it is often difficult to incorporate the

14

diagnostic in a pressure vessel due to the requirement of optical access from two directions [27].

Thus while PDPA is useful because it can measure droplet size and velocity simultaneously, its

numerous disadvantages make it impractical to employ under diesel relevant conditions.

2.2.4 Ultra-Small Angle X-Ray Scattering (USAXS)

More recently, a new x-ray diagnostic, ultra-small angle x-ray scattering (USAXS), has

been applied to diesel sprays to measure droplet sizes [31]. USAXS relies on the high brilliance

synchrotron x-ray beam from the Advanced Photon Source (APS) at Argonne National

Laboratory to probe the spray structure and measure droplet sizes in diesel sprays [31, 32, 33].

The x-rays are scattered by the electrons in the fuel and the resulting scattering pattern is related

to the particle shape and size. X-rays can penetrate the measurement beam through optically

thick droplet clouds, enabling the use of USAXS in near-nozzle locations of diesel sprays. The

USAXS measurement is capable of measuring the surface area of the droplets throughout the

entirety of the spray [34]. X-ray radiography measurements of projected density are used in

conjunction with the surface area measurement to quantify the SMD of the fuel.
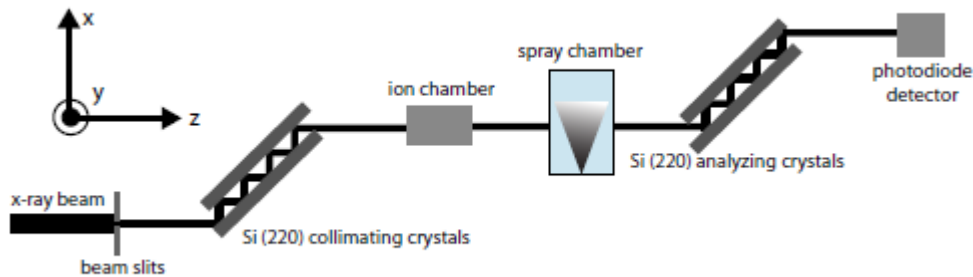
Figure 9 Schematic of the ultra-small angle x-ray scattering setup [39]

The experiments were conducted at the APS using the 9-ID beamline for the surface area

measurements and the 7-BM beamline for the projected density measurements. For both

experiments, the fuel injector was mounted horizontally in a high-pressure spray chamber fitted

with a pair of x-ray transparent windows [10, 9, 34]. The chamber was held at room temperature and pressurized with nitrogen. A light-duty common rail diesel system and high-pressure fuel system was used [34]. Figure 9 shows the x-ray beam emits from the synchrotron, passes through the beam slits, and enters the silicon collimating crystals. The collimating crystals are used to focus the beam to a 500 x 50 μm beam size and minimize the angular divergence [34]. The incident intensity was recorded with an ion chamber. The attenuated intensity was measured at defined angles with a pair of analyzing silicon crystals and photodiode. The x-rays are scattered by the electrons in the fuel and the resulting scattering pattern is related to the particle shape and size. The scattering vector is related to the measured attenuated x-ray intensity I(q). Ultimately, the surface area, S_p, is calculated using the Irena USAXS data reduction and analysis package [34, 32]. Finally, the SMD can be related to the volume of droplets (from radiography) and the surface area of the droplets (from USAXS) using equation 1.

$$d = 6\frac{V}{S} \tag{1}$$

USAXS is a valuable spray droplet sizing measurement because it provides droplet sizes in regions that are mostly unachievable with optical diagnostics due to the high optical thickness of the spray. However, USAXS is a time consuming and resource-intensive diagnostic because each spray measurement location requires a measurement of the scattering signal over a full sweep of scattering angles, resulting in high data throughput requirements. This has limited previous measurements to just a few locations along the spray axis [31]. Additionally, most laboratories do not have access to the high brilliance synchrotron x-rays that are used for USAXS, which makes widespread use of this diagnostic impractical. This diagnostic shows clear advantages in probing high optical thickness sprays and is thus likely to help advance new knowledge on primary breakup and atomization in diesel sprays. It is limited, however, in its

ability to provide a complete spatially resolved picture of the drop size evolution and distribution. Nevertheless, USAXS will be used as validation data to assess the accuracy of the SAMR SMD results in Chapter 4.

2.2.5 Scattering Absorption Measurement Ratio Technique (SAMR)

Magnotti and Genzale have used extinction measurements to measure droplet sizes in diesel relevant sprays. This technique, called Scattering Absorption Measurement Ratio (SAMR), uses visible light extinction and x-ray radiography measurements in conjunction and application of Mie theory to quantify the SMD values [7, 8]. Visible laser extinction (VLE) is a line of sight extinction measurement. It used a 633 nm HeNe laser which passed through the spray. The attenuated light intensity was captured with a photodiode. The optical thickness can be quantified from these experiments using the Beer-Lambert law. The laser and optics were mounted on a traverse which allowed the measurement to be taken at distinct axial and radial positions [7]. Figure 10 shows the experimental setup used.
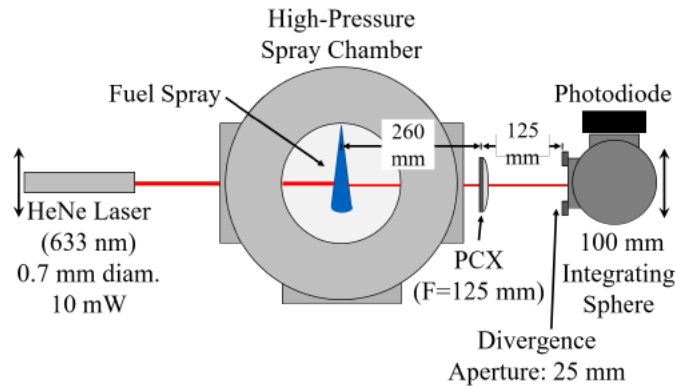
Figure 10: Schematic of visible laser extinction measurements

One main drawback to this technique are that it is limited to measuring the droplet sizes at very few points in the spray due to the time-consuming nature of rastering the spray. This SAMR demonstration by Magnotti was a proof of concept. This thesis extends the work of

Magnotti and is able to quantify the SMDs throughout the spray by using the diffuse back-illumination technique as the scattering-based technique.

2.3 Objectives of the thesis

The ideal diagnostic for studying atomization and measuring droplet sizes in high-pressure fuel sprays would:

1) perform under moderate to high optical thickness environments

2) accurately measure small droplet scales (1-20 μm)

3) provide high temporal resolution

4) provide 2D spatial resolution of the droplet size distribution throughout the spray

A spray droplet sizing diagnostic that could satisfy most of these conditions would provide a more complete picture of the spray phenomena, and thus help to answer the questions about the mechanisms driving spray formation in engine-relevant sprays. Ideally, this diagnostic would also accomplish these goals with a modest level of time and equipment resources. This thesis presents the Scattering Absorption Measurement Ratio technique, which utilizes a ratio of Diffuse Back-Illumination measurements (from Georgia Institute of Technology) and X-Ray Radiography measurements (from Argonne National Laboratory) to quantify the Sauter Mean Diameter in diesel relevant sprays. This is an extension of the work done by Magnotti [7]. This thesis shows 1) the SAMR diagnostic in wider practice, 2) develops and improved setup, 3) refines the post-processing steps required, and 4) quantifies uncertainties of the technique. SAMR satisfies most of these aforementioned requirements and has the potential to be a useful diagnostic to help better understand spray atomization.

The objective of this thesis will be to:

a) Explain in detail the experimental methodologies used in the SAMR technique

a. Develop the ideal DBI setup to measure the optical thickness of the spray

b) Present a brief explanation of the theoretical development of the technique

c) Demonstrate the data processing methodologies developed by the author

d) Present two-dimensional Sauter Mean Diameter measurements within diesel sprays for various experimental conditions and uncertainties associated with this measurement

e) Suggest paths to develop the technique moving forward

CHAPTER 3

EXTENDING THE DEVELOPMENT OF THE SCATTERING

ABSORPTION MEASUREMENT RATIO (SAMR) TECHNIQUE

The Scattering Absorption Measurement Ratio (SAMR) technique utilizes a light scattering extinction measurement and x-ray radiography absorption measurement to quantify the mean droplet size in a given probe volume, or the Sauter Mean Diameter (SMD). This technique has been previously developed and demonstrated in a proof-of-concept study by Magnotti [7, 8]. Each of the experimental diagnostics used for the technique will be elaborated upon in the following sections. In addition, the theory used to derive this technique will be briefly presented. The various data processing steps developed to jointly process the two data sets will also be expanded on.

3.1 Diffuse Back Illumination Experiments

The SAMR technique employs a light scattering extinction measurement to quantify the optical thickness/depth of the spray; a line-of-sight beam measurement or diffuse back-illumination (DBI) measurement can be used. Previously, Magnotti used a line-of-sight measurement, called visible light extinction. However, diffuse back-illumination was selected as the method for measurement of light scattering extinction for this thesis. DBI has some advantages compared to VLE like, increased data throughput due to the two-dimensional nature of DBI and improved spatial resolution. (.5mm/pixel vs .08mm/pixel).

3.1.1 Experimental Facility and Operating Conditions

Diffuse back-illumination experiments were conducted at Georgia Tech in the SPhERe Lab. The SPhERe Lab is equipped with a high-pressure, high-temperature continuous flow spray chamber, which can reach pressures and temperatures up to 100 bar and 900 K, respectively. Highly characterized engine relevant conditions can be achieved in this spray chamber. Ambient densities can be simulated that are representative of typical diesel engine operation. Also, the vessel can reach temperatures that simulate low temperature combustion, an emerging engine technology. Additionally, the spray chamber is optically accessible. Two quartz windows on the left and right side of the vessel enable multiple optical diagnostics to be employed. Other institutions like Universidad Politécnica Valencia and Caterpillar utilize similar continuous flow vessels [35]. A schematic of the spray chamber is shown in Figure 11. Compressed air flows through the bottom of the chamber, up through the test section, and leaves the top through the exhaust. Three windows are shown in this schematic, but for the DBI tests only the two side windows were used.
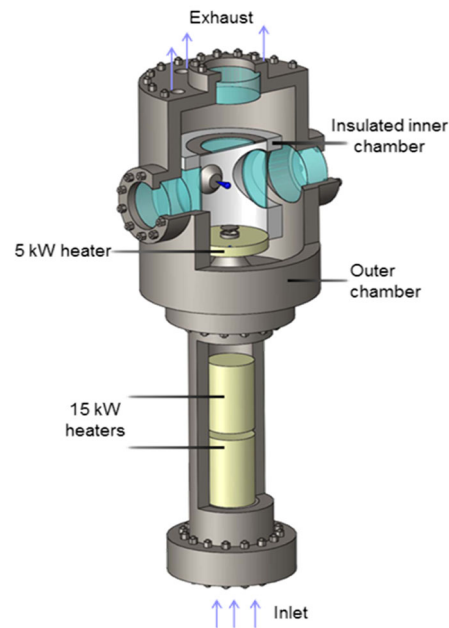
Figure 11 High-pressure high-temperature spray chamber at Georgia Tech

This thesis work consisted of three phases; each phase sought to improve the diagnostic setup used in the previous campaign and to reduce measurement uncertainties. Phase I and III of this work used the Engine Combustion Network (ECN) Spray D injector with a 186 μm nominal outlet diameter, whereas Phase II used the Spray A injector with a 90 μm nominal outlet diameter. A Maxpro Technologies pneumatic high-pressure fuel pump, capable of pressurizing liquid fuels to 410 MPa, was used to pressurize the fuel [36]. A Bosch common-rail diesel system was used. Phase I and II used dodecane for fuel while phase III used viscor.

3.1.2 Optical Setup

The DBI imaging technique was based on the work by Westlye et al. [37]. The DBI setup creates a diffuse light source to illuminate the spray field. An extended and spatially uniform light source with constant radiance is desired to maximize the light throughput [37]. A Photron SA-X2 camera with a CMOS image sensor was used to measure the intensity of incident and attenuated light. The image sensor provides enhanced imaging performance [38]. It has a high light sensitivity which is crucial in high speed imaging [38]. The full dynamic range of the camera should be utilized to maximize the sensitivity of the diagnostic [37].

The Beer-Lambert law is used to relate the attenuation of light through a material. Light attenuation includes absorption and scattering. The optical thickness (τ) can be calculated using the Beer-Lambert law which relates the incident light intensity (I_o) to the attenuated light intensity (I) using the following equation,

$$\frac{I}{I_o} = e^{-\tau} \tag{2}$$

$$\tau = -\ln\left(\frac{I}{I_o}\right) \tag{3}$$

The 2-D line-of-sight optical thickness maps were developed using equation 3. A high power, pulsed LightSpeed Technologies LED served as the light source for these DBI experiments. The LED illuminates the chamber before the fuel injection begins enabling a 2-D measurement of I_o. After the start of injection, the high-speed camera records the attenuated light, I, after the light passed through the chamber and interacted with the spray [16]. At the wavelength used for this work, the light only scatters after interacting with the fuel droplets.

Figure 12 shows the schematic of the experimental setup utilized for the DBI experiments. Table 1 shows the dimensions of the illumination optics. This setup follows the recommendations of Westlye and co-workers for DBI used in diesel relevant sprays employed in high-pressure high-temperature spray chambers for Phase I and II of the data campaigns. However, for Phase III the DBI setup diverged from strictly following the DBI setup recommended by Westlye to create an ideal DBI setup for the SAMR technique. See section 3.1.3 Experimental Conditions for further elaboration on this point. Table 2 shows the camera and light source settings for each phase of the work.
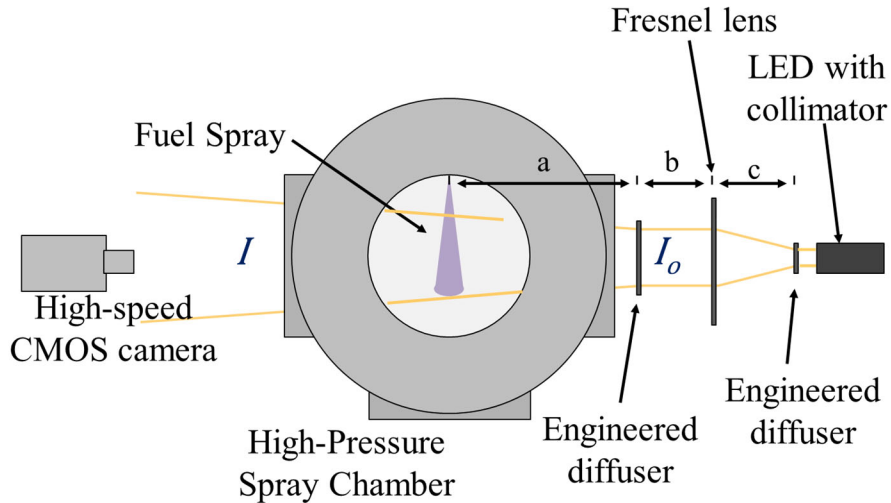
Figure 12: Diffuse back illumination schematic employed for the SAMR technique

Table 1: Dimensions for DBI setup for each phase of the work

	Phase I	Phase II	Phase III
a	250 mm	250 mm	258 mm
b	140 mm	140 mm	640 mm
c	152 mm	152 mm	180 mm

Table 2: Camera and light source settings for all phases of the work

	Camera Lens	Camera Frame Rate	LED pulse rate	Pulse width	Half Collection Angle	Projected Pixel Size
Phase I	50mm f/1.2	72,000 fps	36,000 fps	90 ns	4.85°	77.7 μm/pixel
Phase II	50mm f/2.8	72,000 fps	36,000 fps	52 ns	4.16°	94.6 μm/pixel
Phase III	85 mm f/1.8	72,000 fps	72,000 fps	78 ns	3.67°	66.0 μm/pixel

Figure 13 shows the 2-D measured optical thickness map from the DBI experiments for Spray D ρ_{amb} = 1.2 kg/m³ P_{inj} = 50 MPa. The DBI data is time averaged to attain the steady portion of the spray and ensemble averaged to reduce errors associated with shot-to-shot variation.
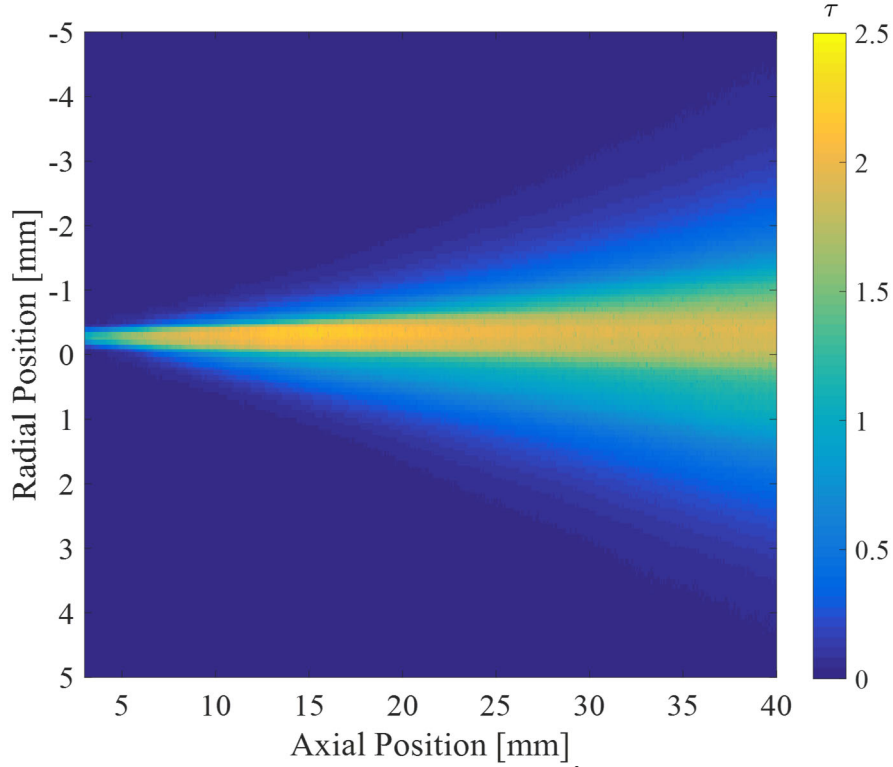
Figure 13: 2-D optical thickness map for Spray D ρ_{amb} = 1.2 kg/m³ P_{inj} = 50 MPa condition with a 120° injector orientation with the shaded pulsed setting

3.1.3 Experimental Conditions

As mentioned previously, this work consisted of three phases; each phase sought to improve the diagnostic setup used in the previous campaign and to reduce measurement uncertainties. Table 3 provides a summary of experimental conditions of each phase of the work.

Table 3: DBI experimental campaigns conducted over the course of this work

	Injector	Light Source	Ambient Density	Injection Pressure	Injector Orientation	Objective
Phase I	Spray D #209133	White LED	1.2, 2.4, 22.8 kg/m³	50, 150 MPa	0°	To develop the SAMR processing steps
Phase II	Spray A #306020	Red LED 633 nm	22.8 kg/m³	50, 100, 150 MPa	0°	To improve the light source and use a smaller nozzle size
Phase III	Spray D #209133	Red LED 633 nm	1.2, 5.8 kg/m³	50, 150 MPa	90, 120, 165°	To improve the DBI setup, reduce the SNR in radiography, to assess the asymmetries in the spray

Phase I was the first time that this SAMR diagnostic technique was comprehensively demonstrated. Thus, it served as a proof of concept. For phase I, the main objective was to establish the experimental setup for both diagnostics at each facility and to develop the data processing steps necessary to quantify the SMD. During phase I, the spray was illuminated with a white LED. Using a white LED, however, is not ideal because it contains a range of light wavelengths from 390 to 700 nm. This is problematic when calculating the extinction cross section using MiePlot, which will be elaborated upon in section 3.4. The built-in shading function on the camera was used to account for dark noise.

The objective of phase II was to use an improved light source and to measure spray atomization using a smaller nozzle size (90 µm vs 186 µm). For phase II, the experimental setup was improved by using a red LED with 633 nm illumination wavelength. Using a light source with a single wavelength is beneficial since it is necessary to input one illumination wavelength into MiePlot (see section 3.4). The built-in shading function on the camera was not used because it was suspected that the camera software was overestimating the noise floor. This overestimation of the noise floor would result in a loss of quantitative data. However, not using the shading calibration also results in a loss of dynamic range. The dark noise of the sensor without the shading function enabled is about 1000 counts, resulting in a 24.4% loss of dynamic range (4095 counts).

Phase III aimed to better understand the asymmetries in the spray by conducting the experiments at multiple viewing angles. Additionally, the signal to noise ratio for the radiography measurements were improved by using Viscor calibration fluid doped with Cerium. For the DBI experiments, Viscor calibration fluid was the fuel used. For phase III, the data was

taken with a red 633 nm LED with the shading correction disabled and enabled. In addition, the

DBI setup was significantly improved by creating a more uniform and diffuse light source.

For Phase I and II, the LED was pulsed at a rate half that of the camera frame rate

according to the recommendations presented by Westlye in a presentation he gave at the ECN 4

workshop [39]. With this skip pulsed configuration, the noise would reset every other frame, thus

reducing the effect of ghosting. In future publications by Westlye [37], he pulsed the LED at the

same rate as the camera frame rate. Phase III included data sets at both skip pulsed and pulsed

configuration. Figure 14 shows a schematic of the pulsed and skip pulsed settings.
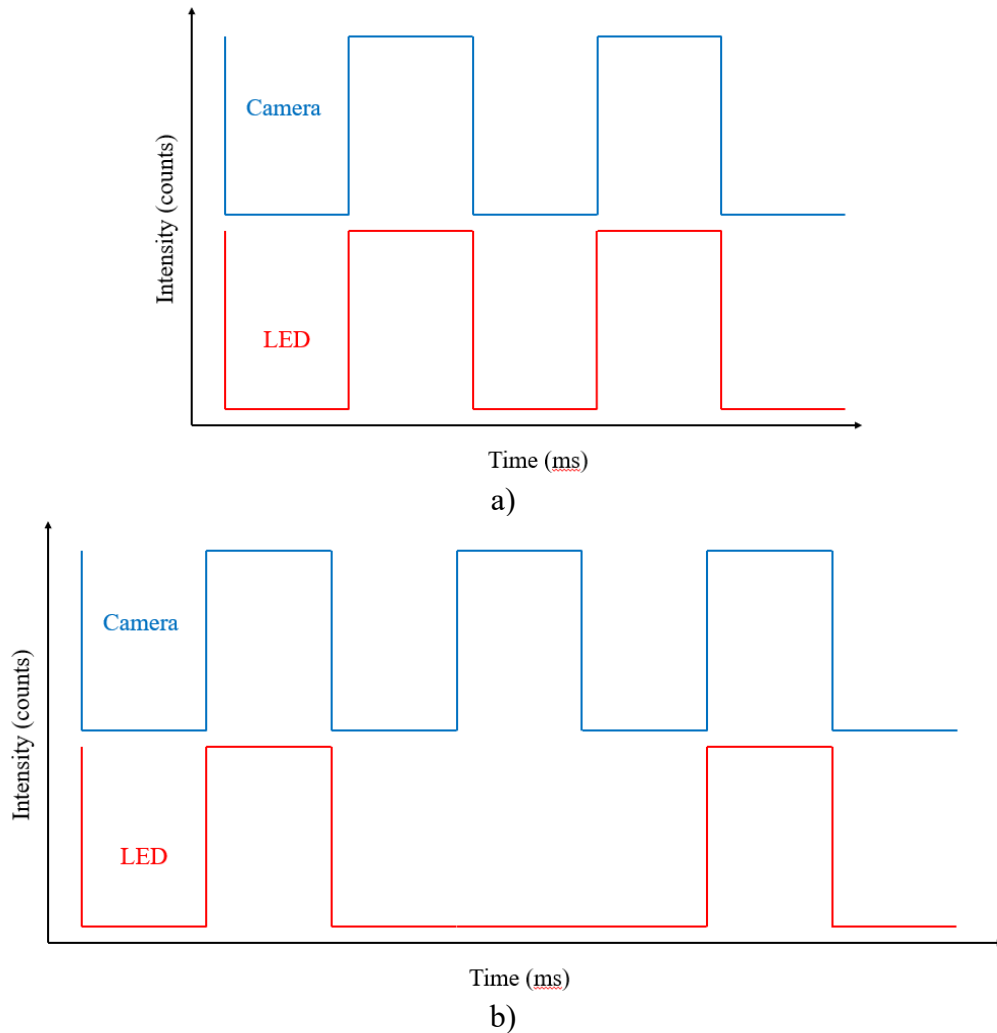
Figure 14: Schematic demonstrating the a) pulsed and b) skip pulsed configurations

3.1.4 Optimization of DBI Illumination Strategy

To assess the optimal DBI setup, it was necessary to identify another measurement of optical thickness with which to compare each illumination strategy (shaded pulsed, shaded skip pulsed, unshaded pulsed, and unshaded skip pulsed). This was done by imaging neutral density filters using a similar DBI setup. Neutral density filters are absorption filters with known optical density values. The optical density/thickness of the filters are measured on a base-10 log scale, which was converted to a natural log scale to compare with the DBI experiments. The results of each configuration were compared with the known optical density value from the filter. Figure 15 shows the optical setup used to calibrate the DBI diagnostic.
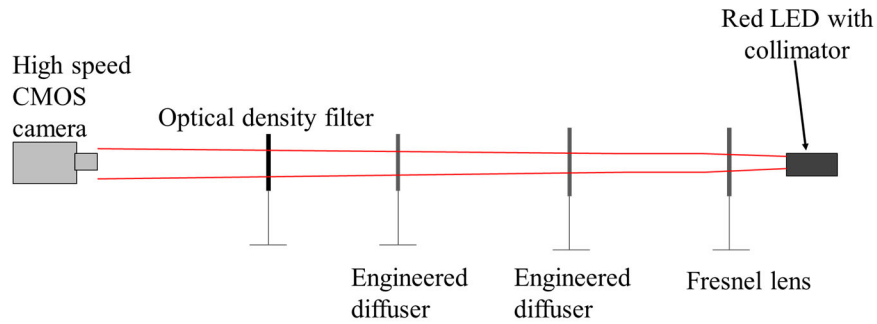
Figure 15: The setup for the DBI calibration

The DBI calibration test was conclusive that using the shading calibration from the camera showed the best agreement with the optical thickness of the neutral density filters. Figure 16 shows that although most of the measurements lie within the error bars of the neutral density filters, both unshaded configurations show the greatest deviation from the mean value. Table 4 shows the results for all the configurations as well as the percent differences between the DBI technique and the neutral density filter. In general, the shaded setting shows better agreement with the filter, especially as the measured optical thickness value increases. For example, at $\tau=6.9$, the unshaded pulsed and unshaded skip pulsed show 12% and 10.6% deviation from the accepted value, respectively. Additionally, with the shading calibration on, the camera sensor can

utilize its full dynamic range. Using the full dynamic range provides the maximum sensitivity of the measurement [37].

Figure 17 shows a comparison between the shaded pulsed and shaded skip pulsed configurations. Both settings show good results with the optical depth of the filter. The skip pulsed setting was initially used to conform to ECN 4 guidelines [39]. It was suggested that residual charge was carried over from previous frames, thus affecting the signal intensity of the frame. It was proposed that by including a dark frame between each light frame the noise floor could be reset. In subsequent work by Westlye et. al., the LED was pulsed [37]. Thus, it was decided to pursue the shaded pulsed configuration, which was used for the Phase III data set.
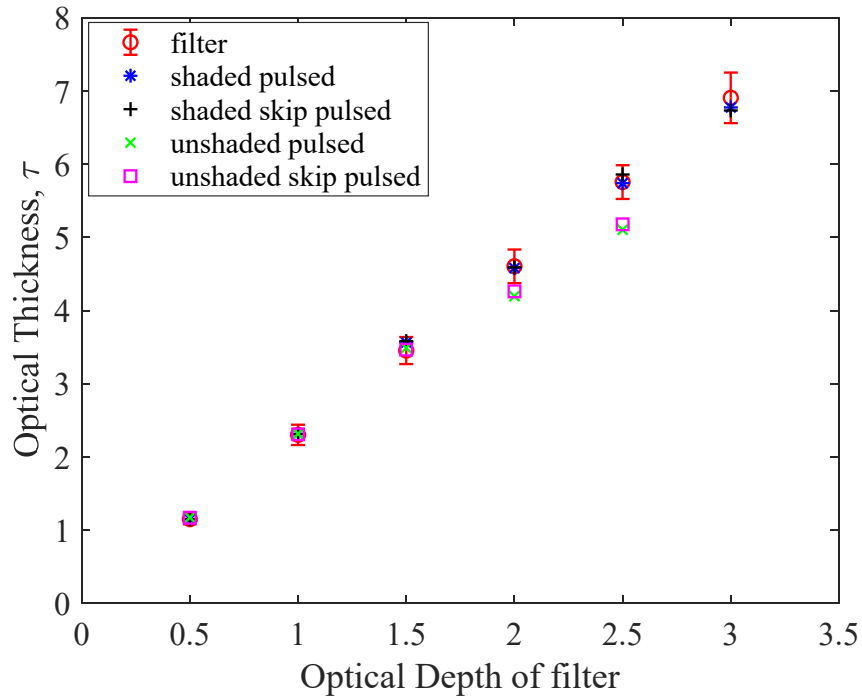
Figure 16: Results of the DBI calibration for all four settings

Table 4: Comparing camera configurations with neutral density filter

OD	τ filter	Shaded pulsed % difference	Shaded skip pulsed % difference	Unshaded pulsed % difference	Unshaded skip pulsed % difference
.5	1.2	.08	.05	1.9	1.7
1.0	2.3	.6	.4	.6	.3

1.5	3.5	3.1	3.7	1.0	.4
2.0	4.6	.5	.3	9.3	7.7
2.1	4.8	1.7	1.2		
2.2	5.1	2.9	2.2		
2.3	5.3	3.4	1.9		
2.4	5.5	1.5	1.5		
2.5	5.8	.3	1.8	12.0	10.6
3.0	6.9	1.9	2.5		
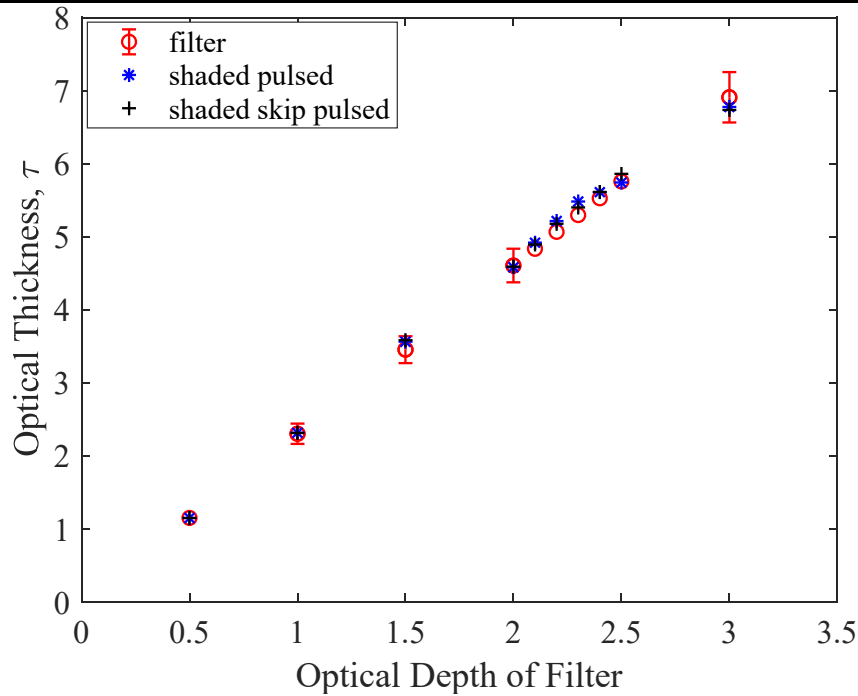
Figure 17: Results of the DBI calibration for the shaded pulsed and shaded skip pulsed

3.2 X-Ray Radiography Measurements

X-ray radiography measurements were taken by our collaborators at Argonne National

Laboratory. The path-integrated liquid fuel mass distribution, namely the projected density, is

measured using this technique [40, 41]. Measurements of the time-resolved projected density of

the fuel sprays were conducted at the 7-BM beamline of the Advanced Photon Source [10, 33].

Each diesel injector was mounted horizontally in a high-pressure spray chamber fitted with a pair

of x-ray transparent windows [10, 9, 34]. The chamber was held at room temperature and

pressurized with nitrogen which was continuously purged the vessel to inhibit droplet accumulation. The radiography experimental conditions match those listed in Table 3.
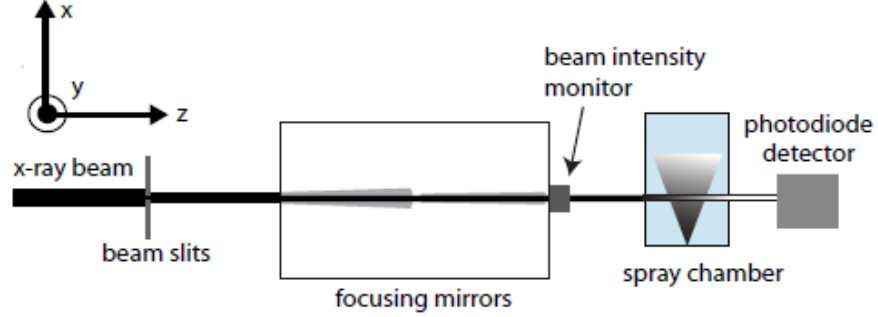
Figure 18: Schematic of the x-ray radiography setup

Figure 18 shows a schematic of the radiography experimental diagnostic. The x-ray source is from the APS at Argonne and the photodiode detects the outgoing x-ray beam intensity [34]. A beam of x-rays from the bending magnet source passed through a double crystal monochromator and beam defining slits to create a monochromatic x-ray beam at 8 keV (4.3% bandwidth) [10, 9, 34]. The x-rays were focused to a 4 μm x 6 μm pencil beam with a pair of x-ray focusing mirrors. The incident radiation, I_o, was measured with an intensity monitor before the x-rays impinged on the spray. The attenuated intensity, I, was captured with a photodiode [10]. At 8 keV x-ray energy, the main interaction of the photons with the fuel spray is through photoelectric absorption. As the beam passes through the spray, photons are absorbed by the fuel. The effective path length, l, can be calculated using the Beer-Lambert law,

$$l = \frac{1}{\mu} \ln\left(\frac{I_o}{I}\right) \tag{4}$$

where μ is the linear attenuation coefficient of the fuel, found through calibration. If the fuel density, ρ, is known, the path length can be converted into the projected fuel density, $\bar{M}$ (units μg/mm^2), through the relation,

$$\bar{M} = \rho l \tag{5}$$

To create the 2D map of the fuel spray distribution, the spray chamber was traversed both horizontally and vertically about a fixed beam, and the x-ray intensity was measured at a raster grid of points. To increase the signal-to-noise ratio, between 16 to 32 spray events were averaged at each spatial location. The radiography measurements were time averaged from 1.3 to 2.3 ms, so the steady portion of the spray is analyzed.

3.3 Scattering Absorption Measurement Ratio Theory

The scattering absorption measurement ratio technique has been presented in previous works by Magnotti and Martinez [7, 10, 9, 8]. The theoretical basis for the measurement ratio was derived by Magnotti and Genzale and is available in Magnotti's thesis [7]. A condensed derivation will be demonstrated here. The full theoretical derivation is available in Appendix A. An expression was derived that relates the optical thickness to the droplet size and liquid volume fraction when applying Mie's solution to Maxwell's equation [42]. The optical thickness can be related to the spray parameters: extinction cross section, liquid volume fraction, and illumination path-length.

$$\tau = \frac{\overline{C_{ext}}}{\frac{\pi d^3}{6}} * LVF * z \tag{6}$$

For Mie scattering (single and independent scattering), it is known that the extinction cross section is proportional to the cross-sectional area of the droplets [42]. The optical thickness from the DBI experiments (equation 1) can be related to this new expression for optical thickness (equation 6) in the single and independent scattering regime. In optically thin regions of the spray (τ<2), single scattering can be assumed. The projected density, measured from the x-ray radiography measurement, can be recast as liquid volume fraction for non-vaporizing and constant liquid density conditions.

$$\frac{\overline{M}}{\rho_f} = LVF * z \tag{7}$$

Because both quantities measured from the experiments are functions of liquid volume fraction, taking a ratio of these quantities will yield a relationship to the droplet size. One necessary assumption in this analysis is comparing equivalent measurement volumes. This assumption will be expanded in 3.4 Data Processing Steps.

$$\frac{\frac{\overline{M}}{\rho_f}}{\tau} = \frac{LVF * z}{\overline{C_{ext}} * \frac{LVF}{\frac{\pi d^3}{6}} * z} \tag{8}$$

Simplifying this expression yields a relationship between our measured quantities (τ and $\overline{M}$) and the mean droplet size within a probed volume or the SMD.

$$\frac{\frac{\overline{M}}{\rho_f}}{\tau} = \frac{\frac{\overline{\pi d^3}}{6}}{\overline{C_{ext}}} \alpha \frac{\overline{d^3}}{\overline{d^2}} = SMD \tag{9}$$

All these terms in the measurement ratio are known, except the extinction (or scattering) cross section. MiePlot, a commercially available program, was used to calculate the extinction cross section for an infinitesimally small collection angle [43]. This quantity is proportional to the overall light lost through the scattering process, and here is determined for monodisperse droplet distributions of varying SMD. The inputs to MiePlot are: log normal distribution of droplet sizes, illumination wavelength of the light source, and index of refraction of the fuel droplets in air. It is well known, however, that extinction experiments use a finite collection angle. Therefore, the additional light collected from forward scattering of a finite collection angle extinction setup must be considered. A MATLAB processing code was used to calculate $\overline{C_{ext}}$ for a given collection angle. As the finite collection angle increases, the forwarded scattered light increases, and the extinction cross section decreases. The measurement ratio is equated to

the SMD by normalizing the calculated $\overline{C_{ext}}$ by the number-weighted mean droplet volume $\frac{\overline{\pi d^3}}{6}$

[7, 9]. Assuming solutions in the Mie-scattering regime, where droplets are larger than the

incident wavelength of light, the calculated ratio is used as a look-up table to relate the

measurement ratio with SMD. Figure 20 shows the measurement ratio as a function of droplet

size.

a)   b)
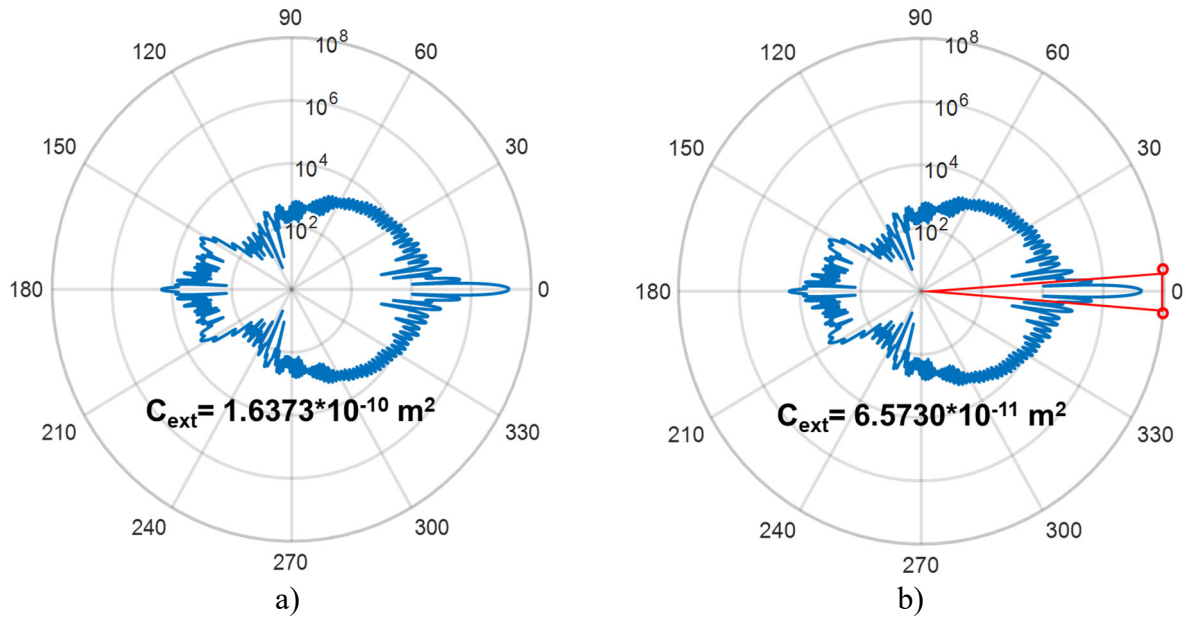
Figure 19: A polar plot generated from MiePlot for a 10μm droplet with a 700nm light source for a) an infinitesimal collection angle and b) a 4.85° half collection angle
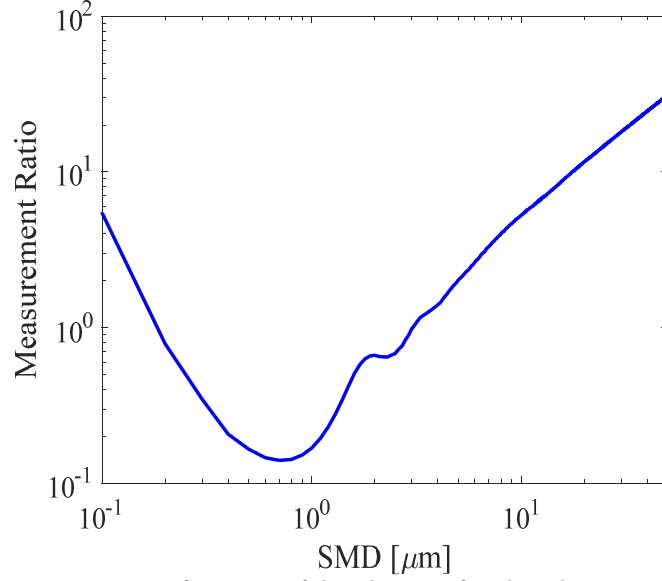
Figure 20: SAMR measurement ratio as a function of droplet size for the Phase III data with illumination wavelength of 633nm and finite collection angle of 3.67°

As mentioned in the derivation of the SAMR technique, it is only valid in the single and independent scattering regime or in the optically thin regions of the spray. Optically thin regions of the spray are usually confined to $\tau < 1.0$. It has been shown that errors due to multiple scattering are low for moderate optical thickness levels ($1.0 < \tau < 2.0$) when the measurement involves small collection angles and small droplets [28, 44], which are expected conditions for the SAMR measurements. In Phase III, a multiple scattering correction was employed which allows for the measurement ratio to be taken throughout the entirety of the spray, thus removing the requirement that $\tau < 2.0$. This correction will be further elaborated upon in 3.4.2 Correction of Measurement Errors from Multiple Scattering.

3.4 Data Processing Methodology

3.4.1 Co-Alignment of Scattering and Absorption Measurements

Because the measurement ratio requires two sets of data from two distinct experimental facilities, careful thought is required when jointly processing the two data sets. Researchers sought to minimize measurement uncertainties by keeping the experimental setups as consistent as

possible. For example, the ambient densities and injection pressures were closely matched. The injectors were shared between the two laboratories. Commanded injection duration and fuel type was matched between the setups. The time average was taken from 1.3 to 2.3 ms for both data sets. It was also essential to ensure that equivalent measurement volumes and the same region of the spray were being compared for both facilities. Therefore, translational and rotational alignment of the sprays is important for jointly processing the two measurements.

Translational co-alignment of the two data sets was explored. It was studied whether the radial distributions of the data sets should be centered by:

a) Shifting the data sets so that the peak value is aligned with x=0

b) Centering the values equal to half of the peak around x=0 (full width half maximum, FWHM)

A study was conducted to analyze which of these methods was more accurate in confirming that the same area of the spray is being explored from both data sets [9]. Figure 20 shows an example of the projected density data aligned using method a) and method b). It appears that aligning the data via these two methods has a very small effect on the projected density data alone. Figure 21 shows that centering the radial distributions using the peak value is not an appropriate method for co-aligning the sprays from both facilities. The spray widths are different for each data set, so shifting the data sets using the full width half maximum method allows for the same region of the spray to be compared for both facilities.
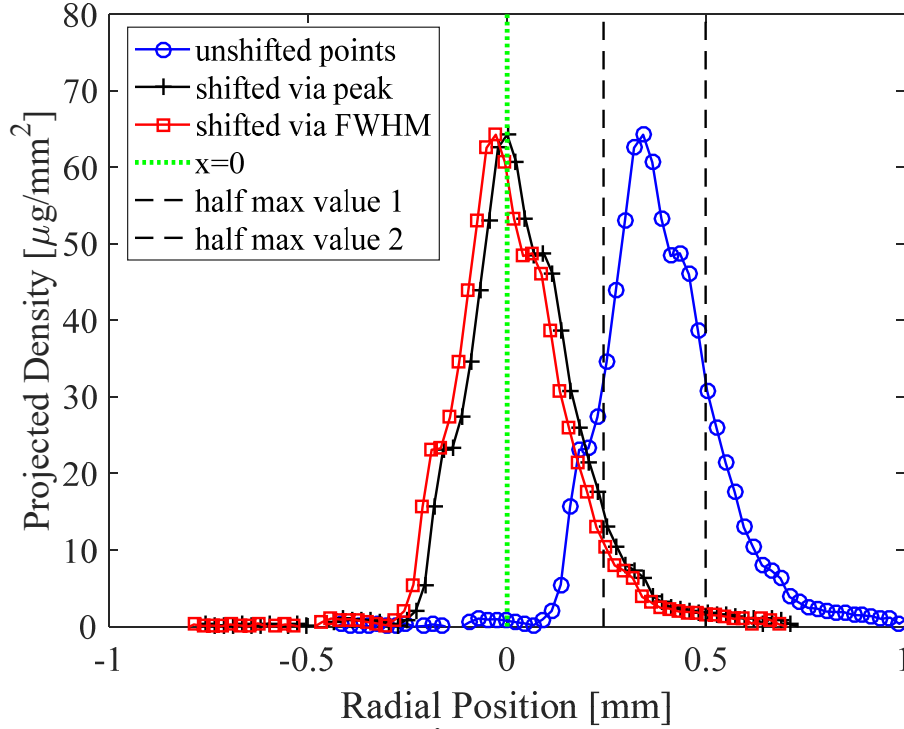
Figure 21: Projected density for Spray D 1.2 kg/m³ 50 MPa at an axial location of 16mm for the unshifted data, the data shifted according to the peak, and the data shifted via full width half maximum
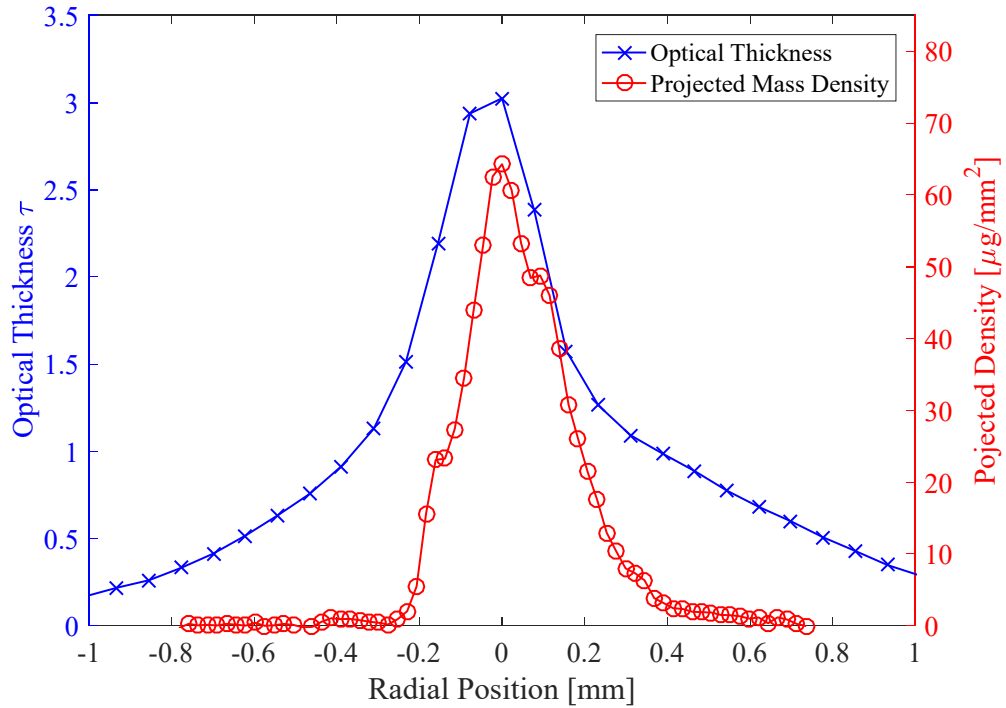
Figure 22: Projected density and optical thickness for Spray D 1.2 kg/m³ 50 MPa at an axial location of 16mm using shifting according to the peak value

Thus, translation co-alignment via full width half maximum is currently the method for ensuring that both data sets are aligned in the projected measurement plane. When aligning via this method, the values (optical thickness or projected density) that are equal to half the maximum are found. The center of the spray is defined as the midpoint between the half-maximum values on each side of the projected density and optical thickness distributions. The SAMR SMD results are determined assuming that these two midpoints correspond to the same location in the spray. Argonne also aligned the projected density data according to this method in a previous publication [45]. Figure 23 and Figure 24 show the unshifted and shifted optical thickness and projected density data sets for Spray D 1.2 kg/m^3 50 MPa at an axial location of 16 mm. Figure 25 shows the properly co-aligned data sets overlaid on one plot.
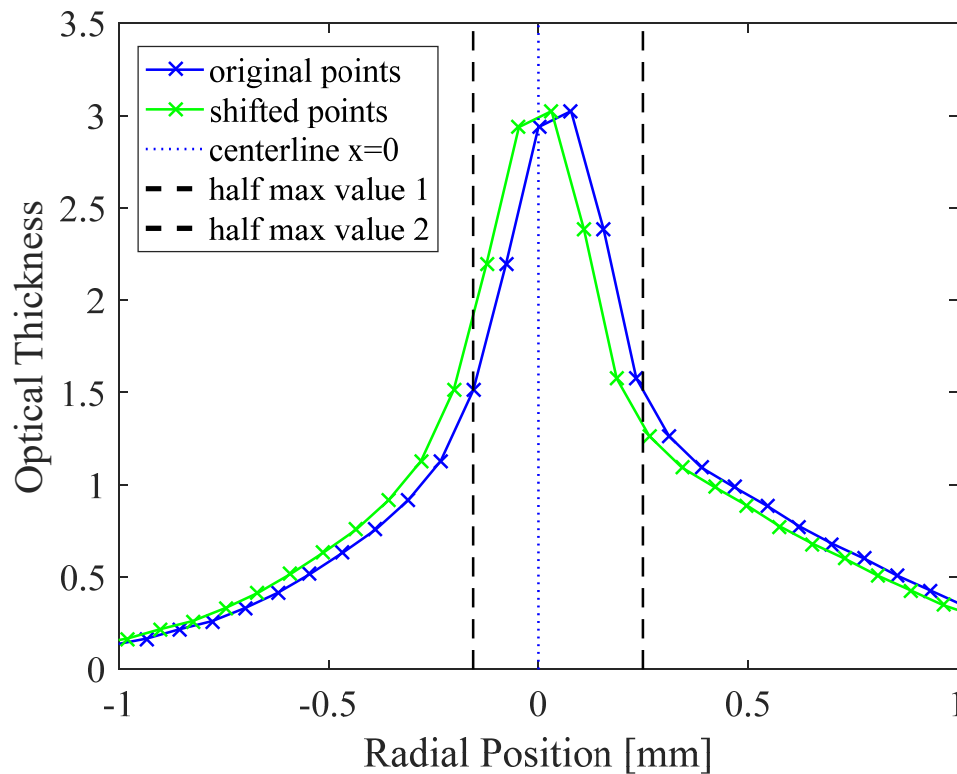
Figure 23: Optical thickness points for Spray D 1.2 kg/m^3 50 MPa at an axial location of 16mm shifting according to the FWHM method

38
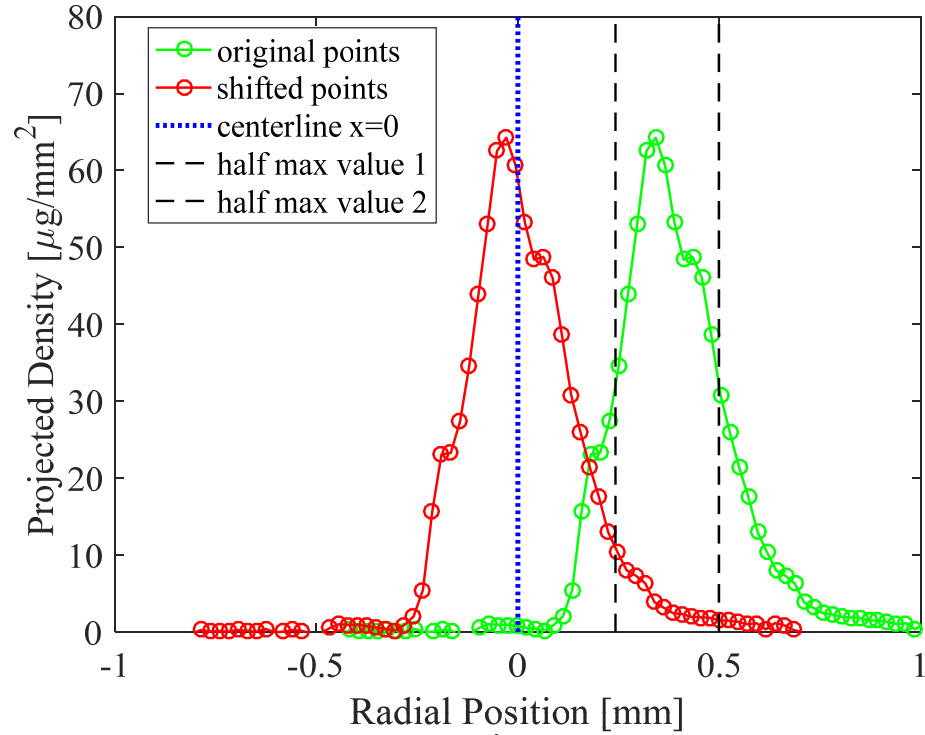
Figure 24: Projected density values for Spray D 1.2 kg/m³ 50 MPa at an axial location of 16mm shifting according to the FWHM method
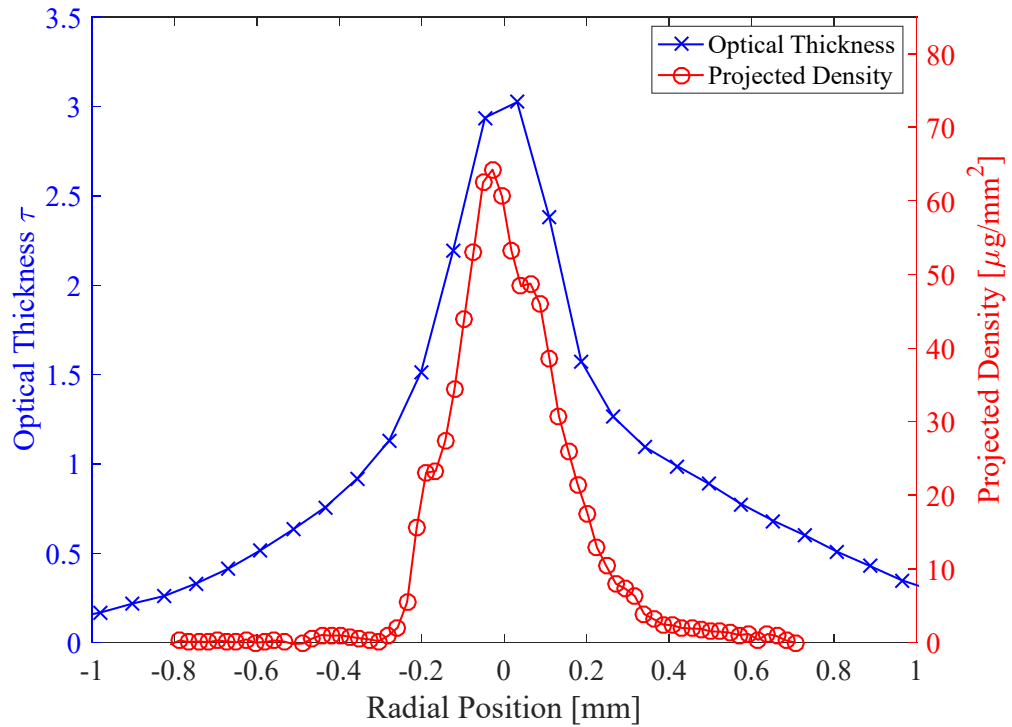
Figure 25: Both data sets overlaid for Spray D 1.2 kg/m³ 50 MPa at an axial location of 16mm shifting according to the FWHM method

In addition to translational co-alignment, the sprays also needed to be rotationally aligned. Previously, asymmetries in the spray were observed, which ultimately will have a large effect on the quantified SMD [9]. These asymmetries in the spray make it essential that the injectors are oriented in the same manner, so that the same region of the spray can be compared. For Phase I of the experimental campaign, the orientation between the two facilities was off by about 10°. For Phase II and III, the injector orientations were matched within approximately 1°. Table 3 shows the aimed injector orientation for each condition. Figure 26 shows the ECN specifications for the 0° orientation.
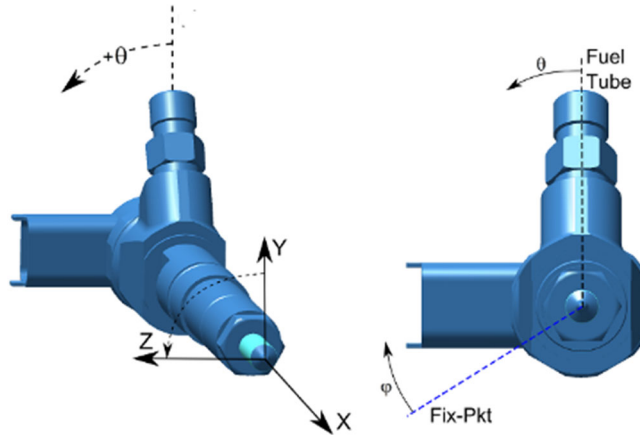
Figure 26: 0° orientation according to the ECN specifications

After the two sprays were co-aligned, a resampling of the project density values occurred. Due to the nature of the radiography measurement, it is possible to achieve finer spatial resolution for the projected density data than the optical thickness data. The resolution of the optical thickness data was limited by the optical setup, namely by the projected pixel size. To ensure that the joint measurement analysis is conducted for equivalent measurement volumes, a resampling process was established. The resampled measurement volumes or bins are equal in size to the spatial resolution of the DBI measurements (see Table 2). Each bin is centered about each optical thickness point. The resampling process is illustrated in Figure 27. The dashed lines show the resampled measurement volumes. The green lines show the two limits for the SAMR

technique. Finally, the purple boxes show the locations where the measurement ratio was taken

for Phase 1.
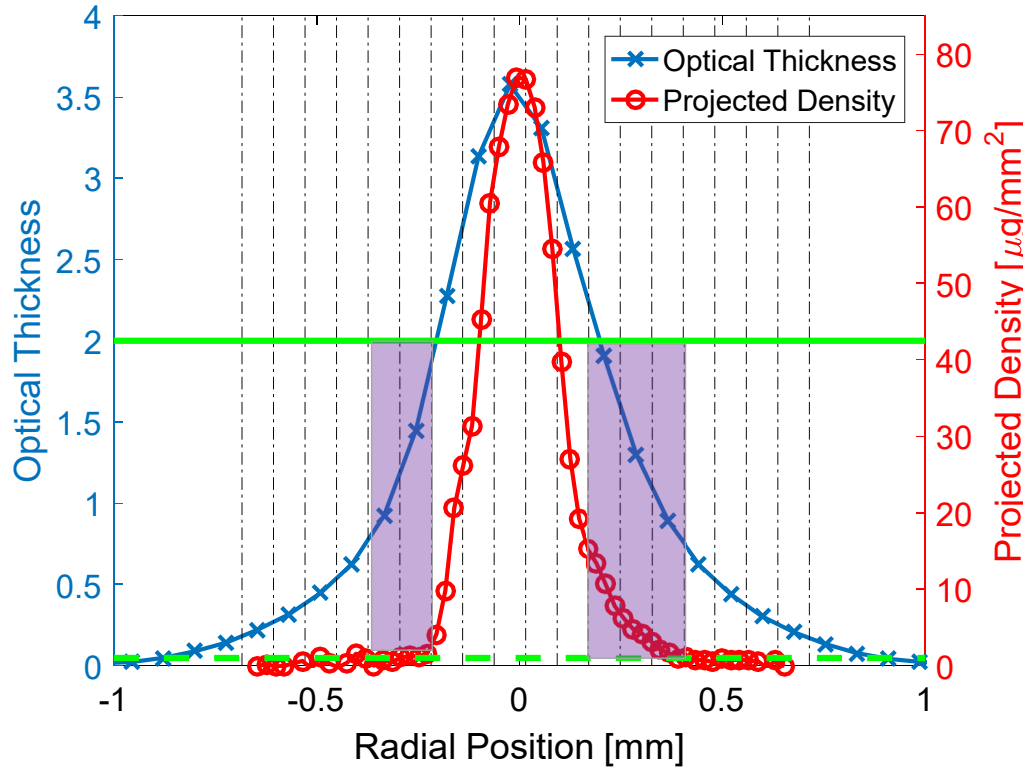
Figure 27: The optical thickness and projected density values for Spray D 2.4 kg/m³ 50 MPa at an axial location of 10 mm

3.4.2 Correction of Measurement Errors from Multiple Scattering

Figure 27 shows another important processing step: identifying the regions where the

SAMR measurement is valid without correction for the impact of multiple-scattering. As

demonstrated in the theoretical development of the SAMR theory, the Mie-scatter calculations

used to quantify SAMR SMDs are limited to single scattering. For Phase I, both conditions were

met. In Figure 27, the purple shaded boxes indicate the regions where a measurement ratio could

be taken. For Phase II and III of the project, a multiple scattering correction was employed which

removed the $\tau < 2.0$ restriction on the utility of the SAMR technique. For these phases, the

measurement ratio was only restricted to satisfying b).

Multiple scattering has a significant impact on a scattering-based measurement with a finite collection angle. To eliminate the restriction of a), the contribution of multiple-scattering must be accounted for. Therefore, the measured optical thickness must be corrected to achieve an accurate SMD estimation using the proposed method. Correcting for the multiple scattering effect will allow for a measurement ratio to be taken everywhere throughout the spray. This will provide a better understanding of the SMD field. To correct for multiple scattering, the modification proposed by Berrocal et al. is first adapted to the current optical system and then used to correct the measured optical thickness [28, 44].

According to Berrocal, the measured optical thickness (τ_{meas}) can be corrected (τ_{corr}) using the following equation which accounts for the influence of multiply scattered light [28]. This relation is for a measurement system with an infinitesimally small collection angle.

$$\tau_{meas} = \tau_{corr} - \alpha \; \tau_{corr}^{\beta} \tag{10}$$

where the coefficients α and β are related to the collection angle of the detection system and size of droplets present in the probe volume. Berrocal et al. reported the values of these coefficients for two collection angles of 3.3° and 10.3° (i.e. recalculated in a manner consistent with the current work) and mono-disperse particle sizes ranging from 1 to 20 μm, illuminated by a 800 nm light source [28, 44]. These constants are linearly interpolated to match the collection angle of the DBI experiments stated in Table 2. The difference in the wavelength of light source is also corrected. According to the theory of light scattering, particles of identical size parameter demonstrate the same scattering behavior [42]. The size parameter x is defined as

$$x = \frac{\pi d}{\lambda} \tag{11}$$

where d is the size of particles and λ is the wavelength of the incident light. Equation 12 is used

to find the size of droplets exhibiting similar scattering behavior at 633 nm to those reported in

the literature, d_{Lit}, illuminated at 800 nm [28, 44]

$$d_{633} = \frac{633}{800} \, d_{Lit} \tag{12}$$

Table 5 shows the diameters reported in the literature and those calculated to relate the 633 nm

light source from the DBI experiments to the 800 nm light source used in the literature.

Table 5: Droplet sizes in literature converted to droplet sizes for 633 nm light source

d_{lit}	d_{633}
1 μm	.79 μm
5 μm	3.9 μm
10 μm	7.9 μm

Equations 10 and 12 are then used to construct a transfer function which corrected the measured

optical thickness using the current system, as seen in Figure 28. The measured optical thickness

and local droplet size both must be known to do this. While the former is directly measured

through the experiments, the latter is initially an unknown parameter. Therefore, an iterative

process is required to solve equation 10. The transfer function is coupled to equation 10 and

solved iteratively to compute the actual optical thickness of the spray field and the corresponding

SMD [10].
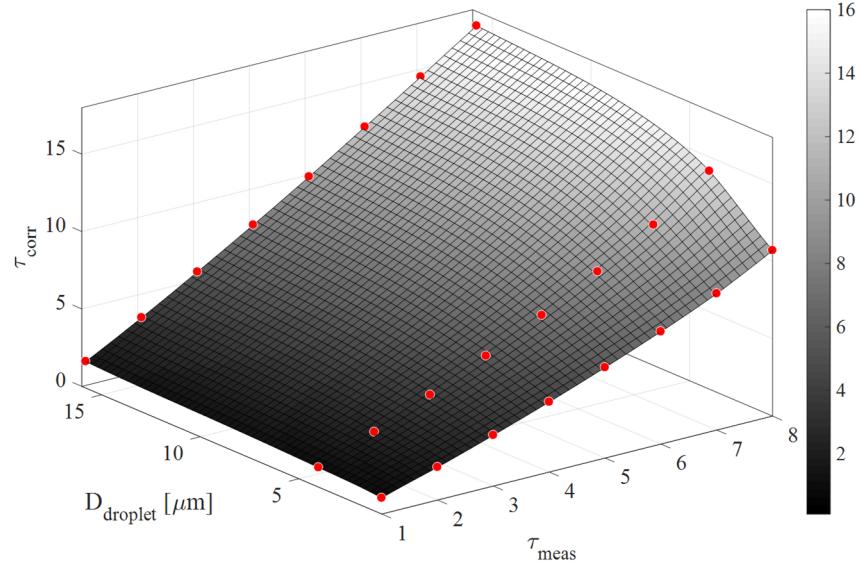
Figure 28: Graphical representation of the transfer function to correct the measured optical thickness as a function of the local droplet size.

Figure 29 illustrates the contribution of multiple scattering on the measured optical thickness for the Spray A 22.8 kg/m^3 and 50 MPa 10 mm away from the nozzle exit. Multiple scattering has a significant impact on the DBI measurement at the spray centerline where the optical thickness is the highest [10]. It becomes less severe and eventually negligible towards the periphery of the spray, where the corresponding optical thickness approaches zero. This trend is expected largely due to the dominance of low-order scattering events in this region [10]. The multiple scattering correction was employed in the regions where this phenomenon may be of considerable impact (i.e. $\tau > 1$) for Phase II and III of this work.
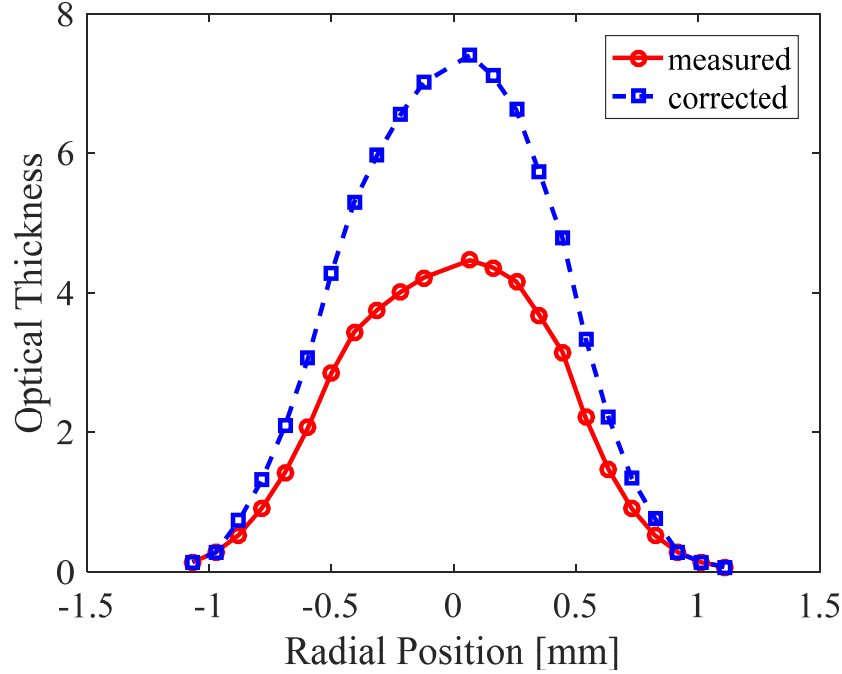
Figure 29: Measured and corrected optical thickness for Spray A 22.8 kg/m3 50 MPa at an axial location of 10 mm

3.4.3 Data Smoothing

After identifying the regions where a measurement ratio could be conducted, the projected density values were curve fit. Curve fitting reduces the inherent noise present in experimental measurements and smooths the data. The curve fits were used to quantify the average projected density in each bin. The curve fitting technique varied for each data set. For the low back pressure cases, asymmetries are present in the spray. Therefore, it was necessary to employ separate curve fits for each condition. Some axial locations had features that could not be easily curve fit, such as the "shoulder" seen in the projected density data on the left-hand side of the spray as seen in Figure 30a. These asymmetries are seen at multiple axial locations for the 1.2 kg/m^3 ambient density condition and are therefore, not likely to be artifacts of noise. To capture these aspects of the spray, each axial location was individually curve fit. The curve fits had an R^2 value greater than 0.98. The curve fits accurately represented the trends in the data.

Figure 30a and b show the curve fits for the left and right half of the projected density distributions at the 10, 16 and 20 mm axial locations, respectively. For the left half of the spray (Figure 30a) for the 10 and 16 mm axial locations, two separate curve fits are used to capture the complex shape of the data, namely the "shoulder" in the projected density data. The data is broken up into two segments surrounding the "shoulder." The first segment was fit with an exponential function of the form,

$$f(x) = Ae^{Bx} + Ce^{Dx} \tag{13}$$

where A, B, C, and D are unique fitting coefficients. For the 10mm axial location, the second segment of data points was fit with a three term polynomial function of the form,

$$f(x) = Fx^3 + Gx^2 + Hx + I \tag{14}$$

where F, G, H, and I are unique fitting coefficients. For the 16mm axial location, the second segment of data points was fit with an exponential function of the form,

$$f(x) = Je^{Kx} + Le^{Mx} \tag{15}$$

Where J, K, L, and M are unique fitting coefficients. The 20mm location was curve fit using a single Gaussian function,

$$f(x) = Ne^{-(\frac{x-P}{Q})^2} \tag{16}$$

For the right half of the spray (Figure 30b), the radial distribution was more uniform and could be easily fit with an exponential curve fit of the form of equation 16. For phase I of the project, only the wings of the spray needed to be curve fit because these were the viable measurement regions. For phase II and III, the entirety of the spray was curve fit.
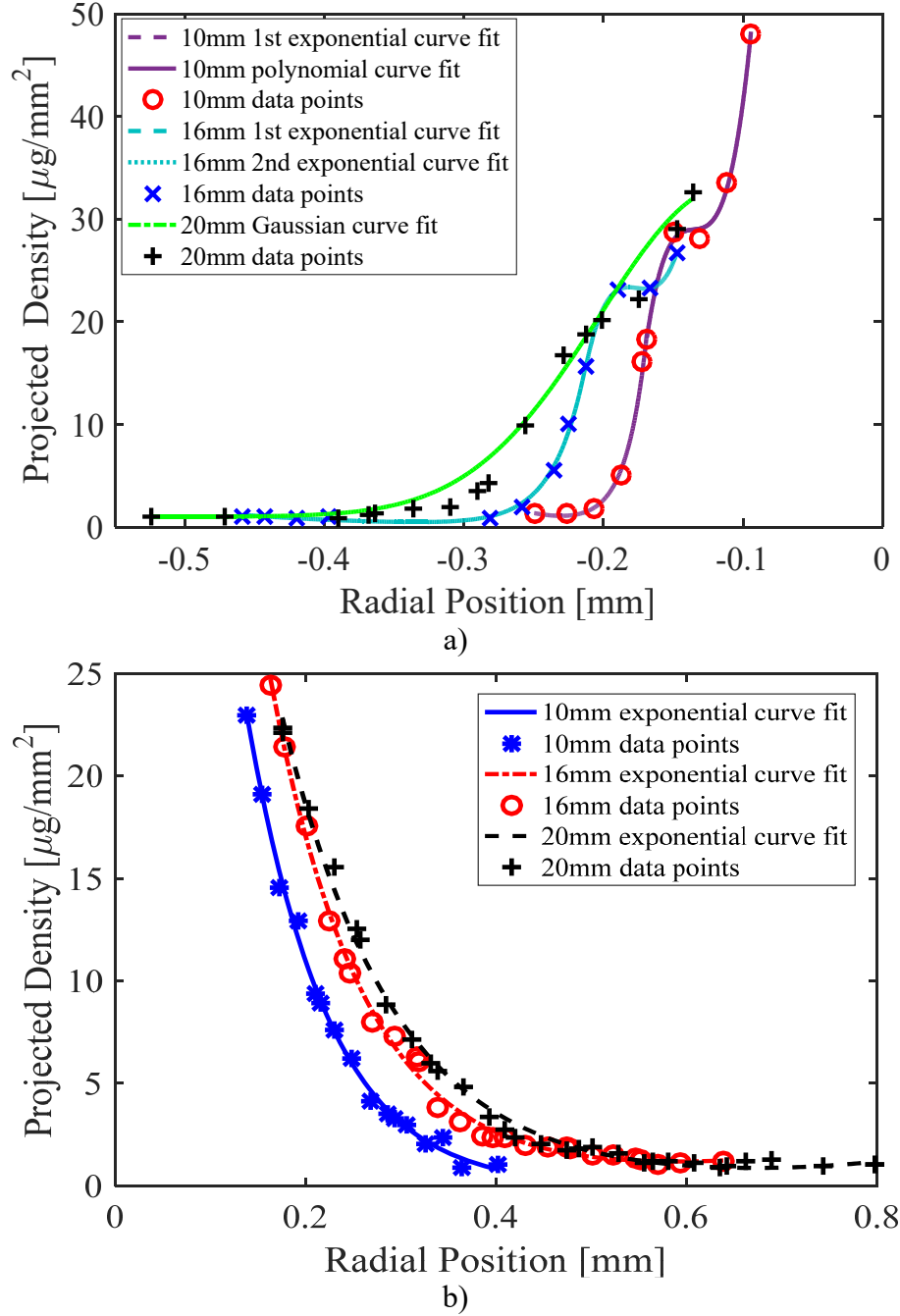
Figure 30: Projected density measurements and their respective curve fits for Spray D 1.2 kg/m3 50MPa three axial locations (10 mm, 16 mm, and 20 mm) for the left half (a) and right half (b) of the spray

For higher back pressure cases, a Gaussian or double Gaussian curve fit was sufficient to accurately follow the trends and to smooth the data. In Phase III, the projected density from the 90, 120 and 150° viewing angles, show asymmetries that required careful curve fitting. A new curve fitting method was used to accurately capture the behavior of the data along the wings of

the spray and near the spray centerline. A moving average was used to curve fit the radiography

data along the wings and a Gaussian curve fit was used to curve fit the centerline data.
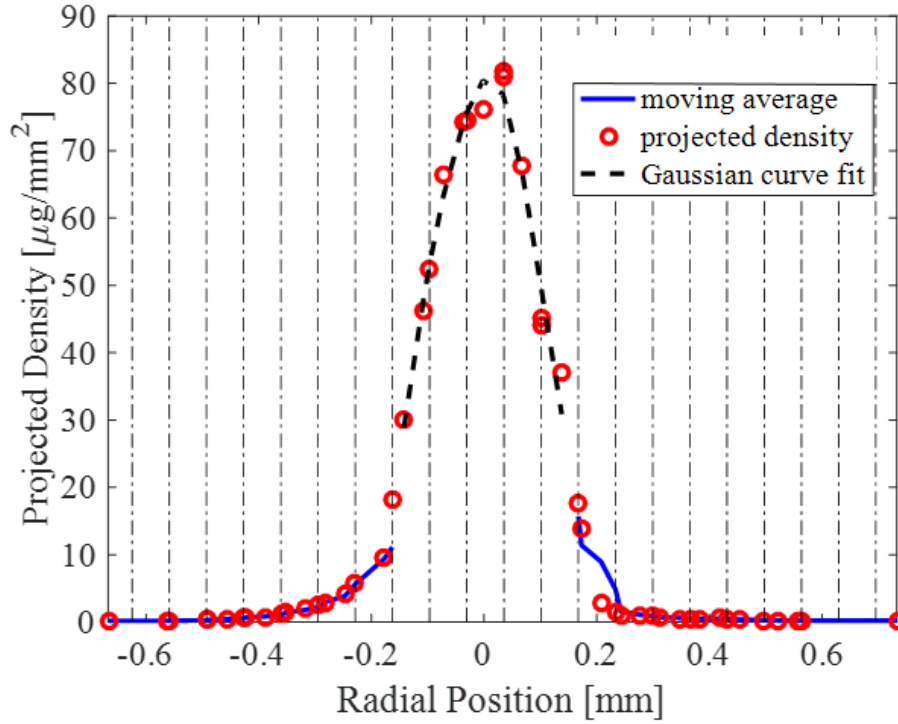
Figure 31: Curve fit of projected density values using a moving average along the wings and a Gaussian curve fit at the centerline for Spray D 1.2kg/m3 50MPa at 10 mm for 90° orientation

Once a curve fit has been applied, the average under the curve for the projected density is

calculated. After the average projected density value is calculated and overlaid with the optical

thickness points (see Figure 31), a ratio is taken between the average projected density value

divided by the fuel density and the optical thickness value (see equation 8). This measurement

ratio is then related to C_{ext} from MiePlot as discussed previously and the SMD can be calculated.

The SMD results and measurement uncertainty analysis will be presented in Chapter 4.
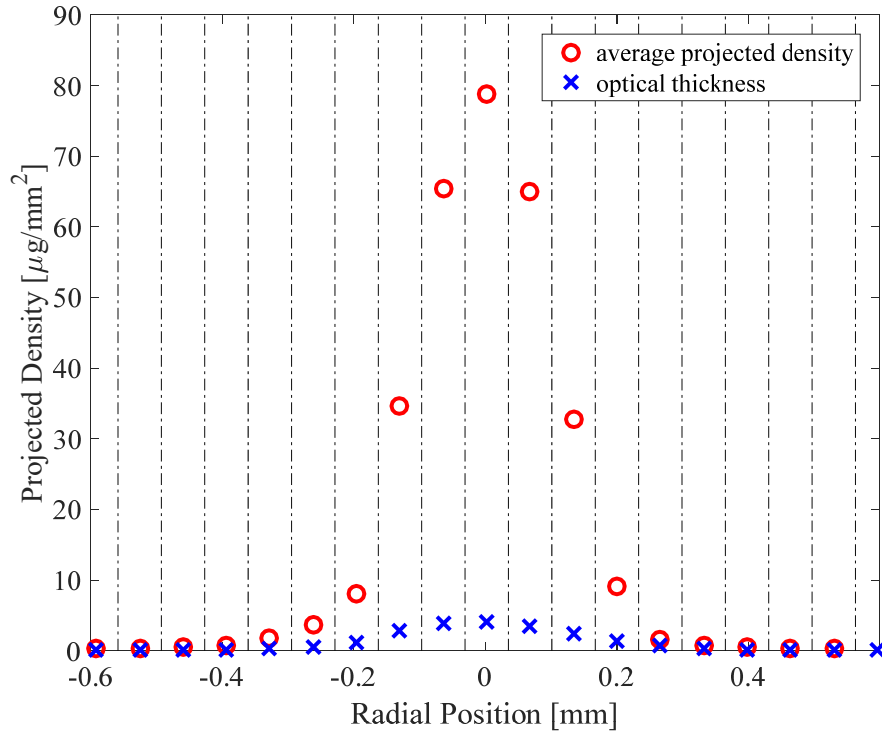
*Figure 32: Average projected density values and optical thickness values for Phase III Spray D 1.2 kg/m³
50 MPa at 10 mm for 90° orientation*

CHAPTER 4

RESULTS

Each phase of this work provided interesting spray droplet sizing information. This chapter will be segmented into three sections corresponding to each phase of the work.

4.1 Phase I SMD results

As stated earlier, the goal of Phase I was to demonstrate an extended proof of concept of the diagnostic based on DBI scattering extinction measurements and to establish the appropriate data processing methodology. Besides this, Phase I also provided useful SMD information. Figure 33-39 show radial distribution plots of SMD for multiple experimental conditions using the Scattering Absorption Measurement Ratio technique for Phase I data set. The USAXS SMD results are overlaid on Figure 34-39 to validate the SAMR measurements.

Figure 33 indicates that a dense region of larger sized droplets exists closer to the spray centerline, with smaller sized droplets along the spray periphery. The right half of the spray also shows that the 16 mm and 20 mm axial locations have droplets similar in size. This suggests that a quasi-stable droplet size has been reached at these downstream locations. Also, the data demonstrates that there are asymmetries in the spray. As seen in Figure 33, the SMD measurements for the right half of the spray show a more gradual decrease in droplet size with increasing distance from the spray centerline than for the left half of the spray. The asymmetry of the radial distribution is likely to be strongly affected by the orientation of the diffuse-back illumination and x-ray radiography measurements. The asymmetry observed in the spray SMD distributions indicate that the assumption of a symmetric spray is not always valid, especially at

this low backpressure conditions (1 bar). Figure 33 shows that asymmetries are evident in both the DBI and radiography measurement results, particularly evident in the "shoulder" seen in the left side of the projected density data. These spray features may stem from the machining groove that is present along the interior of the Spray D #209133 orifice [46].
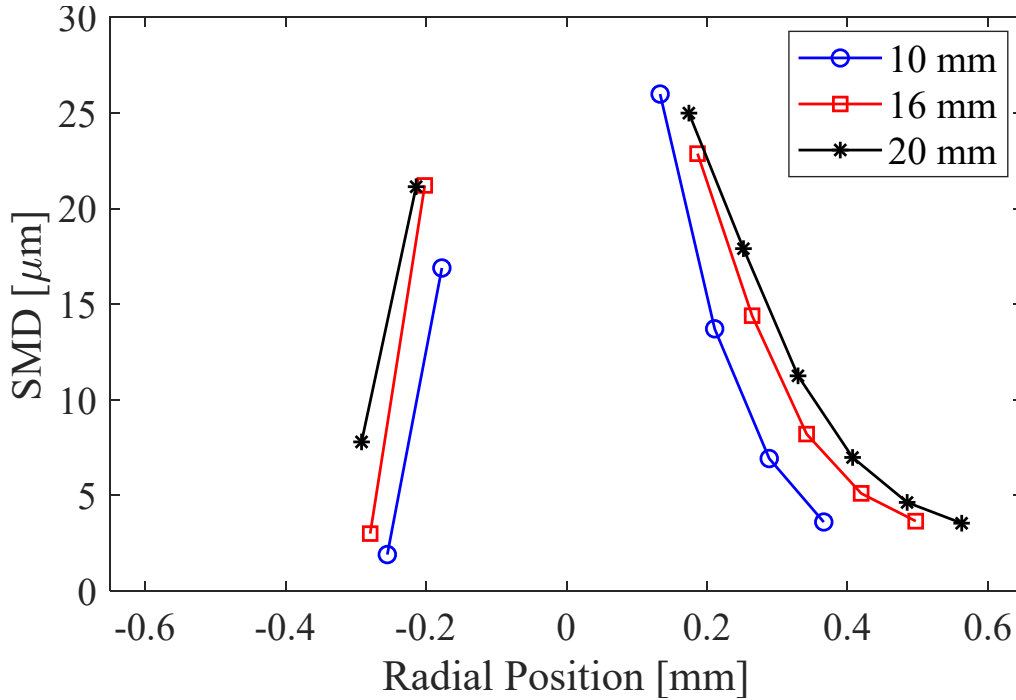
Figure 33: Phase I SAMR SMD results for Spray D 1.2 kg/m³ 500 bar at axial locations of 10, 16, 20 mm

Figure 34 and 35 show the phase I SAMR SMD results overlaid with the USAXS results from the campaign Cycle2016_2 for the Spray D injector at an ambient density of 1.2 kg/m³ and injection pressures of 500 bar and 1500 bar, respectively. These figures show similar trends as before. Larger droplets exist closer to the spray centerline. Moving away from the spray centerline produces droplets smaller in size. The Phase I results do not show droplet sizes at the spray centerline because the multiple scattering correction had not yet been employed. For this data campaign, the SAMR measurement produces larger droplets than the USAXS measurement. The USAXS transverse results for Cycle2016_2 were obtained while measuring the centerline

information, and some uncertainty in the USAXS transverse measurements exist. Argonne

improved the USAXS measurement in the Cycle2017_3 campaign.

Figure 34: Phase I SAMR SMD results compared with the USAXS results (Cycle2016_2) for Spray D 1.2 kg/m³ 500 bar at an axial location of 10 mm

Figure 35: Phase I SAMR SMD results compared with the USAXS results (Cycle2016_2) for Spray D 1.2kg/m³ 1500 bar at an axial location of 10 mm

Table 6: Percent Difference between SAMR (Phase I) and USAXS (Cycle2016_2) for Spray D 1.2 kg/m³ 500 bar for an axial location of 10 mm

SAMR		USAXS		% Difference in SMD	% Difference in location
Radial Position (mm)	SMD (μm)	Radial Position (mm)	SMD (μm)		
0.13	26.0	0.18	6.6	119%	29%
0.21	13.7	0.20	5.5	85%	6%
0.29	6.9	0.25	3.0	78%	14%

Table 6 shows the percent difference in droplet size and location between the SMD results presented in Figure 34 for the USAXS and SAMR diagnostics. Near the spray center line, the difference in droplet size between USAXS and SAMR is about 19 μm. One reason for the large difference in droplet size could be that at these locations close to the center line, the optical thickness value approaches the threshold of $\tau = 2$ and thus the DBI measurement could be susceptible to errors associated with multiple scattering. As the radial distance from the centerline increases, the difference between the SAMR and USAXS SMDs decrease. At the furthest positive position, the difference in droplet size is only 3.8 μm. From Figure 34 and 35, it appears that there is some misalignment between the USAXS and SAMR results. It looks like the data may be shifted radially from each other, suggesting that the data are not truly co-aligned. Another source of uncertainty with this USAXS campaign is improper alignment of the surface area and the radiography measurements. When the USAXS transverse scan is performed, the beam is centered at the peak value of maximum signal intensity, which should theoretically align with the spray centerline [34]. Unfortunately, this cannot be confirmed since Argonne researchers are unable to take the radiography and USAXS measurement simultaneously.

To reduce the measurement uncertainty in the USAXS data, researchers at Argonne completed another campaign which focused on the radial distributions of SMD and proper alignment of both measurements in Cycle2017_3. Figure 36-39 show the comparison of SMD results for the SAMR and Cycle2017_3 USAXS techniques. These updated USAXS results and

SAMR results show good agreement in droplet size. Some uncertainty remains in proper co-alignment between the SAMR and USAXS methods. Currently, the USAXS data is shifted via FWHM prior to overlaying it with the SAMR results. The right half of the spray (positive half) is mostly presented here because more viable data locations for the SAMR were present at these regions. Figure 36 shows larger sized droplets near the spray centerline. The droplets decrease in size as the radial position is increased. The SMDs show decent agreement with the maximum difference in droplet size being about 3.9 µm.
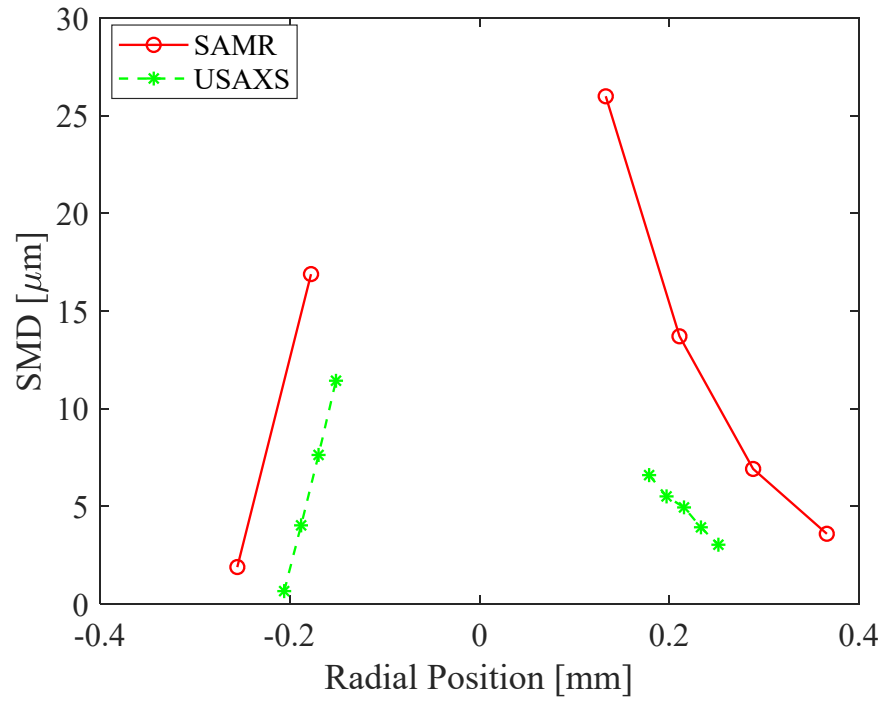

Figure 36: Phase I SAMR SMD results compared with the USAXS results (Cycle2017_3) for Spray D 1.2 kg/m³ 500 bar for an axial location of 10 mm

Table 7: Percent Difference between SAMR (Phase I) and USAXS (Cycle2017_3) for condition presented in Figure 36

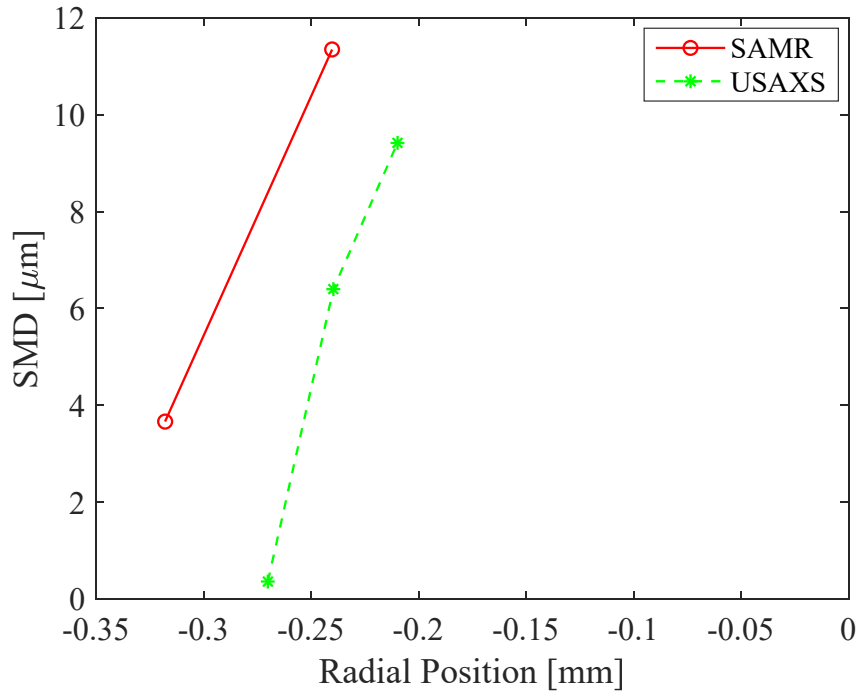| SAMR		USAXS		% Difference in SMD	% Difference in location
Radial Position (mm)	SMD (µm)	Radial Position (mm)	SMD (µm)		
0.13	26.0	0.05	24.0	8%	89%
0.21	13.7	0.18	9.8	33%	16%
0.29	6.9	0.24	5.2	28%	17%
0.37	3.6	0.31	2.8	25%	18%
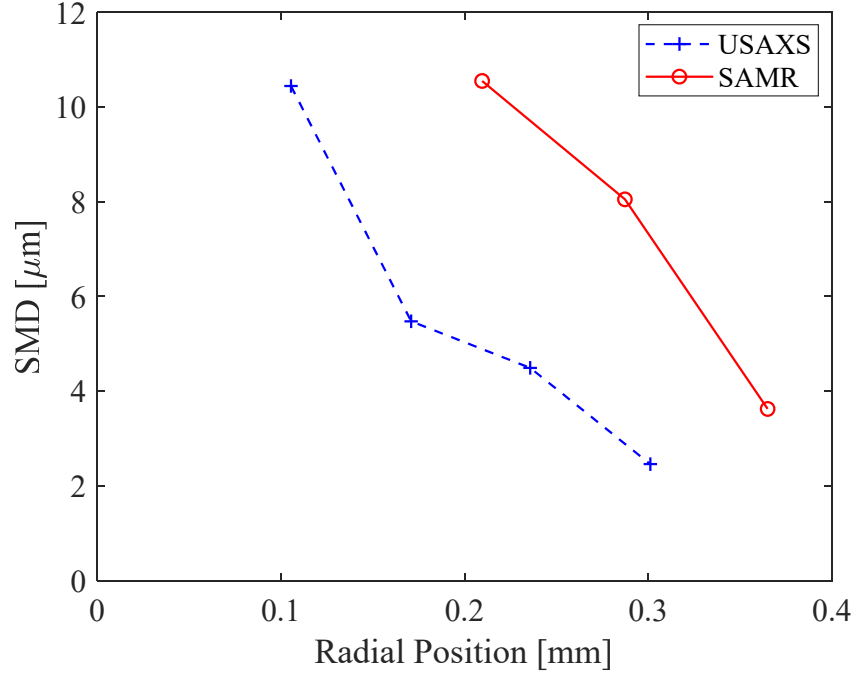
Figure 37: Phase I SAMR SMD results compared with the USAXS results (Cycle2017_3) for Spray D 2.4 kg/m³ 500 bar for an axial location of 10 mm

Table 8: Percent difference between SAMR (Phase I) and USAXS (Cycle2017_3) for condition presented in Figure 37

SAMR		USAXS		% Difference in SMD	% Difference in location
Radial Position (mm)	SMD (μm)	Radial Position (mm)	SMD (μm)		
0.21	10.6	0.11	10.4	1%	66%
0.29	8.1	0.17	5.5	38%	51%
0.36	3.6	0.30	2.5	38%	19%

Table 9: Percent difference between SAMR (Phase I) and USAXS (Cycle2017_3) for condition presented in Figure 38

SAMR		USAXS		% Difference in SMD	% Difference in location
Radial Position (mm)	SMD (μm)	Radial Position (mm)	SMD (μm)		
0.32	6.8	0.14	7.3	7%	77%
0.40	5.4	0.19	4.0	29%	69%
0.48	4.6	0.29	3.2	38%	46%
0.55	3.7	0.35	2.1	53%	45%

55
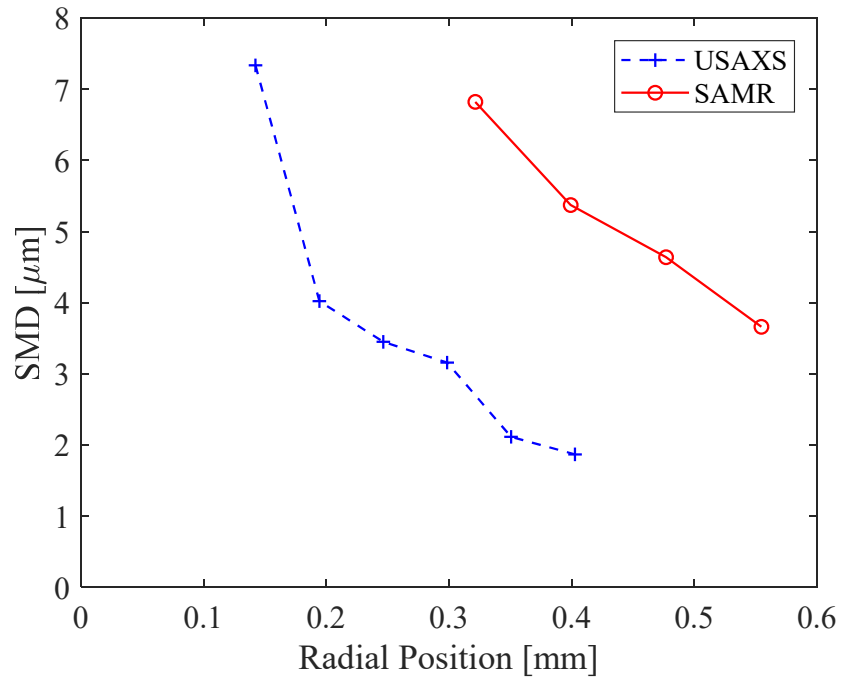
Figure 38: Phase I SAMR SMD results compared with the USAXS results (Cycle2017_3) for Spray D 2.4 kg/m³ 500 bar for an axial location of 15 mm
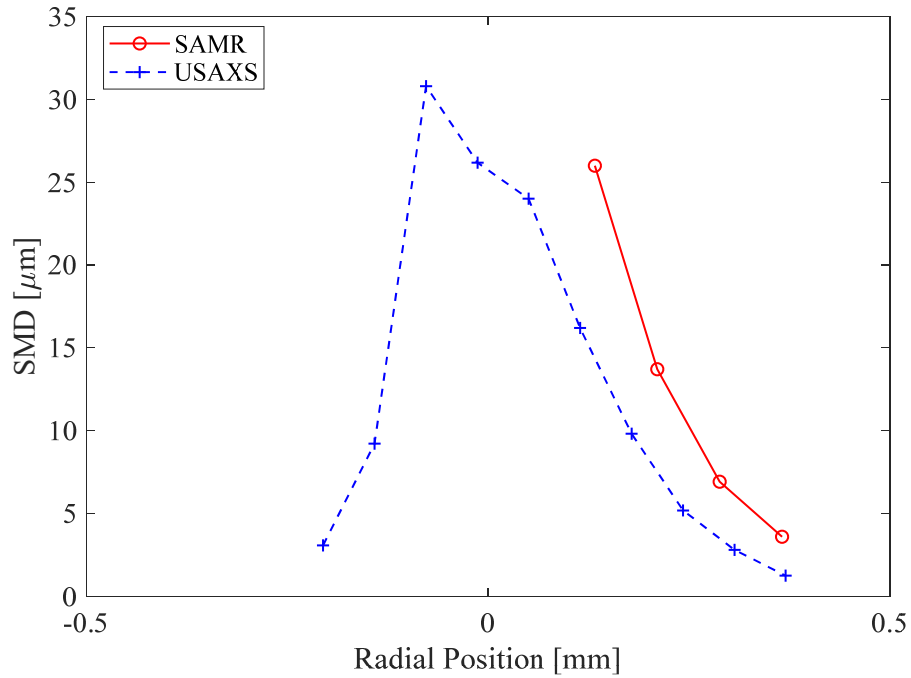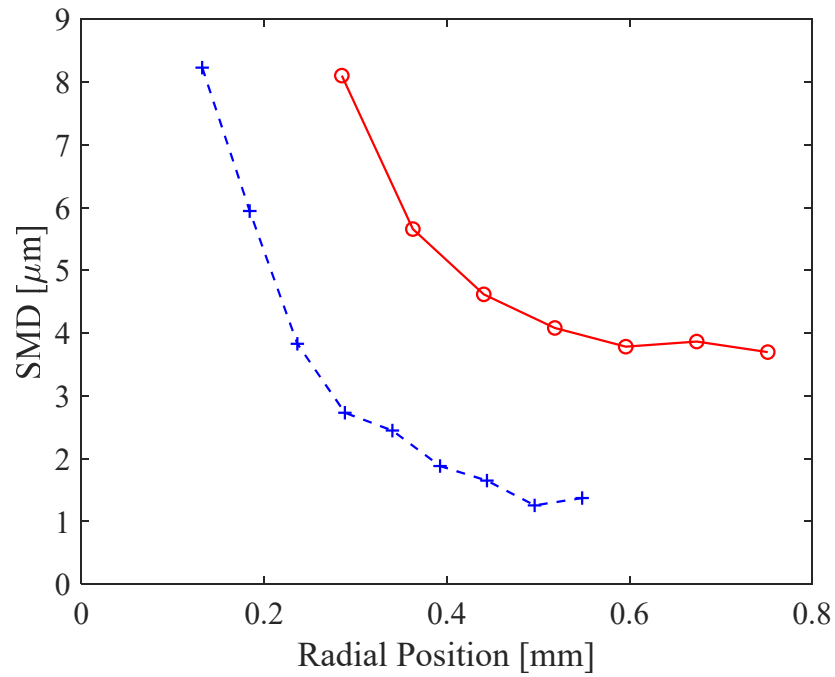

Figure 39: Phase I SAMR SMD results compared with the USAXS results (Cycle2017_3) for Spray D 2.4 kg/m³ 500 bar for an axial location of 20 mm

Table 10: Percent difference between SAMR (Phase I) and USAXS (Cycle2017_3) for condition presented in Figure 39

SAMR		USAXS		% Difference in SMD	% Difference in location
Radial Position (mm)	SMD (μm)	Radial Position (mm)	SMD (μm)		
0.28	8.1	0.13	8.2	2%	73%
0.36	5.6	0.18	5.9	5%	65%
0.44	4.6	0.23	3.8	19%	60%
0.52	4.1	0.34	2.5	50%	41%
0.59	3.8	0.39	1.9	67%	41%
0.67	3.9	0.44	1.6	80%	41%
0.75	3.7	0.55	1.4	31%	92%

Figure 37-39 show similar trends as before, decreasing droplet size as radial position increases. Table 8-9 show the radial locations, SMD values, and corresponding percent differences for SAMR and USAXS measurements. While radial distributions of SMD at distinct axial positions are useful, two-dimensional color maps with interpolation provide a more complete picture of the spatial droplet evolution. These SMD maps are shown in Figure 40.
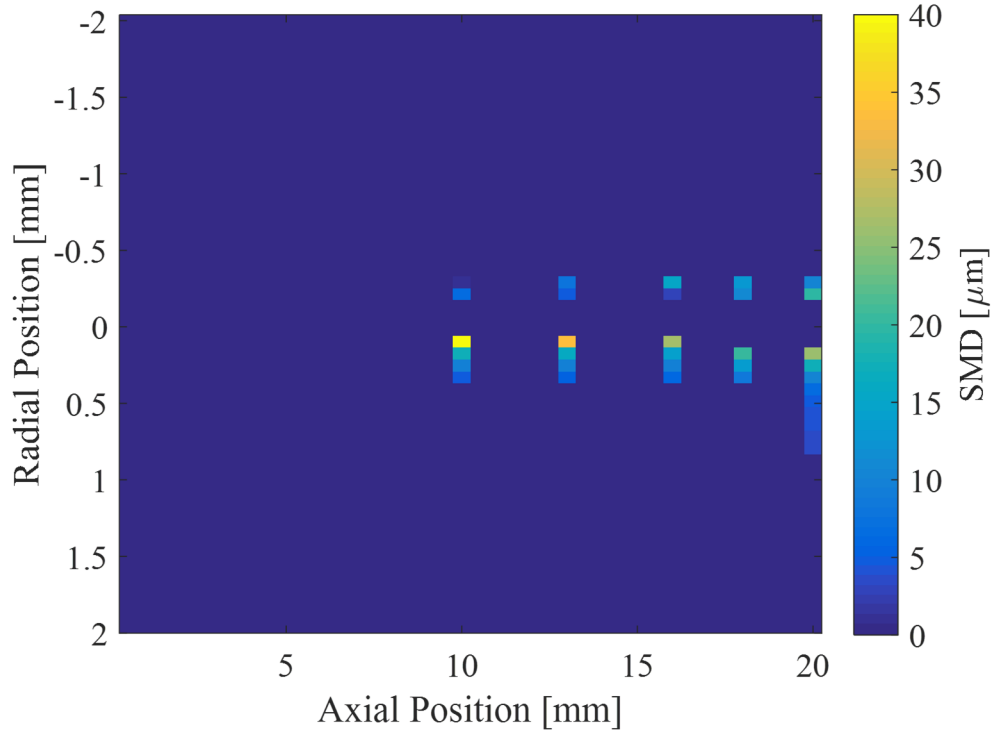
Figure 40: Phase I SMDs for Spray D 1.2kg/m³ 50MPa with interpolated points at 13 and 18 mm
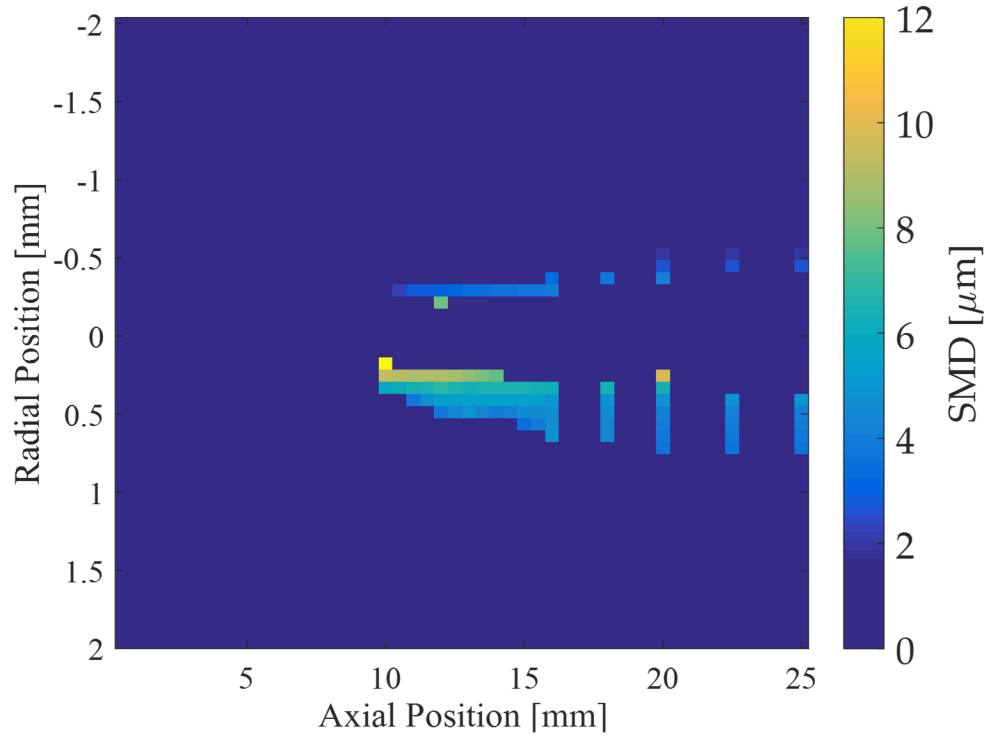
Figure 41: Phase I SMDs for Spray D 2.4 kg/m³ 50 MPa with interpolated points at 10.5, 11.5, 12.5, 13.5, 14.5, 15.5, 18, 22.5 mm
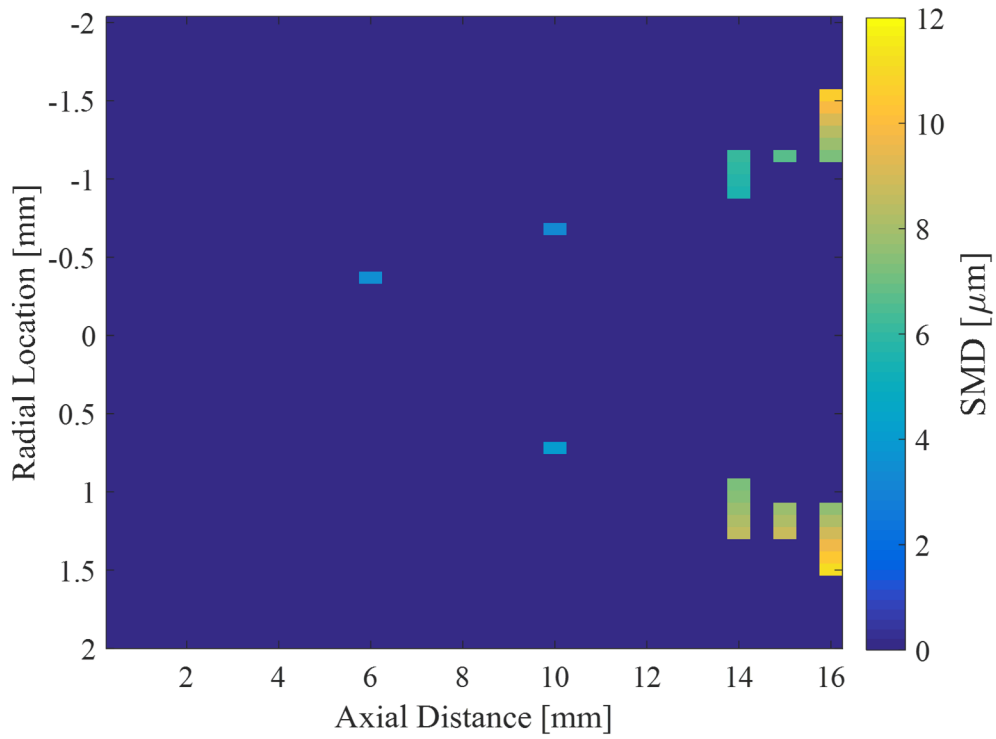
Figure 42: Phase I SMDs for Spray D 22.8kg/m³ 50MPa with interpolated points at 15 mm

Figure 40 and 41 show similar trends, larger droplets exist closer to the spray centerline, whereas smaller droplets occur along the spray periphery. Increasing axial distance from the nozzle exit results in smaller droplets. This trend is evident for the low ambient density cases (1.2 and 2.8 kg/m^3). As ambient density increases, this trend is not observed. For the 22.8 kg/m^3 ambient density case, at downstream axial locations, droplets increase in size as radial position increases, as seen in Figure 42. This counterintuitive trend has been observed by other researchers [5, 27, 47, 48, 49]. This increase in SMD at the spray periphery is primarily attributed to two potential mechanisms: droplet collision/coalescence at the peripheral region due to shear effects [48], and transport of large droplets from the core region due to vortex effects at the spray tip [49].

4.2 Data Processing Uncertainty Analysis

The Phase I SMD results provide a quantitative data set for model validation with more spatial resolution than any other diesel drop sizing data set to date, other than perhaps the work of Parker and Labs [5, 23]. To be useful to modelers, the measurement uncertainties associated with this new diagnostic were assessed. An uncertainty analysis was conducted which evaluated the relative effect each processing step had on the quantified SMD. The first processing step that was analyzed was the co-alignment of the scattering extinction and x-ray radiography absorption matching data sets. Because the data were taken at two experimental facilities, co-alignment was essential to ensure that the same region of the spray was being analyzed. Additionally, each facility uses a different coordinate system for the measurements, thus emphasizing the need for spatial co-alignment. This analysis was conducted to determine the sensitivity of the SMD measurement to the translational co-alignment. The DBI and radiography data sets were translated and centered with respect to each other according to FWHM. Next, the projected

density values were shifted radially by distances of ±0.05 and ±0.15 mm. The optical thickness

values and the locations of the bins were not changed. The projected density values in each bin

do change, which results in a different average projected density value. This new average

projected density value is used to calculate a new measurement ratio in that bin, and ultimately, a

different SMD. Figure 43 shows the shifting that occurred for the projected density values for

Spray D 2.4 kg/m^3 and 50 MPa at 14 mm axial location.
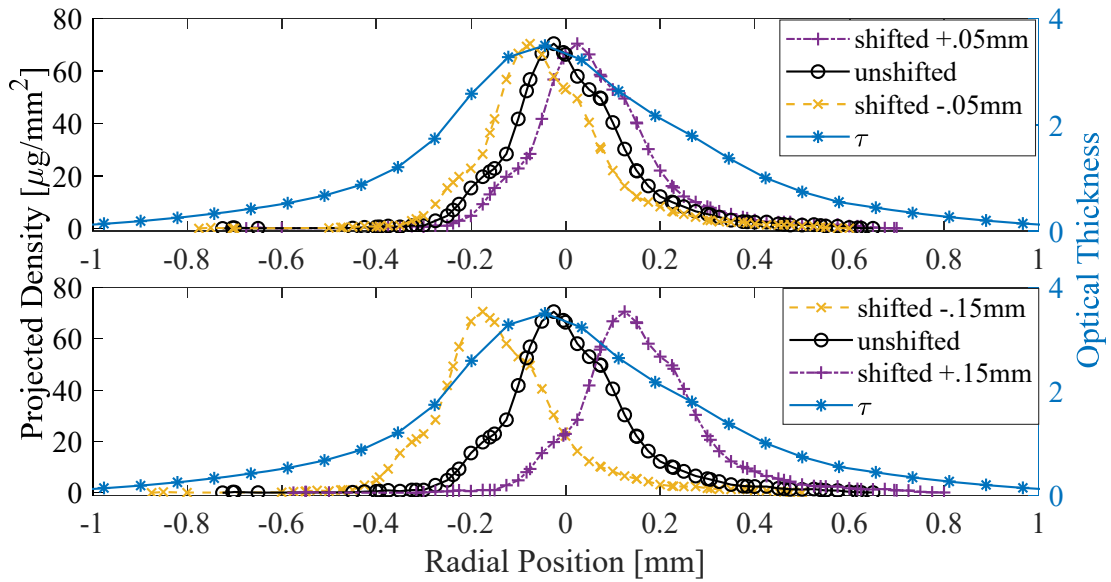
Figure 43: Projected density data shifted by ±0.05 mm and ±0.15 mm to assess the importance of the spatial co-alignment of the data sets

Figure 44 shows the SMDs that are calculated after shifting the projected density values

by ±0.05 mm (top) and ±0.15 mm (bottom). The SMDs are found only in the optically thin and

moderate optical thickness regions of the spray (τ < 2.0). The unshifted SMDs are indicated with

a purple +, the positively shifted SMDs are shown with a blue ○, and the negatively shifted

SMDs are shown with a red x. Figure 45 shows the relative error in the quantified SMD for the

same conditions shown in Figure 43. The figures show that even a relatively small misalignment

of the two data sets can have a significant effect on the calculated SMD. Figure 45 indicates that

on average the percent difference between the two SMDs is about 30% but can get as large as

145%. A misalignment of the data sets by up to ±0.05 mm could be reasonably judged as "co-aligned" by an observer of the overlapping data sets. Thus, the uncertainty in quantified SMD is highly dependent on the accuracy of co-aligning both data sets. As such, shifting via FWHM seems to reasonably align the datasets and should continue to be used in the future. Increasing the data misalignment by 0.1 mm contributes to an even more substantial error in the measured SMD, resulting in relative errors greater than 100% at all viable measurement locations. Although a misalignment of this magnitude would be more obvious and less likely to be considered as a viable co-alignment of the data sets, these rather large errors indicate how essential it is to carefully consider the spatial alignment of the two data sets from both facilities.
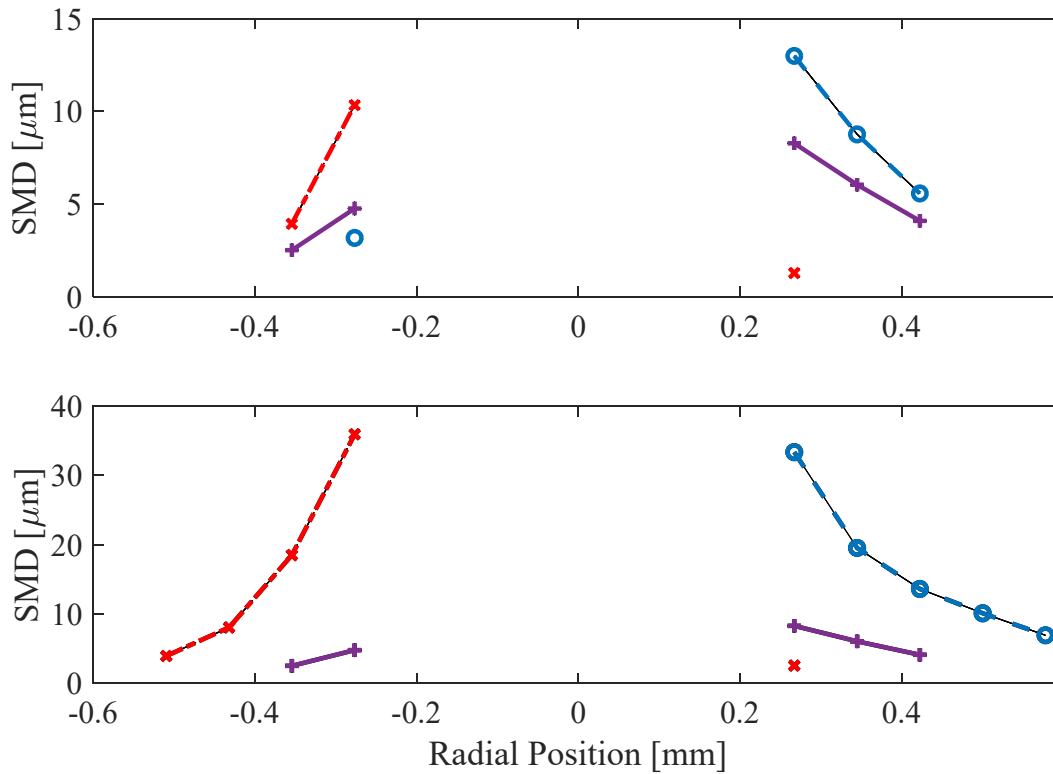
Figure 44: SMDs for the original and shifted by ±0.05 mm (top) and ±0.15 mm (bottom) for Spray D 2.4 kg/m³ 50 MPa at 14 mm away from the nozzle
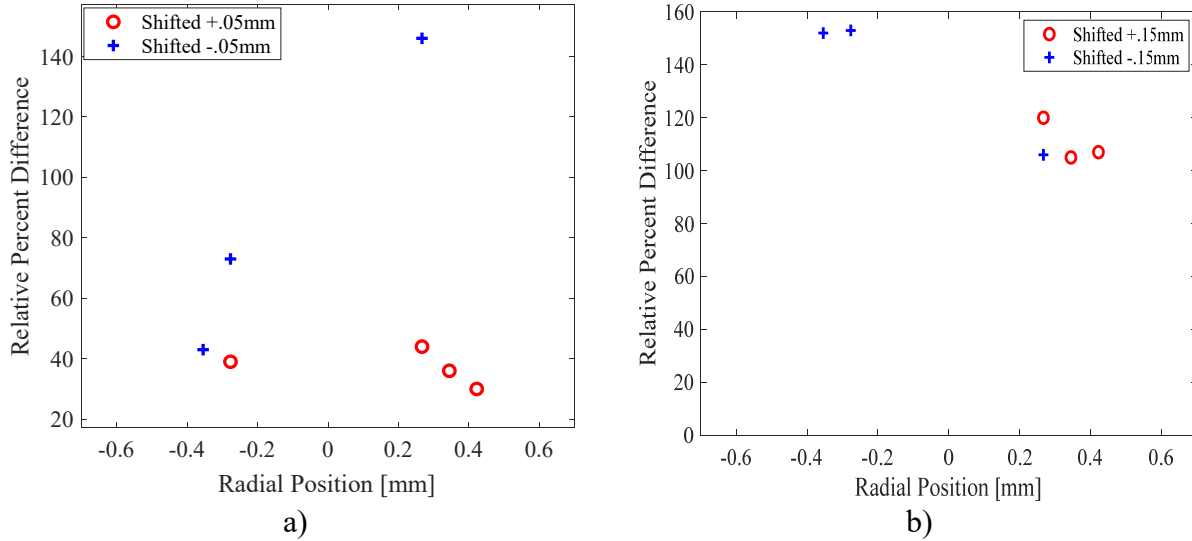
Figure 45: Relative percent differences for the Spray D 2.4 kg/m3 50 MPa at 14 mm away from the nozzle for shifting by a) ±0.05 mm and b) ±0.15 mm

The next portion of the data processing uncertainty analysis consisted of assessing the relative importance of the injector orientation. Previously, it has been shown that significant asymmetries are present in the spray thus precipitating a need to assess the importance of the injector orientation [9, 46]. In Phase I, the injector orientation between the two facilities was off by about 10°. This uncertainty analysis enables an assessment of the sensitivity of the SMD measurement to relative differences in facility-to-facility injector orientation. This analysis consisted of processing the projected density with 0° and 180° orientations. The orientation of the optical thickness values was not changed. While flipping the data sets by 180° may not capture all the possible asymmetries in the spray, it allowed for an analysis of the importance of the injector orientation between the two facilities. Figure 46 illustrates the asymmetries present in the spray, as illustrated by the "shoulders" in the projected density values. The projected density values do not decrease to zero at the same rate, indicating an additional asymmetry. This asymmetry in slope of the projected density measurements relative to the change in optical thickness is one of the driving factors in relative percent differences for both shifting the data and changing the spray orientations.
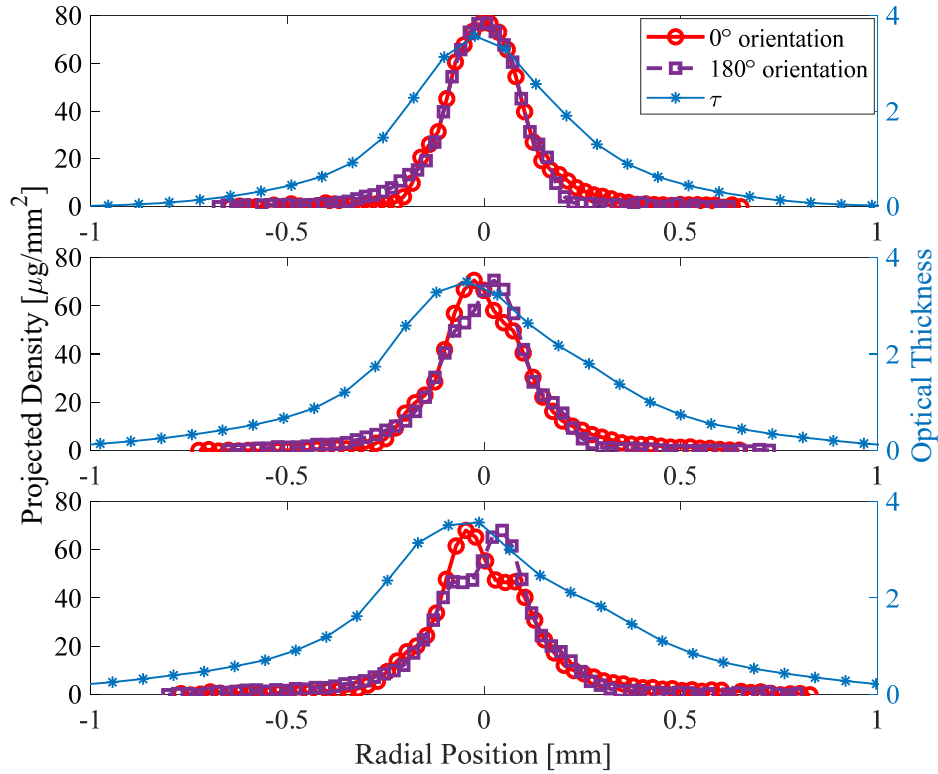
Figure 46: Optical thickness at 0° and the projected density values at 0° and 180° for Spray D 2.4 kg/m³ 50 MPa at 10, 14, 16 mm axial locations (top to bottom)

When the data is processed for both injector orientations, the measurement ratio and the SMD are affected. Figure 47 shows the SMD values for both injector orientations for the 2.4 kg/m³ ambient density case 0° (shown with a red ○) and 180° (shown with a purple □) orientations. For the 10 and 14 mm axial locations, the maximum difference in the droplet size is 3 μm. The high ambient density condition (22.8 kg/m³) also shows a difference in the SMD of about 3 μm. At 16 mm away from the nozzle exit, the maximum difference in the droplet size is only 0.2 μm. As distance from the nozzle increases, the periphery of the spray becomes more symmetric whereas the centerline of the spray becomes more asymmetric. This trend is seen in Figure 46. Figure 48 demonstrates that the relative error between the two injector orientations ranges from less than 1% up to 60%. Overall, this rotational alignment uncertainty analysis indicates the importance of matching the injector orientation. In Phase II of this work, the

injector orientation for both facilities was matched to minimize error due to rotational misalignment.
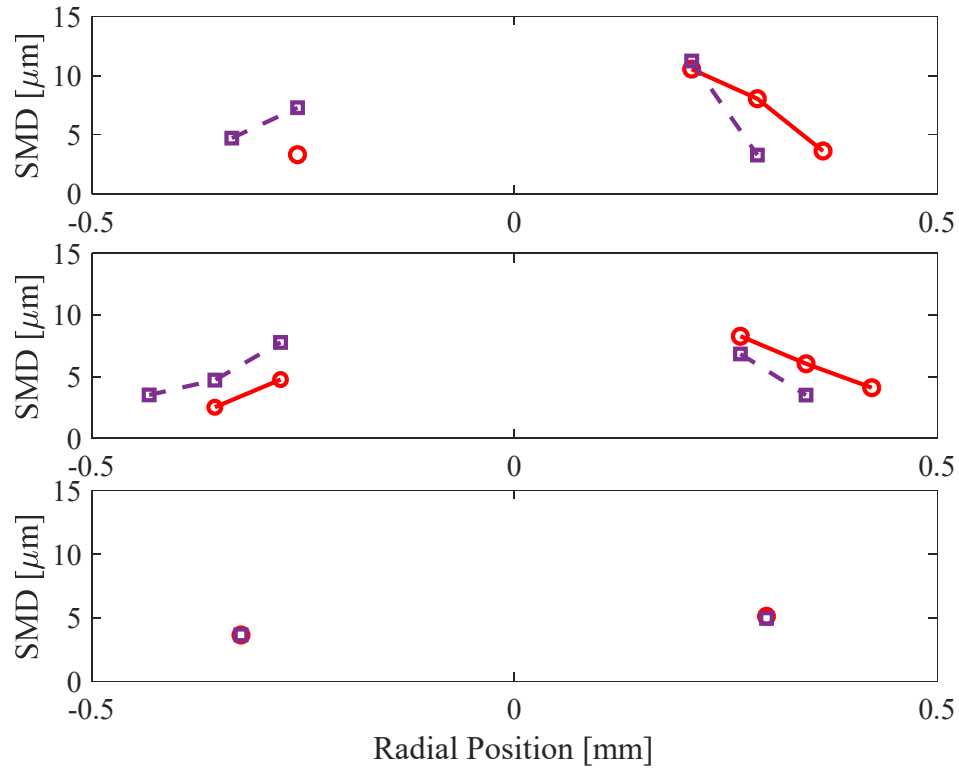
Figure 47: SMDs for the 10, 14, 16 mm (top to bottom) axial locations for Spray D 2.4 kg/m³ 50 MPa 0° and 180° orientations
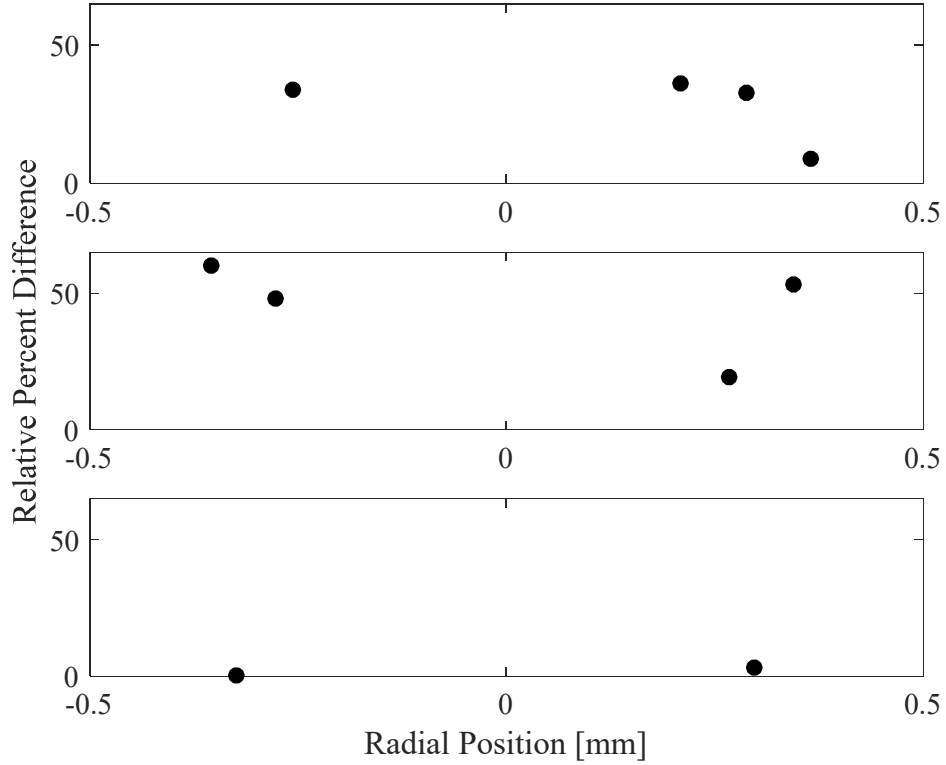
Figure 48: Relative percent differences for the 0° and 180° orientations for Spray D 2.4 kg/m³ 50 MPa at 10, 14, 16 mm away from the nozzle

4.3 Phase II SMD results

The Phase II SMD results are shown for Spray A at 22.8 kg/m³ ambient density and 50 MPa injection pressure [10]. Phase II DBI experiments improved the SAMR diagnostic by utilizing a single wavelength 633 nm red LED as the light source. Using a longer wavelength helps to suppress multiple scattering thus improving the fidelity of the optical thickness measurement in the intermediate scattering regime ($1<\tau<2$). Additionally, phase II employed the multiple scattering correction, so the SMDs were calculated through the entirety of the spray. One drawback of the Phase II results was that the DBI data was collected with the built-in shading function on the camera disabled, resulting in a loss of dynamic range of approximately 1000 counts.

Figure 49 shows the radial distribution of SMDs using the measured and corrected optical thickness values. At the periphery of the spray where $\tau < 1$ and single scattering events are safely

assumed, the multiple scattering correction was not applied, so the SMDs for the original and corrected values overlap. An average SMD of 6 μm is measured along the spray centerline. While the distribution of SMD remains fairly uniform for a large proportion of the spray width, it sharply rises at the peripheral region of the spray. This is particularly evident farther downstream of the injector at 16 mm axial location. As stated earlier, this counterintuitive trend has been witnessed by other researchers and can be attributed to droplet collision and coalescence due to shear effects and the transport of large droplets from the core region at the spray tip [10, 48, 49].
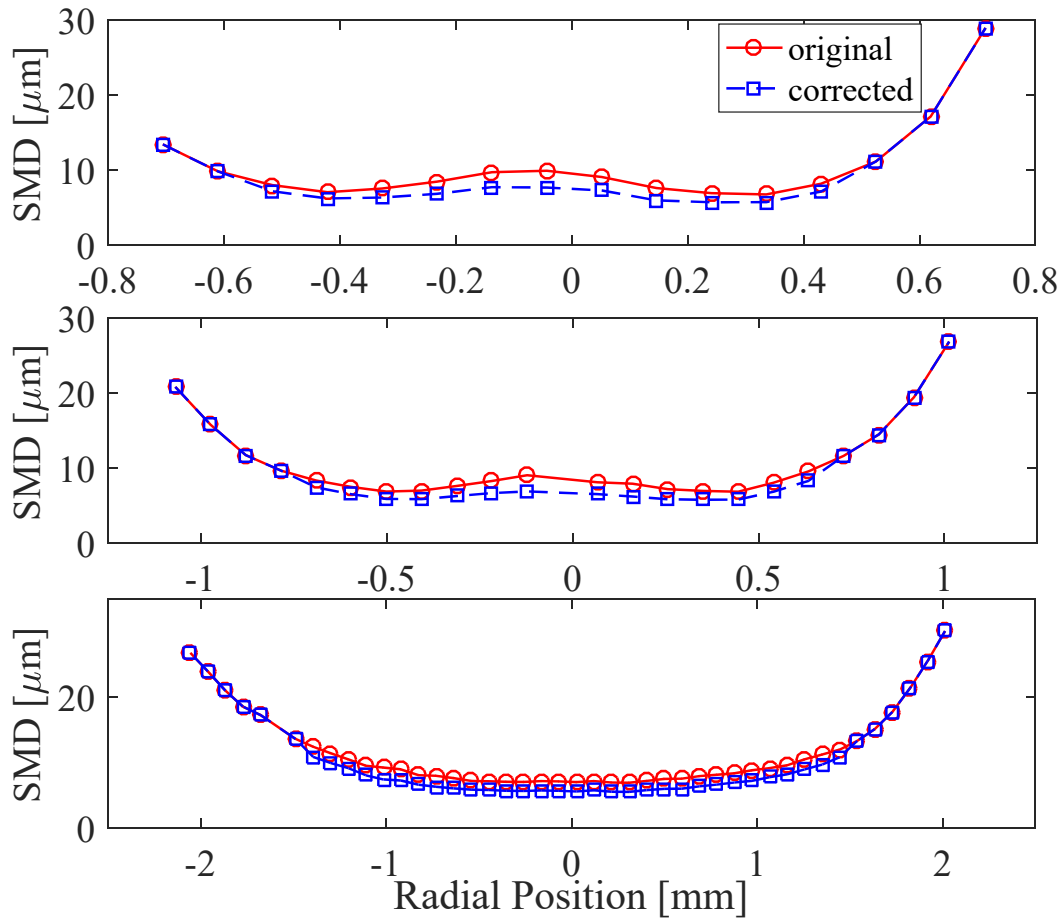
Figure 49: Radial distribution of measured and corrected SMDs for Phase II Spray A 22.8 kg/m3 50 MPa at 8, 10, 16 mm

Figure 50 shows a detailed view at the regions where the multiple scattering correction was applied. In these regions, the uncorrected results overestimate the size of droplets by a maximum

of about 2 μm. This is attributed to the contribution of multiple scattering phenomenon, which results in an underestimation of the local optical thickness (as shown in Figure 29) and hence an overestimation of the corresponding droplet sizes.
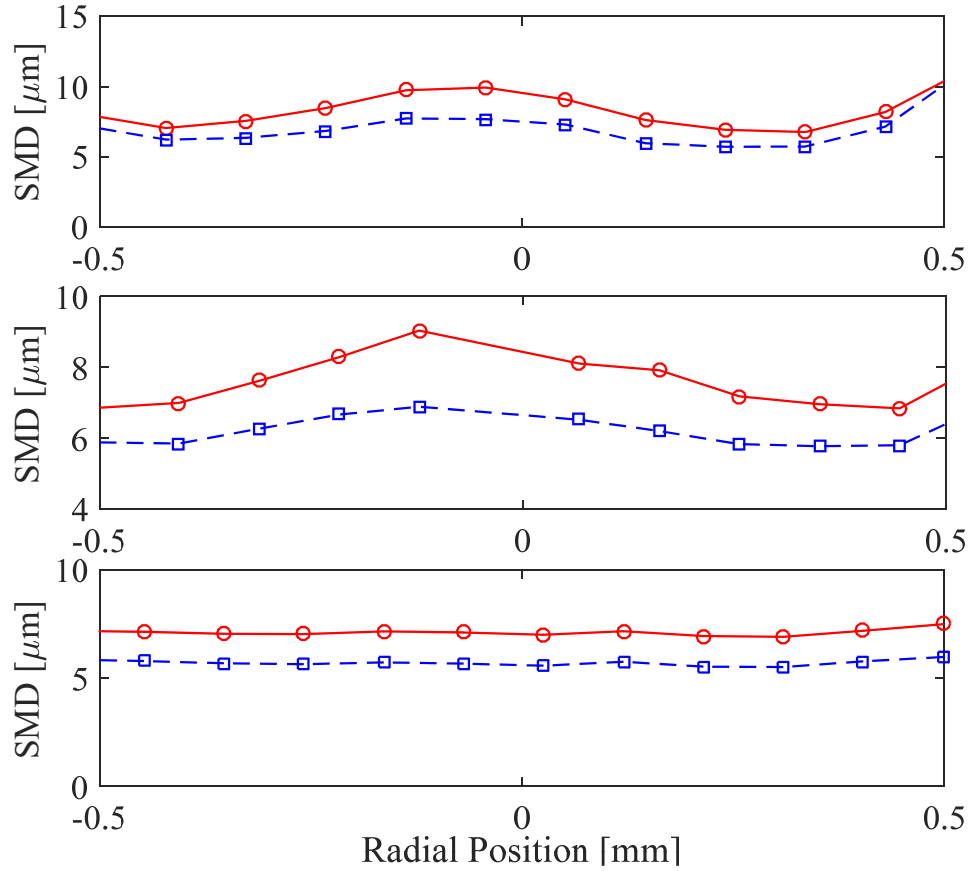
Figure 50: Detailed view of the Phase II SMDs for Spray A 22.8kg/m3 50MPa at axial locations of 8, 10, 16 mm (top to bottom)

4.4 Phase III SMD Results

Phase III used the ideal diagnostic setup for both diffuse back illumination and x-ray radiography for the SAMR technique to measure spray droplet sizes. The DBI setup used an ideal diffuse and uniform background and the maximum dynamic range of the camera. The finite collection angle is decreased, and a finer measurement resolution is achieved. A smaller collection angle reduces the light that is redirected into the detection system and thus reduces the errors associated with multiple scattering. A finer measurement resolution is beneficial because it

provides more locations where the measurement ratio can be conducted. The radiography

measurements increased the signal to noise ratio (SNR) by adding Cerium to the fuel and by

increasing the number of fuel injections that were ensemble averaged. Increasing the SNR

provides additional regions where the measurement ratio could be conducted. In phase III the

data was taken at 3 injector orientations, which allows for analysis of the asymmetries present in

the spray. Figure 51 shows an example of the original and corrected SMDs for the Spray D 1.2

kg/m³ density at 50 MPa injection pressure and a 90° viewing angle. Without the multiple

scattering correction, the measurement indicates that the droplets can reach up to 40 µm at the

spray centerline. This is very large and has not been seen in the literature. The multiple scattering

correction brings the SMDs at the centerline down to 20 µm, which is similar to results in the

literature [23]. The droplets decrease in size traversing across the spray.
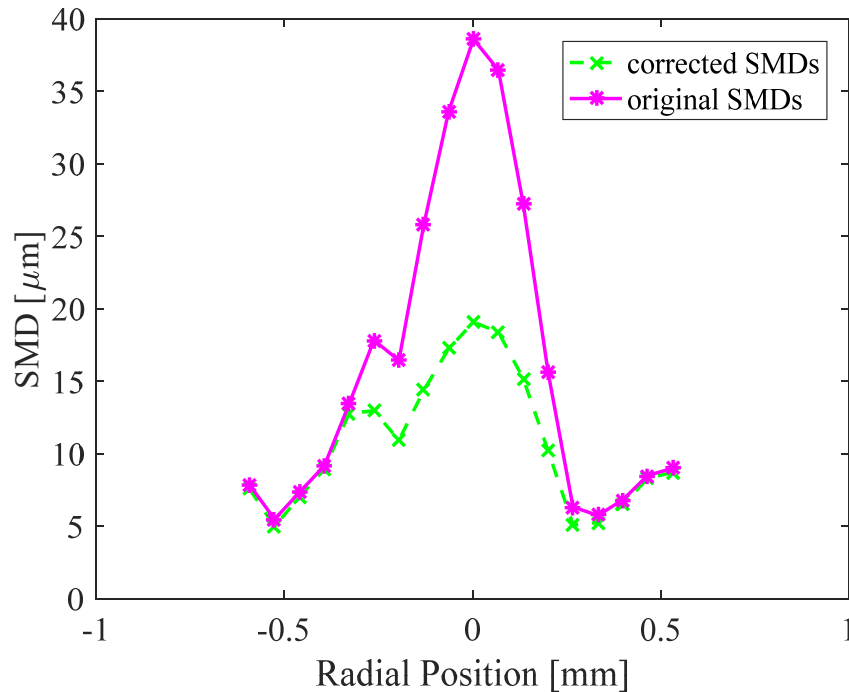
Figure 51: Phase III Spray D 1.2 kg/m³ 50 MPa 90° orientation for corrected and original SMDs at 10 mm axial location
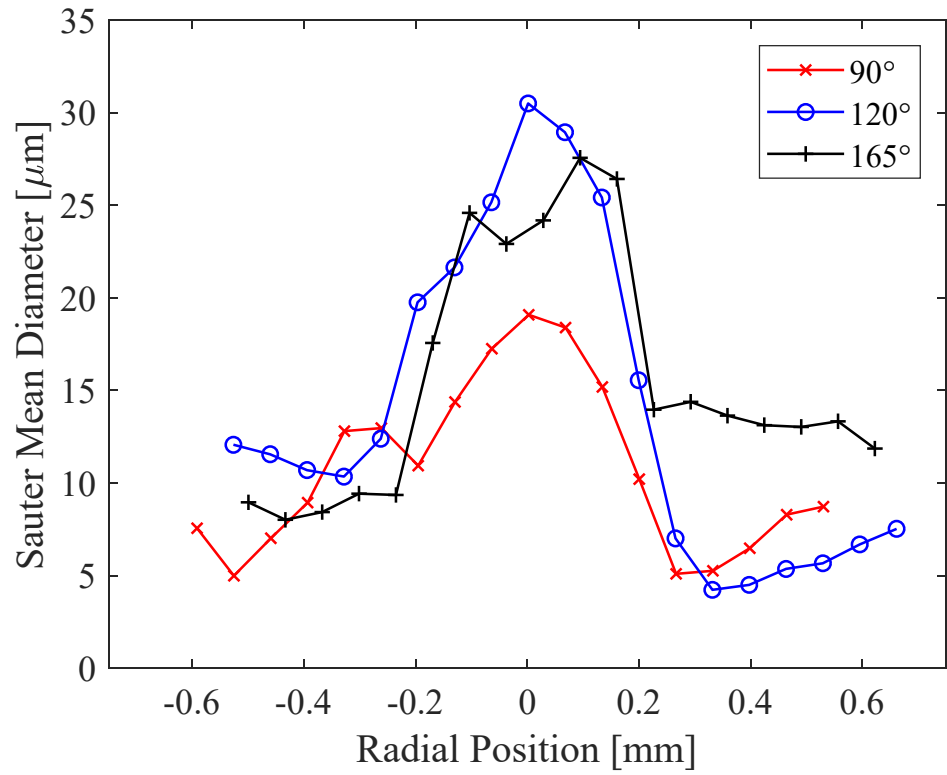
a)
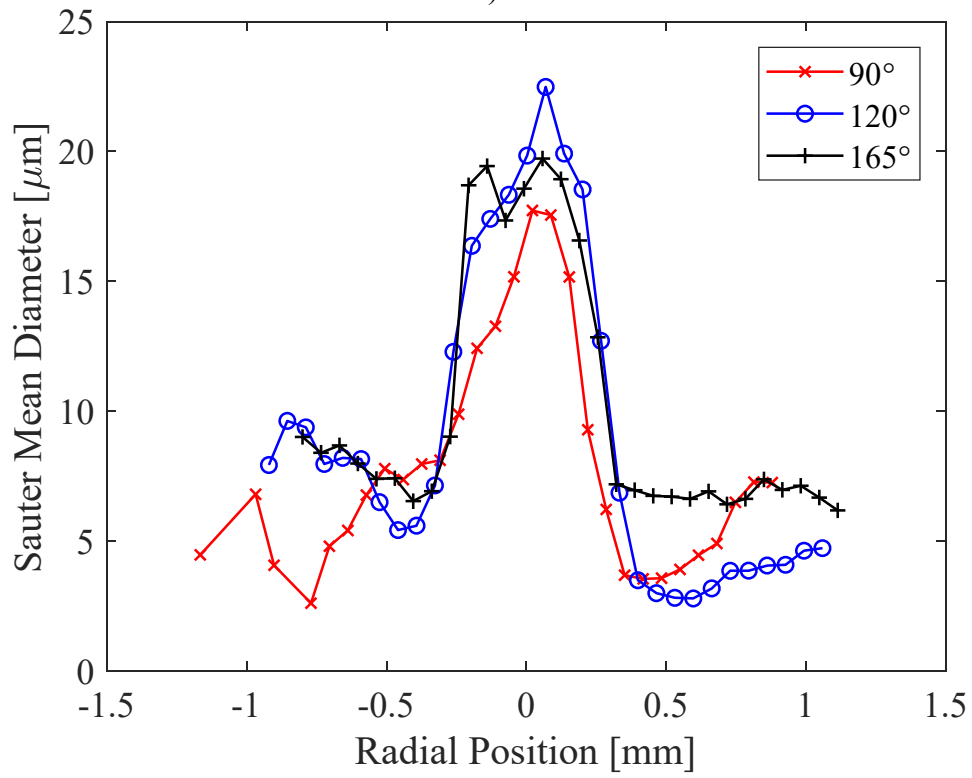
b)
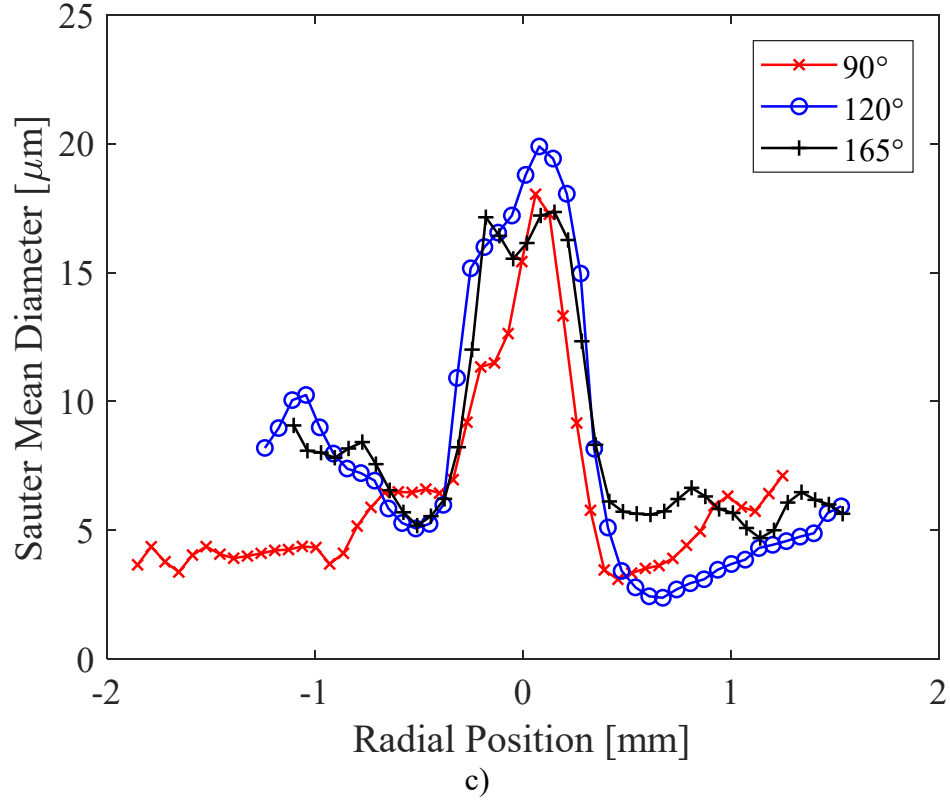
Figure 52: Phase III SMDs for Spray D 1.2 kg/m³ 50 MPa 90°, 120°, 165° orientations at a) 10, b) 16, and c) 20 mm

Figure 52 a-c shows the Phase III SMD results at 1.2 kg/m³ 50 MPa at 90°, 120°, and 165° orientations for axial locations at 10, 16, 20 mm. Each of the plots shows the same general trends. Larger droplets exist at the spray centerline, and they decrease in size as radial position increases. Additionally, increasing axial distance results in decreasing droplet size. Besides these two trends, Figure 52 clearly shows the asymmetries present in the spray. If the spray was perfectly symmetric, the radial distributions of droplet size would overlap, but this is not evident in the figures. Figure 52 a) shows a particularly interesting trend; the 90° orientation shows a much smaller droplet size throughout the spray compared to the 120° and 165° orientations. At the centerline, the difference in SMD between the 90° and 120° is 11.4 μm. The 165° orientation shows a bimodal distribution, as evident by the double peak of 24.6 μm and 27.6 μm at -.10 mm and .09 mm, respectively. At the 16 mm axial location (seen in Figure 52b), the droplet size

radial distribution of the 120° and 165° orientations converge at the spray periphery (-.34 to -.19 mm) and (.19 to .32 mm). The 165° orientation at 16 mm also shows the bimodal distribution, with both SMD peaks hovering around 19 µm at -.14 mm and .06 mm. At the 20 mm axial location (Figure 52c), the 120° and 165° orientations converge even more. The peak/centerline SMDs also converge for 90°, 120°, and 165° orientations.

Table 11: Peak SAMR SMD data for conditions presented in Figure 52 a-c

	10 mm	16 mm	20 mm
90°	19.1 µm	17.7 µm	18.0 µm
120°	30.5 µm	22.5 µm	19.9 µm
165°	27.6 µm	19.7 µm	17.4 µm
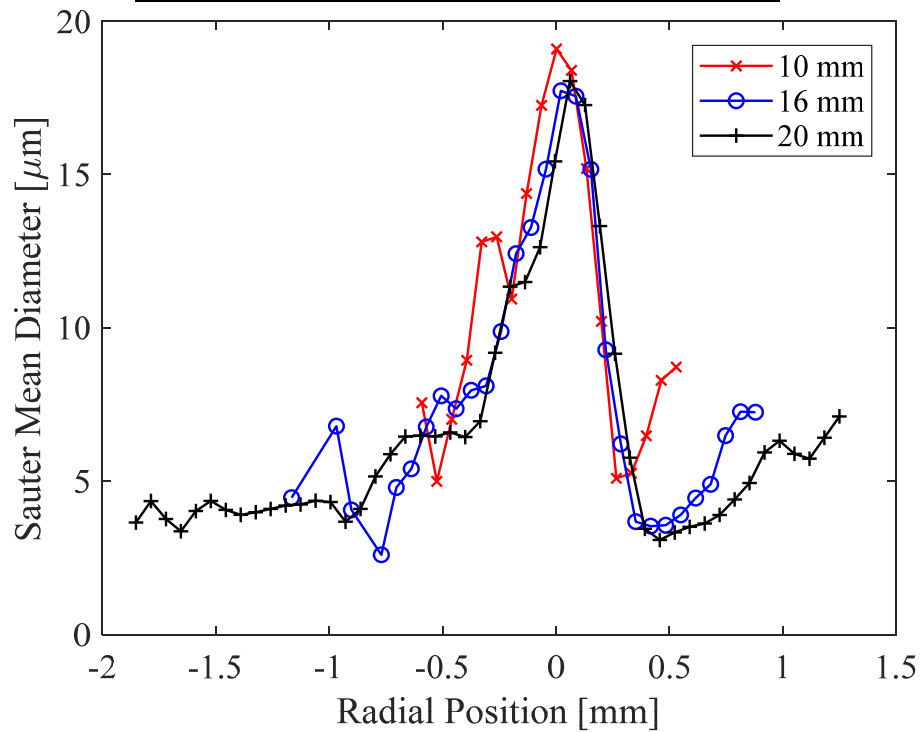
Figure 53: Phase III SMDs for Spray D 1.2 kg/m³ 50 MPa for 90° orientation at 10, 16, 20 mm
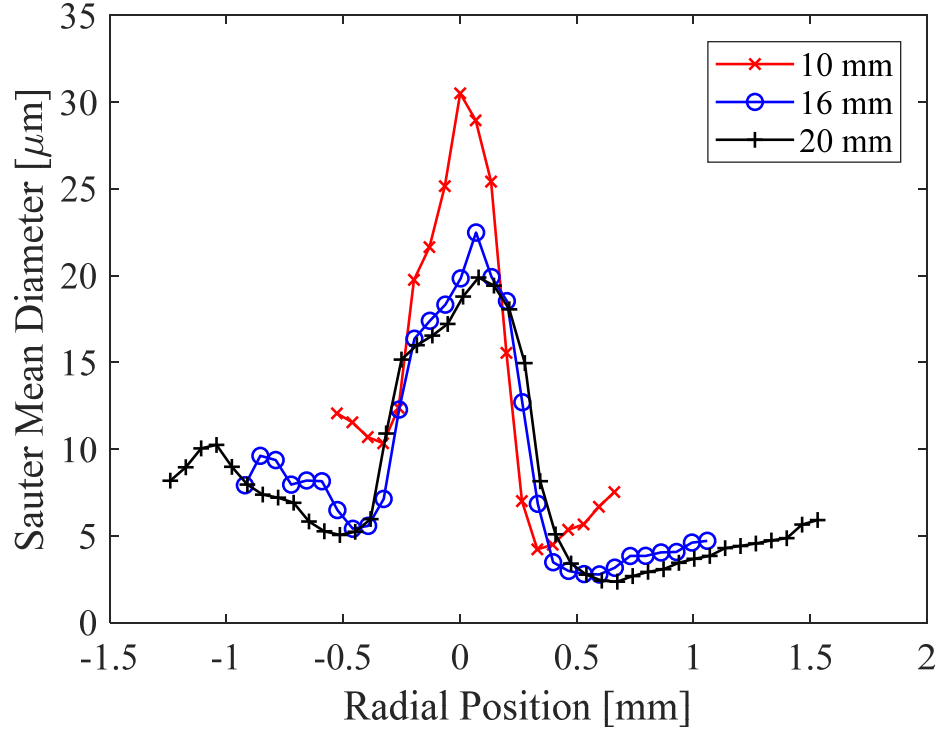
Figure 54: Phase III SMDs for Spray D 1.2 kg/m^3 50 MPa for 120° orientation at 10, 16, 20 mm
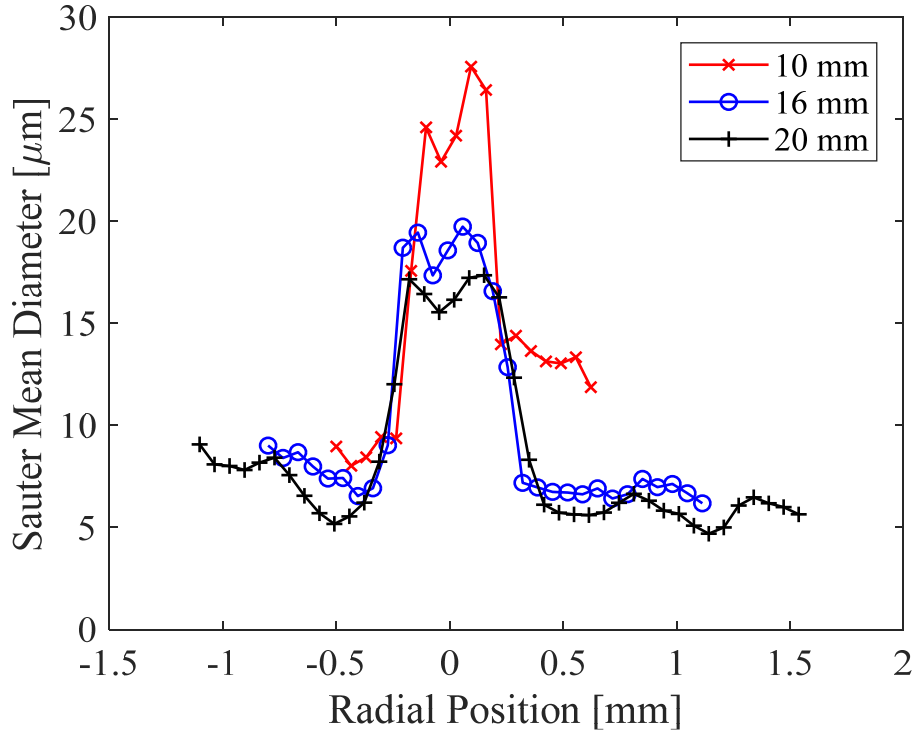
Figure 55: Phase III SMDs for Spray D 1.2 kg/m^3 50 MPa for 165° orientation at 10, 16, 20 mm

Figure 53-Figure 55 show the SAMR SMDs for Spray D 1.2 kg/m^3 50 MPa at each

orientation with all the axial positions overlaid. Figure 53 shows the SMDs for the 90°

orientation. This plot illustrates all three axial locations overlapping near the spray centerline, with the peak SMD value decreasing slightly with axial distance. At 10 mm, the peak SMD is 19 μm. At 16 and 20 mm, the SMD hovers around 17.5-18 μm. As the radial position increases (from 0 to ±.5 mm), the SMD value decreases. From 0 to ±.5 mm, the SMDs overlap for 16 and 20 mm locations, indicating that a stable droplet size has been reached. However, for all three axial conditions, on the positive half of the spray from .5 to 1 mm, the SMD begins to increase. This interesting trend could be attributed to droplet collision and coalescence. The negative side of the spray also shows an interesting trend at the 10mm location, where a shoulder is seen around -.3 mm with an SMD value of 12.8 μm. Figure 54 and Figure 55 show the SMDs for the 120 and 165°, respectively. Both figures show similar trends. The 10 mm axial location shows a significantly larger droplet size than the 16 and 20 mm locations throughout the entirety of the spray. This is consistent with Phase I trends and many sources in the literature. Larger droplets exist closer to the nozzle, and they decrease in size as the distance from the nozzle increases. Figure 54 shows that at the 120° a singular SMD peak value occurs at the spray centerline, whereas Figure 55 shows that for the 165° orientation a double peak in SMD is seen. Both peak SMDs are centered around the spray centerline. The peak SMDs at 10 mm are 27.6 μm and 24.6 μm; at 16 mm the peak SMDs are 19.7 μm and 19.4 μm; at 20 mm the peak SMDs are 17.4 μm and 17.2 μm. It is quite curious that at this injector orientation, this bimodal distribution is very evident.

Figure 56-58 show two-dimensional SMD droplet sizing maps of this same data. These maps provide a better way to visualize the droplet evolution in space. These droplet sizing maps show that, as expected, the droplets decrease in size with increasing axial and radial position. The SAMR technique is demonstrated to yield a reasonable measurement of diesel spray droplet

sizes, with the expected range of SMD reported in prior literature and following the expected trends in spatial evolution.
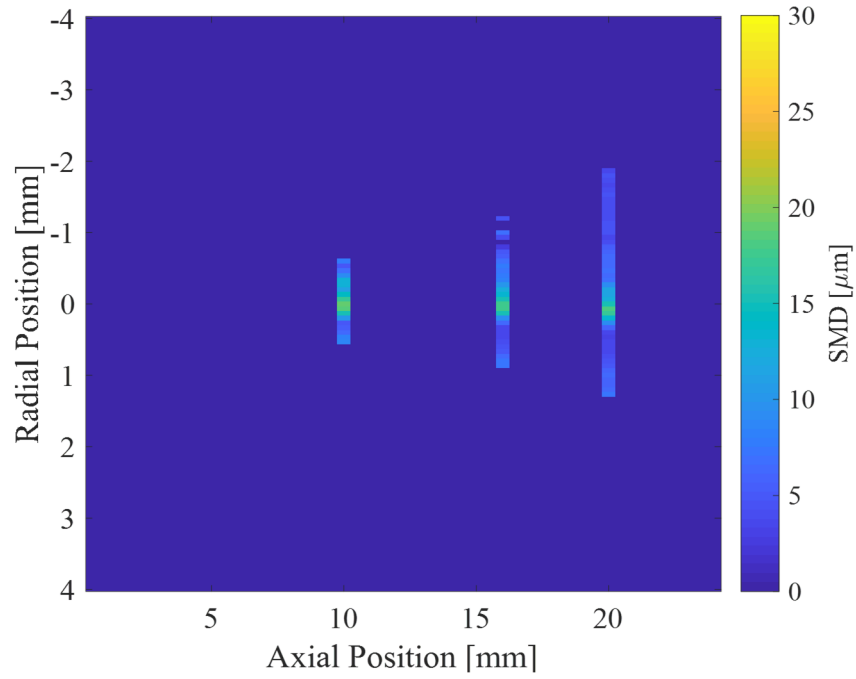
Figure 56: Phase III 2-D SMD map for Spray D 1.2kg/m³ 50MPa at 90° orientation
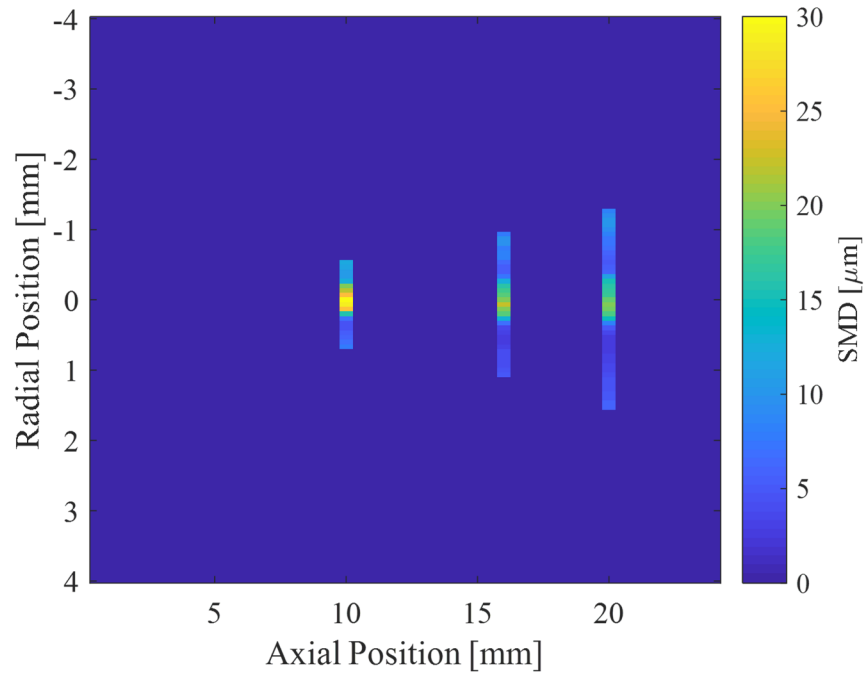
Figure 57: Phase III 2-D SMD map for Spray D 1.2kg/m³ 50MPa at 120° orientation
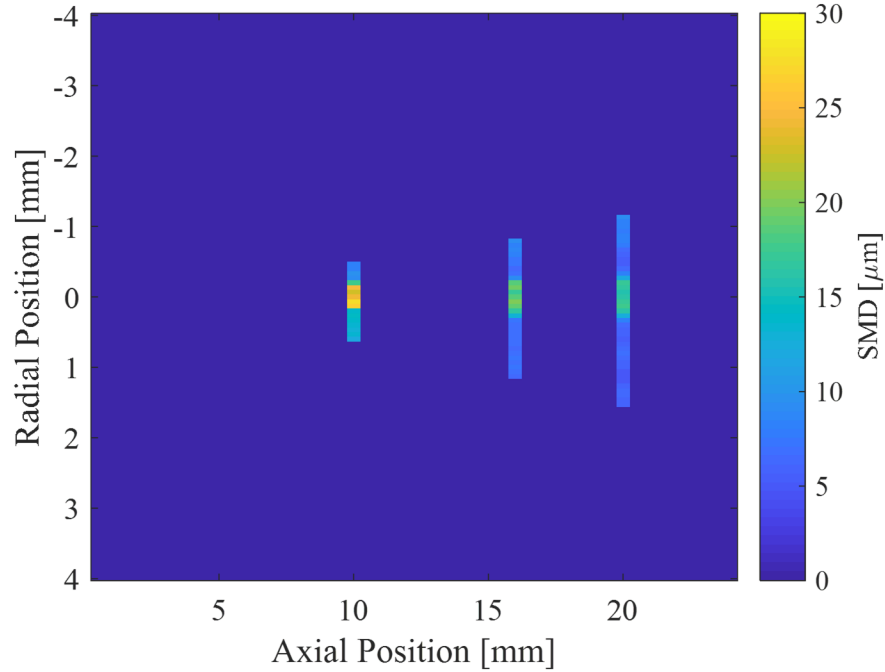
Figure 58: Phase III 2-D SMD map for Spray D 1.2kg/m³ 50MPa at 165° orientations

Figure 59-61 show two-dimensional Sauter Mean Diameter plots which have been interpolated along the axial dimension from 10 to 20 mm using the MATLAB built in "scatteredInterpolant" function. These plots are expected to be particularly useful for model validation efforts where visualization of interpolated scalars is typical. All the figures have the color bar limits from 0 to 30 μm which enables a comparison of the injector orientations. The 90° orientation shows much smaller droplets than the 120° and 165° orientations, as seen previously. The figures also show the general trend that larger droplets exist near the spray centerline and they decrease in size as axial distance increases. Additionally, the droplets decrease in size as radial distance increases, until they reach a certain radial position where the droplet size begins to increase slightly.
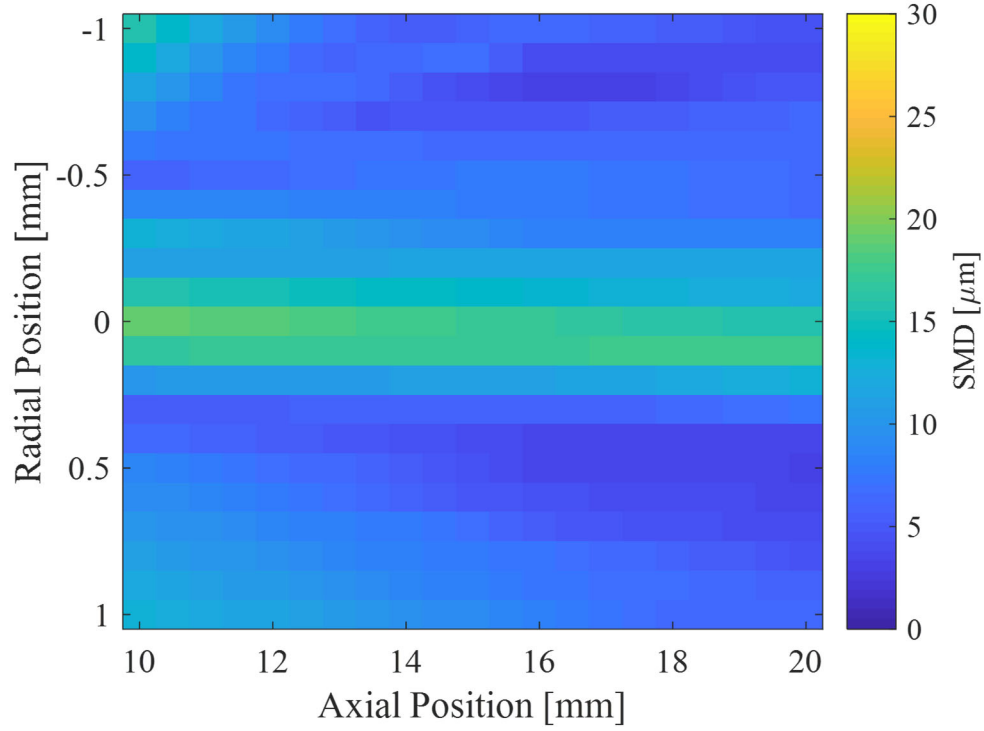
Figure 59: Phase III 2-D SMD map interpolated from 10 to 20 mm for Spray D 1.2 kg/m³ 50 MPa at 90° orientation
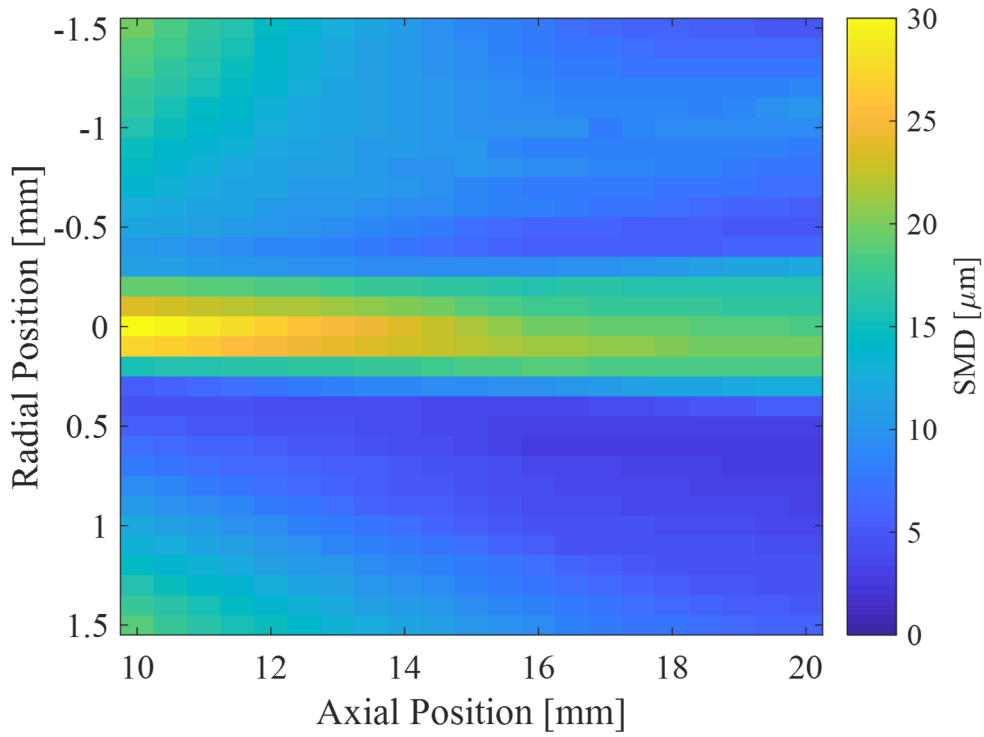
Figure 60: Phase III 2-D SMD map interpolated from 10 to 20 mm for Spray D 1.2kg/m³ 50 MPa at 120° orientation
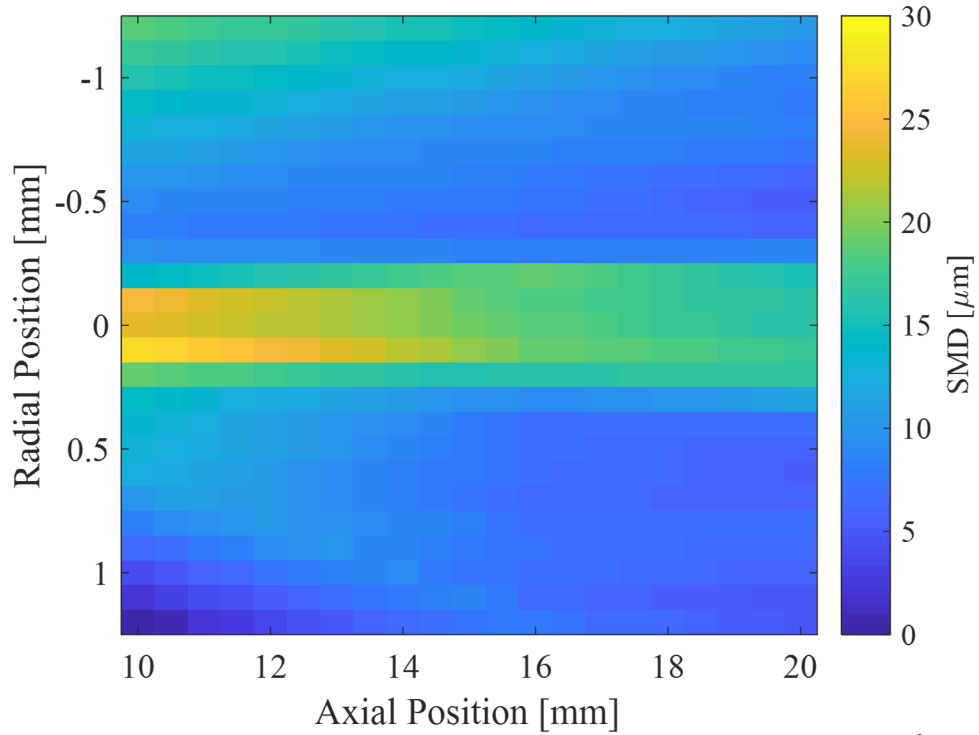
Figure 61: Phase III 2-D SMD map interpolated from 10 to 20 mm for Spray D 1.2 kg/m³ 50 MPa at 165° orientation
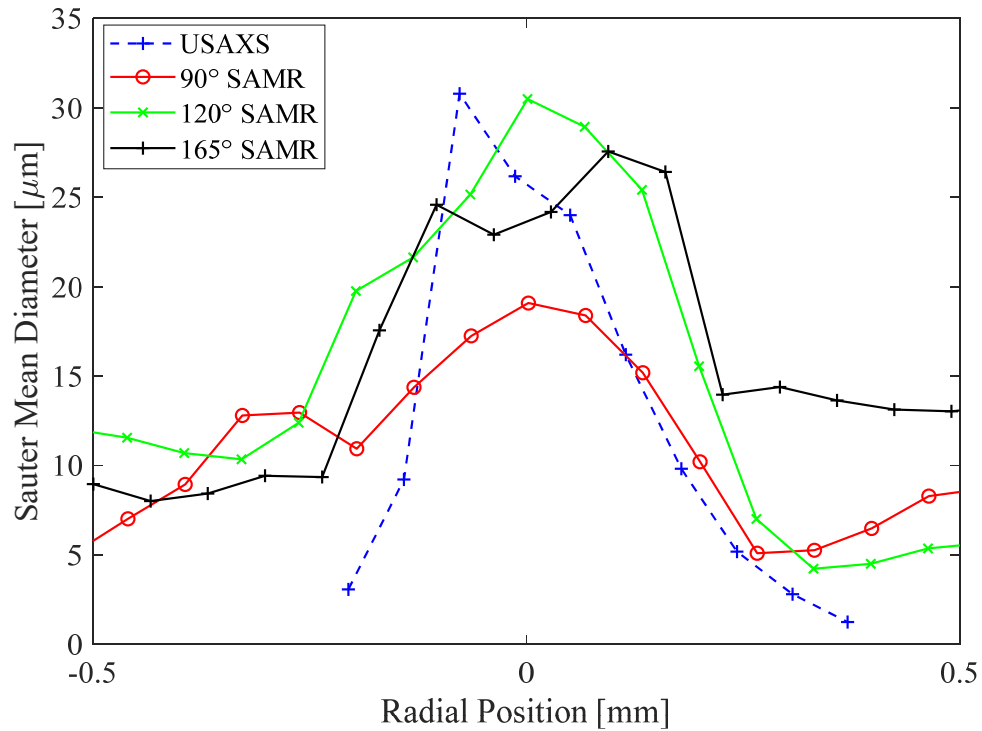
Figure 62: Comparison of SMDs for Phase III (90, 120, 165°), and USAXS (Cycle2017_3) for Spray D 1.2 kg/m³ 50 MPa at an axial location of 10 mm

Table 12: Peak SAMR and USAXS SMD data for conditions presented in Figure 62

USAXS		120°			165°		
Radial Position (mm)	SMD (µm)	Radial Position (mm)	SMD (µm)	% Difference in SMD	Radial Position (mm)	SMD (µm)	% Difference in SMD
-0.077	30.8	0.0014	30.5	1%	.09	27.6	11%

Table 13: Periphery SMD data for Spray D 1.2 kg/m3 50 MPa at an axial location of 10 mm for 90° SAMR data and Cycle2017_3 USAXS

USAXS		90°		% Difference in SMD	% Difference in location
Radial Position (mm)	SMD (µm)	Radial Position (mm)	SMD (µm)		
0.11	16.2	0.13	15.2	6 %	16%
0.19	9.8	0.20	10.2	4%	11%
0.24	5.2	0.27	5.1	2%	9%

Figure 62 shows a comparison of the Phase III SAMR results (at 90°, 120°, 165°
orientations) with the Cycle2017_3 USAXS results (at 0° orientation) for the condition Spray D
1.2 kg/m^3 50 MPa at 10 mm axial location. These results show good agreement despite the
differing injector orientations. The 120° and 165° SAMR SMD results show good agreement
with the USAXS results at the spray centerline as demonstrated in Table 10. The peak 120° SMD
differs from the USAXS SMD by .98%, whereas the peak 165° SMD differs by 11.10%. The 90°
orientation and the USAXS SMDs results converge at the spray periphery. Table 11 lists the
periphery SMD data for the 90° orientation and the USAXS results. The minimal percent
differences indicate the very good agreement between the two diagnostics. The SAMR
diagnostic shows better agreement with the USAXS measurement for Phase III compared to
Phase I (see Figure 36). The SAMR diagnostic is showing reasonable agreement with accepted
droplet sizing results. Furthermore, this proves that the SAMR diagnostic is a promising droplet
sizing technique which can aid in the understanding of the physics governing spray atomization
in diesel relevant sprays and ultimately aid in spray submodel development.

CHAPTER 5

CONCLUSIONS AND FUTURE WORK

In this thesis work, a novel spray droplet sizing diagnostic, called the scattering-absorption measurement ratio (SAMR) technique, was presented which leverages joint measurements at Georgia Tech and Argonne National Laboratory to quantify the SMD distribution in diesel relevant sprays. SAMR utilizes diffuse back illumination measurements of optical thickness from Georgia Tech and spray radiography measurements of projected density from Argonne National Laboratory. Taking a ratio of these two measurements, in combination with application of Mie-scattering theory, produces a measurement of the 2D volume-projected Sauter Mean Diameter. Two-dimensional droplet sizing maps have been developed, which provide an understanding of the spatial droplet evolution. The SAMR diagnostic and resulting data developed as a part of this thesis can assist in the understanding of the physics governing diesel relevant sprays and aid in the improvement of spray submodels for engine CFD codes.

The main contributions of this thesis are:

- improving the DBI setup specifically for the SAMR technique

- establishing the comprehensive data processing methodology which jointly processes the data sets from each experimental facility

- extracting detailed droplet sizing information in regions of the spray that are typically unattainable by most droplet sizing techniques

- a detailed uncertainty analysis of the SAMR diagnostic

These will be elaborated upon in the subsequent paragraphs.

79

The results presented in this work consisted of three data campaigns, each improving on the previous campaign to reduce measurement uncertainties and maximize measurement bandwidth of the SAMR technique. The optimized diffuse back illumination setup utilizes a pulsed 633 nm light source with the shading calibration enabled for the high-speed Photron SA-X2 camera. The optics were arranged such that a uniform light source was created. This new DBI setup is enhanced for use with the SAMR technique. It was crucial to develop a setup which provided a uniform light intensity background that minimized fluctuations in light intensity across the image. This new DBI setup deviated from the setup employed by Westlye and others within the ECN [37, 39]. The DBI setup proposed by the ECN focused on the reduction of beam steering, which is not applicable in a non-vaporizing environment that the SAMR diagnostic is currently employed. Additionally, the projected pixel size was minimized which allowed for the SMD to be quantified at a higher resolution throughout the spray. The enhanced DBI technique utilized a correction equation from the literature to take into account the adverse impact of multiple scattering on the optical thickness data for optically thick regions of the spray. The x-ray radiography experiments at Argonne also took place in three phases. The experiments in the third phase used a cerium additive to the fuel to improve the SNR. The SAMR diagnostic was also enhanced by matching the injector orientations for both facilities.

A major contribution of this work was establishing the data processing methodology to jointly process both projected density and optical thickness data sets. Quantifying the SMD distributions from the joint scattering-absorption measurements involved the development of several data processing steps. These steps included: co-aligning the optical thickness and projected density measurements by centering the FWHM of the radial distributions, binning the projected density data in order to compare consistent measurement volumes between the DBI

and radiography experiments, identifying the regions where each of the measurements could be accurately interpreted, curve fitting the data, finding an average projected density in the measurement volume using this curve fit, taking a ratio of the projected density and optical thickness values, and finally applying Mie-scatter calculations to quantify the SMD. Once the data was appropriately processed, the Sauter Mean Diameter could be extracted.

As shown in this work, each of the data processing steps can introduce error into the final SMD value. The influence of these steps was quantified in terms of measurement uncertainty. One source of experimental uncertainty is due to uncertainty in relative positioning between the two measurements. The measurement uncertainty introduced by co-alignment of the sprays was examined by assessing the impacts of spatial and rotational co-alignment on the quantified SMD. Misalignment of the data sets by 0.05 mm resulted in an uncertainty in the quantified SMD of about 30-70%, thus indicating the necessity of data co-alignment via FWHM method. The effect of relative rotational alignment or measurement viewing angle was also analyzed by comparing the SMDs calculated from projected density measurements orientated at viewing angles of 0° and 180°. This level of rotational misalignment between the two data sets produced an uncertainty in the quantified SMD of less than 1% up to 60%. Thus, measurement errors due to either rotational or translational misalignment of the spray coordinate systems are of similar magnitude and can produce SMD measurement uncertainties of up to 60-70%. In Phase III, steps were taken experimentally to minimize these co-alignment uncertainties to improve the accuracy of the SAMR measurement, like matching injector orientation.

For all three data campaign phases, the SMDs measured using the SAMR technique demonstrated magnitudes and trends that are consistent with previous data in the literature, validating the SAMR approach. For the low ambient density cases (1.2 and 2.4 kg/m^3), larger

droplets exist near the spray centerline. The droplets decrease in size as axial distance increases. Additionally, the droplets decrease in size as radial distance increases, until they reach a certain radial position where the droplet size begins to increase slightly. Whereas for the high ambient density case (22.8 kg/m^3), the SMDs are fairly constant around 6-7 μm near the spray centerline. As the radial distance from the spray centerline increases, the droplets also begin to increase in size. Additionally, this work proved that the spray produced from the ECN Spray D injector is indeed asymmetric, which results in different SMD values depending on the measurement viewing angle.

Some unique droplet sizing trends identified through this work should be further explored in the future. For example, the Phase III low ambient density cases at 90 and 120° showed that the droplet sizes begin to increase as distance from the spray centerline increases. This trend could be further explored by conducting a SAMR data campaign which focuses on the periphery of the spray. These results could be compared with the USAXS data for validation. Another unexpected feature that can be further explored with another SAMR data campaign is the increasing SMD along the periphery of the spray for the higher ambient density cases.

Additionally, it would be useful to leverage the new diffuse back illumination methodology which provides more flexibility in the optical setup and allows for increased spatial resolution to be achieved. It would be ideal for the light scattering measurements resolution to match the high spatial resolution of the radiography measurements. The spray structure looks different between the two measurements. This is evident by the shoulders seen in the radiography measurements, which are not seen in the diffuse back-illumination measurements (see Figure 46). This discrepancy in spray structure could be due to differing resolutions.

82

In the future, this SAMR technique should be applied to x-ray radiography and diffuse back illumination measurements conducted under other experimental conditions, including higher ambient densities and injection pressures. Additionally, steps should be taken so that this diagnostic can be applied under vaporizing and combusting sprays. Applying this diagnostic under a range of engine-relevant conditions is critical to assessing and formulating predictive spray breakup theories and computational models that can capture experimentally observed trends.

The SAMR technique currently provides time-averaged spatial droplet evolution maps, but in the future can provide time-resolved droplet information. This can be done by processing the Sauter Mean Diameter at the same instant in time for both x-ray radiography and diffuse back-illumination experiments. Thus, time resolved and spatially resolved droplet sizes can be quantified in diesel sprays and the spatiotemporal droplet evolution can and should be assessed.

One source of experimental uncertainty is the differing coordinate systems used at each facility. More of an effort can be made to replicate the measurement coordinate systems in the x-ray and extinction measurements to avoid uncertainty in co-alignment. Another way to reduce measurement uncertainties between the two facilities is by conducting the light scattering and the absorption measurement experiments at one facility. The light scattering experiments could remain the same, but another absorption method would have to be used, perhaps by utilizing an absorptive ultraviolet light source.

One source of uncertainty in the multiple scattering correction is that the transfer function for correcting the measured optical thickness was used from the literature for another facility and was modified for the Georgia Tech DBI setup. A calibration experiment like that of Berrocal should be setup to directly measure and quantify multiple scattering errors in the diffuse back-

illumination optical arrangement for several calibrated sphere diameters within the range of drop sizes expected in the experiment [28]. Also, a polydisperse mixtures of spheres could be measured which more accurately represents droplet sizes in diesel sprays. This calibration experiment would be used to construct an empirical transfer function for the DBI setup which can then be used to confidently correct the extinction measurements in the entire spray field, and therefore have a more accurate prediction of local SMD values.

APPENDIX A

SCATTERING ABSORPTION MEASUREMENT RATIO THEORY

The SAMR derivation is thoroughly presented in Magnotti's thesis [7]. A brief derivation will be presented here of the diagnostic. An expression will be derived which relates the optical thickness to the droplet size and liquid volume fraction when applying Mie's solution to Maxwell's equation [42]. Mie's solution to Maxwell's equations describe the scattering and absorption of light interacting with a homogeneous sphere, like a fuel droplet. Firstly, the optical thickness is related to the attenuation coefficient, α_{ext} and the illumination path-length, z.

$$\tau = \alpha_{ext}z \tag{17}$$

After some mathematical manipulation, the attenuation coefficient can be re-written in terms of the number weighted extinction cross section, $\overline{C_{ext}}$, where N is the number of droplets in a given volume V.

$$\alpha_{ext} = \frac{\overline{C_{ext}}N}{V} \tag{18}$$

For the DBI experiments, the light is scattered and therefore the extinction cross section is equivalent to the scattering cross section, $\overline{C_{ext}} = \overline{C_{scatt}}$. From equation 8, the term, N/V or the number of droplets in a given probe volume can be related to the liquid volume fraction. As the name suggests, the liquid volume fraction is the volume of liquid to the total volume. This equation can be further simplified by using the number weighted mean droplet volume.

$$LVF = \frac{V_{liq}}{V} = \frac{\sum_j N_j(\frac{\pi d_j{}^3}{6})}{V} \tag{19}$$

Equation 9 can be rearranged to solve for N/V. This expression can then be substituted into equation 8 for the attenuation coefficient.

$$\alpha_{ext} = \frac{\overline{C_{ext}} * LVF}{\frac{\pi d^3}{6}} \tag{20}$$

Finally, the optical thickness can be related to the spray parameters of extinction cross section, liquid volume fraction, and illumination path-length using equations 7 and 10.

$$\tau = \frac{\overline{C_{ext}}}{\frac{\pi d^3}{6}} * LVF * z \tag{21}$$

For Mie scattering (single and independent scattering), it is known that the extinction cross section is proportional to the cross-sectional area of the droplets [42].

$$C_{ext} \propto d^2 \tag{22}$$

The optical thickness from the DBI experiments (equation 3) can be related to this new expression for optical thickness (equation 12) in the single and independent scattering regime. In optically thin regions of the spray ($\tau < 2$), single scattering can be assumed. If a measurement of liquid volume fraction were present, the measured droplet size in a given probe volume could be calculated. The projected density, measured from the x-ray radiography measurement, can be recast as liquid volume fraction for non-vaporizing and constant liquid density conditions.

$$\overline{M} = \rho_f \frac{V_{liq}}{V} z \tag{23}$$

Rewriting projected density in terms of liquid volume fraction becomes,

$$\frac{\overline{M}}{\rho_f} = LVF * z \tag{24}$$

Because both quantities measured from the experiments are functions of liquid volume fraction, taking a ratio of these quantities will yield a relationship to the droplet size. One necessary assumption in this analysis is comparing equivalent measurement volumes. This assumption will be expanded in 3.4 Data Processing Steps.

$$\frac{\frac{\overline{M}}{\rho_f}}{\tau} = \frac{LVF * z}{\overline{C_{ext}} * \frac{LVF}{\frac{\pi d^3}{6}} * z} \tag{25}$$

Simplifying this expression yields a relationship between our measured quantities (τ and $\overline{M}$) and the mean droplet size within a probed volume or the SMD.

$$\frac{\frac{\overline{M}}{\rho_f}}{\tau} = \frac{\overline{\frac{\pi d^3}{6}}}{\overline{C_{ext}}} \alpha \frac{\overline{d^3}}{\overline{d^2}} = SMD \tag{26}$$

REFERENCES

[1] US Department of Energy, "Energy Consumption by Sector and Source," DOE Annual Energy Outlook, 2017.

[2] J. E. Dec, "Advanced compression-ignition engines- understanding the in-cylinder processes," *Proceedings of the Combustion Institute ,* vol. 32, no. 2, pp. 2727-2742, 2009.

[3] N. Peters and J. Weber, "The effects of spray formation and evaporation on mixing, auto-ignition, and combustion in Diesel engines," in *Conference on Thermo and Fluid Dynamic Processes in Direct Injection Engines*, Valencia, Spain, 2006.

[4] A. H. Lefebvre, Atomization and Sprays, New York: Taylor and Francis, 1989.

[5] J. Labs and T. Parker, "Diesel fuel spray droplet sizes and volume fractions from the region 25mm below the orifice," *Atomization and Sprays,* vol. 13, pp. 45-62, 2003.

[6] T. Parker, E. Jepsen and H. McCann, "Measurements and error analysis of droplet size in optically thick diesel sprays," *The Combustion Institute,* pp. 1881-1888, 1998.

[7] G. M. Magnotti, "Modeling the influence of nozzle-generated turbulence on diesel sprays," *PhD Dissertation Georgia Institute of Technology,* 2017.

[8] G. M. Magnotti and C. L. Genzale, "Detailed assessment of diesel spray atomization models using visible and X-ray extinction measurements," *International Journal of Multiphase Flow,* vol. 97, pp. 33-45, 2017.

[9] G. L. Martinez, G. M. Magnotti, B. W. Knox, K. E. Matusik, D. J. Daniel, C. L. Genzale, C. F. Powell and A. L. Kastengren, "Quantification of Sauter mean diameter in diesel sprays using scattering-absorption extinction measurements," in *Institute for Liquid Atomization and Spray Systems*, Atlanta, 2017.

[10] G. L. Martinez, F. Poursadegh, G. M. Magnotti, B. W. Knox, C. L. Genzale, K. E. Matusik, D. J. Duke, C. F. Powell and A. L. Kastengren, "Measurement of Sauter mean diameter (SMD) in Diesel sprays using a scattering-absorption measurement (SAMR) technique," in *Thermo and Fluid Dynamics Processes in Direct Injection Engines*, Valencia, 2018.

[11] T. C. Wang, J. S. Han and X. B. Xie, "Parametric characterization of high-pressure diesel fuel injection systems," *Journal of Engineering for Gas Turbines and Power,* vol. 125, pp. 412-426, 2003.

[12] S. Som and S. K. Aggarwal, "Effects of primary breakup modeling on spray and combustion characteristics of compression ignition engines.," *Combustion and Flame,* vol. 157, no. 6, pp. 1179-1193, 2010.

[13] R. Reitz, *Computer Modeling of Sprays,* Pittsburgh, 1996.

[14] R. D. Reitz and F. Bracco, "Mechanism of atomization of a liquid jet," *The Physics of Fluids,* vol. 25, no. 10, pp. 1730-1742, 1982.

[15] R. D. Rolf, "Atomization and other breakup regimes of a liquid jet," *PhD Dissertation Princeton University,* 1978.

[16] B. Munson, T. Okiishi, W. Huebsch and A. Rothmayer, *Fundamentals of Fluid Mechanics*, Hoboken: John Wiley and Sons, 2013.

[17] H. Zaheer, "Transient microscopy of primary atomization in gasoline direct injection sprays," *Georgia Institute of Technology,* 2015.

[18] J. B. Heywood, Internal Combustion Engine Fundamentals, New York City: McGraw-Hill, 1988.

[19] C. Crua, T. Shoba, M. Heikal, M. Gold and C. Higham, "High-speed microscopic imaging of the initial stage of diesel spray formation and primary breakup," in *SAE International*, Detroit, 2010.

[20] C. Crua, G. de Secrey, M. R. Heikal and M. Gold, "Dropsizing of Near-Nozzle Diesel and RME Sprays by Microscopic Imaging," in *Triennial International Conference on Liquid Atomization and Spray Systems*, Heidelberg, 2012.

[21] C. Crua, M. R. Heikal and M. R. Gold, "Microscopic imaging of the initial stage of diesel spray formation," *Fuel,* vol. 157, pp. 140-150, 2015.

[22] Y. Kim, "Development of Spectral Microscopy Imaging Technique for Time-Resolved Imaging of Primary Breakup in High-Pressure Fuel Sprays," *MS Thesis,* 2017.

[23] J. Labs and T. Parker, "Two-dimensional droplet size and volume fraction distributions from the near-injector region of high-pressure diesel sprays," *Atomization and Sprays,* vol. 16, pp. 843-855, 2006.

[24] T. D. Fansler and S. E. Parrish, "Spray measurement technology: a review," *Measurement Science and Technology,* 2015.

[25] W. D. Bachalo, "Spray Diagnostics for the Twenty-first Century," *Atomization and Sprays,* vol. 10, pp. 439-474, 2000.

[26] Dantec Measurement Technology, "Principles of Phase Doppler Anemometry," [Online]. Available: http://www.ara.bme.hu/neptun/BMEGEATMW03/2009-2010-2/FloMeas_pres_5.pdf. [Accessed 9 August 2018].

[27] R. Payri, L. Araneo, J. Shakal and V. Soare, "Phase doppler measurements: system set-up optimization for characterization of a diesel nozzle," *Journal of mechanical science and technology,* vol. 22, no. 8, pp. 1620-1632, 2008.

[28] E. Berrocal, "Multiple scattering of light in optical diagnostics of dense sprays and other complex turbid media," *Cranfield University,* 2006.

[29] L. Araneo and C. Tropea, "Improving Phase Doppler measurements in a diesel spray," in *International Spring Fuels & Lubricants*, Paris, 2000.

[30] M. C. Jermy and D. A. Greenhalgh, "Planar dropsizing by elastic and fluorescence scattering in sprays too dense for phase Doppler measurement," *Applied Physics B,* vol. 71, pp. 703-710, 2000.

[31] A. L. Kastengren, J. Ilavsky, J. P. Viera, R. Payri, D. J. Duke, A. Swantek, F. Z. Tilocco and C. F. Powell, "Measurements of droplet size in shear-driven atomization using ultra-small angle x-ray scattering," *International Journal of Multiphase Flow,* vol. 92, pp. 131-139, 2017.

[32] J. Ilavsky, P. R. Jemian, A. J. Allen, F. Zhang, L. E. Levine and G. G. Long, "Ultra-small-angle x-ray scattering at the Advanced Photon," *Journal of Applied Crystallography,* vol. 42, pp. 469-479, 2009.

[33] A. L. Kastengren, C. F. Powell, D. Arms, E. M. Dufresne, H. Gibson and J. Wang, "The 7BM beamline at the APS: a facility for time-resolved fluid dynamics measurements," *Journal of Synchrotron Radiation,* vol. 19, pp. 654-657, 2012.

[34] K. E. Matusik, B. A. Sforzo, H. J. Seong, D. J. Duke, A. L. Kastengren, J. Ilavsky and C. F. Powell, "X-Ray Measurements of Fuel Spray Specific Surface Area and Sauter Mean Diameter," in *International Conference on Liquid Atomization and Spray Systems*, Chicago, 2018.

[35] M. Meijer, B. Somers, J. Johnson, J. Naber, S.-Y. Lee, L. M. Malbec and G. Bruneaux, "Engine Combustion Network (ECN): Characterization and comparison of boundary conditions for different combustion vessels," *Atomization and Sprays,* vol. 22, no. 9, 2012.

[36] B. W. Knox, "End of Injection Effects on Diesel Spray Combustion," *PhD Dissertation Georgia Institute of Technology,* 2016.

[37] F. R. Westlye, K. Penney, A. Ivarsson, L. Pickett, J. Manin and S. Skeen, "Diffuse back-illumination setup for high temporally resolved extinction imaging," *Applied Optics,* 2017.

[38] Photron, "SA-X2 Technical Datasheet," 1 April 2015. [Online]. Available: file:///C:/Users/gmartinez36/Downloads/sa-x2_tech_datasheet_april_2015.pdf. [Accessed 1 November 2017].

[39] F. R. Westlye, " New standard for high temporal DBI," in *Engine Combustion Network*, Kyoto, 2015.

[40] Y. Yue, C. F. Powell, R. Poola, J. Wang and J. K. Schaller, "Quantitative measurements of diesel fuel spray characteristics in the near-nozzle region using x-ray absorption," *Atomization and Sprays,* vol. 11, pp. 471-490, 2001.

[41] J. Wang, "X-ray vision of fuel sprays," *Journal of Synchotron Radiation,* vol. 12, pp. 197-207, 2005.

[42] H. C. Van de Hulst, *Light scattering by small particles*, Dover Publications, 1981.

[43] P. Laven, "MiePlot," [Online]. Available: www.philiplaven.com/mieplot.htm. [Accessed 1 July 2017].

[44] E. Berrocal, D. L. Sedarsky, M. E. Paciaroni, I. V. Meglinski and M. A. Linne, "Laser light scattering in turbid media part 1: experimental and simulated results for the spatial intensity distribution," *Optics Express,* vol. 15, pp. 10649-10665, 2007.

[45] A. L. Kastengren, C. F. Wang, K. S. Im and J. Wang, "X-ray radiography measurements of diesel spray structure at engine-like ambient density," *Atomization and Sprays,* vol. 19, no. 11, 2009.

[46] G. M. Magnotti, K. E. Matusik, D. J. Duke, B. W. Knox, G. L. Martinez, C. F. Powell, A. L. Kastengren and C. L. Genzale, "Modeling the Influence of Nozzle-Generated Turbulence on Diesel Sprays," in *ILASS-Americas 29th Annual Conference on Liquid Atomization and Spray Systems*, Atlanta, 2017.

[47] G. J. Smallwood and O. L. Gulder, "Views on the structure of transient diesel sprays," *Atomization and Sprays,* vol. 10, pp. 355-386, 2000.

[48] K. J. Wu, R. D. Reitz and F. V. Bracco, "Measurements of drop size at the spray edge near the nozzle in atomizing liquid jets," *Physics of Fluids,* vol. 4, no. 29, pp. 941-951, 1986.

[49] H. Kosaka, T. Suzuki and T. Kamimoto, "Numerical simulation of turbulent dispersion of fuel droplets in an unsteady spray via discrete vortex method," *SAE Technical Paper,* 1995.

[50] W. W. Pulkrabek, Engineering Fundamentals of the Internal Combustion Engine, Upper Saddle River, N.J: Prentice Hall, 1997.

[51] B. Johnson and C. Edwards, "Exploring the Pathway to High Efficiency IC Engines through Exergy Analysis of Heat Transfer Reduction," *SAE Interntaional Journal of Engines,* vol. 6, no. 1, 2013.

[53] P.-K. Wu and G. M. Faeth, "Aerodynamic effects on primary breakup of turbulent liquids," *Atomization and Sprays,* vol. 3, pp. 265-289, 1993.